Reducing Added Noise in a Microwave-Mechanical-Optical Converter

by

Peter Schaunaman Burns

B.A., University of Montana, 2013

M.S., University of Colorado Boulder, 2016

A thesis submitted to the

Faculty of the Graduate School of the

University of Colorado in partial fulfillment

of the requirements for the degree of

Doctor of Philosophy

Department of Physics

2019

This thesis entitled:
Reducing Added Noise in a Microwave-Mechanical-Optical Converter
written by Peter Schaunaman Burns
has been approved for the Department of Physics

_____

Prof. Konrad Lehnert

_____

Prof. Cindy Regal

Date _____

The final copy of this thesis has been examined by the signatories, and we find that both the content and the form meet acceptable presentation standards of scholarly work in the above mentioned discipline.

Burns, Peter Schaunaman (Ph.D.,)

Reducing Added Noise in a Microwave-Mechanical-Optical Converter

Thesis directed by Prof. Konrad Lehnert

Viewed as resources for quantum information processing, microwave and optical fields offer complementary strengths. Quantum technologies operating at microwave frequencies have shown the ability to create and manipulate quantum information, making them leading candidates for building a quantum computer. Optical fields can transmit quantum information over long distances with low loss making them ideal for use as links between quantum nodes. Therefore the ability to transduce quantum information between microwave and optical frequencies is an essential technology in realizing an extended quantum network. To date there has been no demonstration of a microwave to optical link that is capable of quantum transduction.

This thesis describes the design and characterization of a device that couples one mode of a micromechanical oscillator to a resonant microwave circuit and a high-finesse optical cavity, thereby realizing a mechanically mediated electro-optic converter. We have operated this converter at $T < 100$ mK, and demonstrated unprecedented conversion efficiency of 47% and added noise of 38 photons. I discuss how noise correlations can be exploited to develop a feedforward protocol. I also discuss the limitations on the noise performance of the device used to achieve these results, and describe recent improvements in the fabrication process and optical and microwave resonator designs aimed at reducing added noise. These improvements should produce a device that is near the threshold for quantum conversion.

Acknowledgements

There is not enough space to thank the many people that contributed to the science and to my well being, up to and during my time on this project. Even if there was, I don't know if I have the words to truly express how lucky I have been to be surrounded and supported by such impressive individuals. My PhD would not have been possible without all of them, but here I make a meager attempt to thank the specific individuals who made this project possible. However, I must also express my gratitude to my parents and brother. Without their support and belief in me, none of this would have happened.

First, I would like to thank my committee members Graeme Smith, John Teufel, and Victor Bright for generously taking time out their busy schedules to provide feedback and guidance on this project and for the invaluable insights and discussions throughout my PhD. Cindy Regal's joint leadership of this project has been invaluable both to the productivity of the group, and to my growth as scientist.

Due to its fabrication-heavy nature, this project owes a debt of gratitude to all the staff at the NIST BMF cleanroom. Their patience and willingness to help allowed this project to succeed, and also made the cleanroom a welcoming place to work. A special thanks goes to Kat Cicak who I shadowed for my training and taught me nearly everything I know about fabrication.

I am grateful to all of the Lehnert and Regal lab members for their willingness to have open, engaging physics discussions at any moment's notice and for the sincere camaraderie that has been built both in the lab trenches and on the athletic pitch. In particular, I would like to thank the members of the microwave-to-optics team. Bob Peterson, Tim Menke, Oliver Wipfli, and Andrew

Higginbotham all made this project a joy to be a part of in the first half of my time here. I owe a special thanks to Andrew, not only for his direct efforts in lab, but more importantly for shaping me as a scientist and for the many wonderful conversations. To the newer members of the team, Max Urmey, Ben Brubaker, Sarang Mittal, and Jon Kindem, thanks for carrying me through to the finish line. Your creativity and energy made everyday exciting and thanks to you I have great confidence about the future of the project.

Finally, there is not a way to accurately recognize my advisor, Konrad Lehnert, for all he has done for me. Konrad's leadership as an advisor goes well beyond the level of scientific guidance. His excitement for all physics, both big and small, is contagious and meant there was rarely a dull discussion.

To all of you: thank you.

Contents

Chapter

Tables

Table

Figures

Figure

Chapter 1

Microwave-Optical Transducers as Tools for Quantum Networks

1.1 Quantum information networks

We are in the middle of the second quantum revolution [1]. The tools being developed in labs today are quickly finding their way into the growing field of commercially-available, quantum-assisted technologies. Rather than just describing and understanding the world using the framework of quantum mechanics, the second quantum revolution is based on harnessing quantum mechanics to build useful technologies. This change in our technical ability to control and manipulate systems at the quantum level has been advancing for nearly a century. The first quantum revolution was one of knowledge, as our views of the physical world were profoundly changed by the discovery of quantum theory at the turn of the 20th century. In its early stages, this theory was thought to describe very small, discrete systems, but the consequences of applying it to the macroscopic world were fiercely debated [2]. Schrödinger's famous cat is an example of the kind of paradox that seems to exist when the laws of quantum mechanics are used to describe macroscopic systems. Schrödinger himself even had this to say in 1952 about the idea of having experimental access to quantum degrees of freedom:

> We never experiment with just one electron or atom or (small) molecule. In thought-experiments we sometimes assume that we do; this invariably entails ridiculous consequences... We are not experimenting with single particles, any more than we can raise Ichthyosauria in the zoo [3].

Since that time, we have gained sufficient control over the quantum degrees of freedom of not just

microscopic atoms and molecules, but over semi-macroscopic objects. It has forced us to address the "ridiculous consequences," and more importantly it has allowed us to take advantage of them.

One of the areas that is benefiting from the consequences is the field of quantum information science. Because of the many superposed degrees of freedom, simulating a quantum system with a classical computer quickly becomes intractable. Simulating quantum systems on classical computing machines is inherently insufficient as the machinery is fundamentally different than what is being represented. This was realized in the 1980s as Feynman [4, 5] and Deutsch [6, 7] proposed using quantum systems themselves as a platform for simulation. Beyond just simulating quantum systems to learn more about the physics, the field gained considerable traction when an algorithm for efficiently factoring large numbers was developed [8]. The ability to efficiently factor large numbers sparked interest due to the fact that common encryption techniques such as RSA are based on factoring being a classically hard problem [9]. In parallel to the development of quantum computing theory, the field of cryptography also began realizing benefits from incorporating quantum information. The quantum key distribution protocol first proposed in 1984 [10], which takes advantage of the no-cloning theorem [11] to establish physically secure communication, is still the basis for multi-city [12, 13], and even satellite-based [14] quantum key distribution. While secure communication and encryption breaking are still driving forces in developing quantum technology, quantum science will also benefit other fields including quantum metrology [15] and force sensing [16], search algorithms [17], and chemical simulation [18, 19, 20].

A long standing goal for the field of quantum information is to realize an extended quantum network. A quantum network entangling spatially separated quantum nodes would permit secure communication and distributed quantum computing [21, 22, 23, 24]. The nodes create, store and manipulate quantum information, while links between them transmit information and allow for entanglement between nodes [25]. A quantum internet could follow the same road map as the modern internet, using local computers, operating on electronic signals, connected around the globe via fiber optic links. Just like classical information, quantum information has a physical platform. The information, however is independent of the physical implementation. We take this

fact for granted with classical information as signals in our computer are converted all the time from different physical states such as magnetic memory, electronic signals on chips, or fiber optic communication networks. Likewise, quantum information theory does not presuppose a physical system and as such there have been developments in quantum proving grounds across a variety of physical platforms. Propagating optical fields are the natural choice for quantum links in such a network, as they enable entanglement distribution at room temperature and over kilometer-scale distances. Promising qubits have been demonstrated across a variety of solid state implementations including superconducting qubits [26, 27, 28], spin qubits [29, 30], and charge qubits in various material systems [31, 32]. These solid state qubits typically have excitations energies corresponding to a range from a few GHz to a tens of GHz, suggesting that the most powerful nodes will use microwave-frequency excitations, and therefore will need to be operated in ultralow-temperature environments ($T < 100$ mK), so that thermal fluctuations don't obscure quantum signals. Making a large network all housed at these ultralow temperatures is fairly impractical, implying that a quantum state preserving electro-optic converter is a crucial element needed for a future quantum internet.

1.2 Microwave-Optical transducers

Given that classical networks already convert information between microwaves and optics, it is worth pointing out why the current commercially-available technology is not compatible with quantum signals. The technology used in modern communication networks works for classical transduction because efficiency and noise can be overcome by amplification. A quantum signals however, requires much more stringent conversion requirements as quantum states can not be amplified or cloned. Error correcting quantum algorithms exist [33], but still typically require an error rate less than 1% depending on the type of error [34]. If one is limited to Gaussian resources, a converter will only have quantum capacity if the efficiency is greater than 50% [35]. Furthermore, a quantum transducer needs to have a large enough bandwidth to convert a signal before it is lost. For a first-generation converter to be compatible with leading superconducting qubit lifetimes [36], a

conversion bandwidth of at least 10 kHz is required, however for long term applicability even larger bandwidths would be necessary. These stringent requirements for a quantum microwave-optical link make this a challenging task and has created an active and open field of research pursuing this effort.

Frequency conversion between the two domains is not possible without a significant nonlinearity, and the source of the nonlinearity is a useful way to categorize the different experimental approaches. The nonlinearity can come from a material susceptibility, or through an intermediary mode. The material susceptibility for microwave-optical conversion can either be a bulk effect that takes advantage of the electro-optic effect, or a resonant effect of a multi-level system. A parametric processes, such as coupling through an intermediary mechanical mode, can also give rise to a nonlinearity. In most schemes the single photon nonlinearity is very small, and therefore these schemes benefit from increasing the effect with the use of a resonant cavity, which enhances the photon interaction and increases the optical density of states.

Conversion based on materials with optical nonlinearities can further be divided into bulk solid state effects or resonant effects in atomic clouds or atom-like defects in solid-state hosts. For a solid state system, the susceptibility $\chi(\omega)$ of a crystal describes the polarization in response to an alternating electric field. The bonds in the crystal can respond in harmonic and anharmonic ways which leads to frequency mixing. The goal of electro-optic converters is to find materials with low loss and high $\chi^{(2)}$, where $\chi^{(2)}$ is the second order susceptibility that leads to the electro-optic effect, or Pockels effect. Experimental conversion efforts have shown success using whispering gallery mode optical resonators made out of $LiNbO_3$, which has a high $\chi^{(2)}$, placed inside a microwave cavity [37]. The challenge of such an approach comes from matching the resonance conditions between the microwave frequency and the spacing between optical modes, but an efficiency of $\eta = 1 \times 10^{-3}$ has still been achieved [38]. Another approach uses lithographically defined microwave resonators patterned on AlN which allows for higher mode overlap between the microwave and optical fields. This approach has lead to the highest efficiency in an electro-optic effect device of $\eta = 1 \times 10^{-2}$ [39]. Approaches in atomic like systems use a three level λ system where the spacing between the two

lowest levels is in the microwave range. Prospective conversion technologies using this technique are ultracold atoms [40, 41], or optically active spins in solids [42, 43, 44, 45, 46]. So far the strict resonant conditions of these systems have also limited there efficiency to $\eta = 5 \times 10^{-2}$, albeit with 15 MHz bandwidth [47].

Another approach (and the one pursued in this thesis) relies on coupling vibrational modes to microwaves and optical fields. The optomechanical interaction is appealing because it is mathematically symmetric between the microwaves and optical modes and the coupling is independent of intrinsic resonances and therefore can be tuned across a range of frequencies. The approach relies on mechanical motion parametrically coupling to one or both electromagnetic modes. For example, confining the mode to a nanomechanical element that uses piezoelectric coupling works well for mechanical modes in the GHz range. These converters benefit from the high mechanical frequencies that allow for less thermal occupation of the mode and for higher bandwidths, but are usually limited in efficiency and by heating of the mechanical mode from the optical field [48, 49].

In this thesis, our approach is to simultaneously couple a mechanical mode to both a microwave and optical cavity as shown in Figure 2.1. We use a doubly parametric approach that can reduce mode overlap between mechanics and optics and therefore shows less signs of heating. High quality mechanical modes combined with low-loss cavities have allowed for the highest efficiency and lowest added noise to date [50]. In a mechanical converter, low added noise requires high electromechanical and optomechanical cooperativities [51, 52], which have yet to be achieved together in a single device. In optomechanical systems, alternatives to high cooperativity have been explored to cool mechanical modes [53, 54, 55, 56, 57, 58, 59]. Our feedforward protocol makes use of the two ports of our device to present an alternative to the high cooperativity requirement for conversion.

1.3 Optomechanics for conversion

Our approach to use a mechanical element to couple between the optical and microwave domain is built on the field of optomechanics [60, 61, 62]. This field comes from two simple ideas:

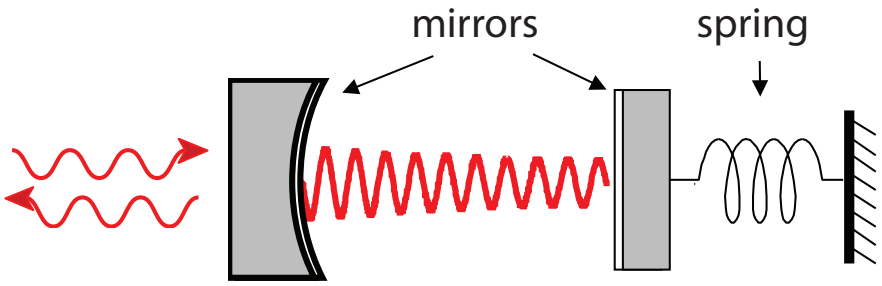

Figure 1.1: **Canonical optomechanics picture.** Two mirrors define a single mode optical cavity. The mirror on the left is partially transmissive and allows light to enter and exit. The mirror on the right behaves like a mass on a spring. Light in the cavity can push on the mirror through radiation pressure.

motion can influence light, and therefore electromagnetic signals, and light carries momentum. The first has been used to aid the technology revolution as mechanical elements are ubiquitous in modern devices from clocks, to sensors. The second was predicted by Maxwell's description of electromagnetism in 1873 [63], and was noticed by Johannes Kepler in the observation that comets' tails point away from the sun [64]. Experimental efforts to use light to affect motion and motion to affect light began being used to trap objects, starting with the microspheres [65] and developing into quantum control over single atoms [66, 67, 68, 69]. In parallel to using light to control objects, the quantum limits of continuous displacement detection were largely worked out in the context of interferometers used for gravitational wave detection. Developing theory and experimental platforms to study gravitational waves has led to much of the language used for studying optomechanics. For example, the standard quantum limit for measurement of the position of mechanical oscillator was developed in terms of the precision of an interferometer for searching for gravitational waves [70]. The advancement of the field fueled the search for gravitational waves [71, 72] and led to the experimental discovery and study of them [73]. Interferometers like LIGO are now so precise that quantum mechanical fluctuations of the light field are now the limiting factor in some parts of their sensitivity range [74, 75].

From the initial efforts to improve measurement sensitivity, emerged the broader fields of op-

tomechanics and electromechanics. Efforts to improve the sensitivity of optomechanical detectors is still a driving force, but has also led to other interesting uses for optomechanics–for example, putting mechanical objects into profoundly non-classical states [76, 77]. The canonical optomechanics experiment is an optical cavity in which one mirror is free to vibrate as shown in Figure 1.1. The motion of the mirror affects the light in the cavity, and therefore the light exiting the cavity holds information about the position of the mirror. The same interactions that were developed for cooling and trapping ions in harmonic potentials can be used to affect the motion of the mirror. In the microwave regime, the same picture applies, but with an LC circuit where one plate of the capacitor is free to vibrate. Experiments have developed to the level of control that the mechanical modes of these systems can be cooled to their quantum ground state [78, 79]. Mechanical resonators can also be used to entangle motion with microwave fields [80]. Preparing non-classical states of light has improved force sensitivity, but has also shown promise in quantum information fields as mechanical oscillators can be used for quantum memories [81] or dynamic signal processing including frequency conversion [82, 83, 84]. Quantum information can be transferred between microwaves and mechanical motion and between optical fields and mechanical motion, accomplishing both these quantum coherent couplings, simultaneously, to the same mechanical oscillator would achieve a quantum, electro-optic converter.

In this thesis, we explore electro-optic conversion in a mechanically mediated transducer. We operate a converter device at $T < 100$ mK, as required for compatibility with superconducting qubits. We demonstrate an unprecedented conversion efficiency of $47 \pm 1\%$, and implement a feedforward protocol that exploits noise correlations between the two converter output ports to reduce the noise added to a signal referred to the converter input to $N_{\mathrm{add}} = 38$ photons. These figures of merit represent significant technical progress relative to the 8% efficiency and 1500 photons of added noise achieved in a prototype system operated at 4 K [85]. Using the noise correlations, we explore an alternative feedforward framework where quantum tasks could be performed even if thermal-mechanical noise yields $N_{\mathrm{add}} > 1$, provided threshold efficiencies are reached. We characterize the limitations of this converter in terms of the sources of added noise and make technical

improvements to each part individually such that when put all together should be on the threshold of a quantum-enabled converter.

Chapter 2

Theory of Operation

This chapter lays out the theory needed to describe the operation of the converter. The converter is a system of three linearly coupled harmonic oscillators. In order to understand the physics of the full device, Section 2.1 starts by describing a single resonator coupled to internal and external ports. Section 2.2 introduces a mechanical oscillator and describes how it mediates the coupling between two electro-magnetic modes. The chapter finishes with a full description of the transducer as well as the mathematical machinery needed to describe correlations measured by exploring the system of three coupled oscillators in Section 2.3.

2.1 Electromagnetic resonators

The coupling between each component of the converter is shown in Figure 2.1. The resonators are shown as circles to highlight the fact that although physically quite different, mathematically they are equivalent. Each resonator couples to the environment at some internal loss rate κ_{int}. The mechanical resonator couples to each electromagnetic resonator at rate Γ, and the electromagnetic resonators couple to propagating fields at rate κ_{ext}.

Intrinsically, we care about the interaction between photons and motion. This effect is enhanced by confining the harmonic oscillator to high-Q, compact resonators. Although a single photon transfers a minuscule amount of momentum that would be obscured by the zero-point motion for all but the smallest mechanical oscillators, a cavity allows a photon to interact many times with the oscillator, transferring momentum with each pass. In the optical domain the resonator

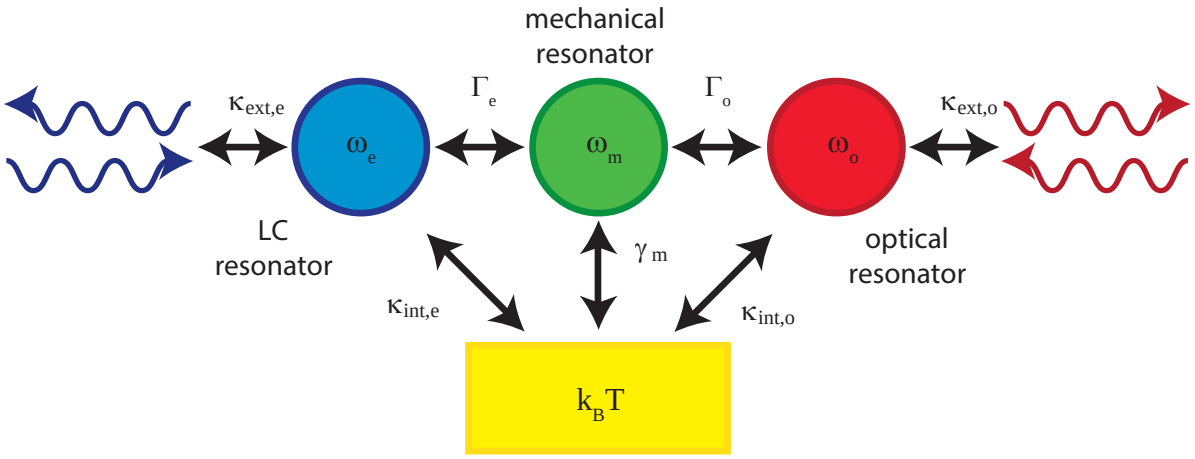

Figure 2.1: **Microwave optical transducer coupling diagram.** The two electromagnetic resonators (blue and red circles) are coupled to the mechanical resonator (green circle) at rates Γ. They each have there own loss rates coupled to the thermal environment. Propagating fields are coupled to the LC and optical cavity at rates κ.

can be formed by two mirrors, or in the microwave domain it can be a lumped element inductor capacitor circuit. Making the cavities more compact increases the sensitivity to displacement because a small change in position corresponds to a fractionally large change in a dimension that sets the resonant frequency. For an optical cavity this means making small spacings between the mirrors and for an LC circuit this means making a narrow gap capacitors.

An electromagnetic resonator and a mechanical oscillator both exhibit harmonic behaviour and therefore can be described by the same equations of motion. In a mechanical oscillator the oscillating quantities are position and momentum, while in an electrical oscillator they are the electric and magnetic fields. This can be described using input-output formalism and for the derivation of bare electromagnetic resonators and cavities interacting with mechanical motion we follow Ref. [62]. The mathematical notation describes equally well optical light confined between two mirrors in a cavity and electrical energy stored in inductor capacitor resonant circuits.

The state of the cavity, shown in Figure 2.2, can be described in a basis of coherent states $|\alpha\rangle$, which most closely approaches the classical notion of a cavity in a state of definite amplitude and phase, and described by a complex number α. In quantum optics it is more natural to work

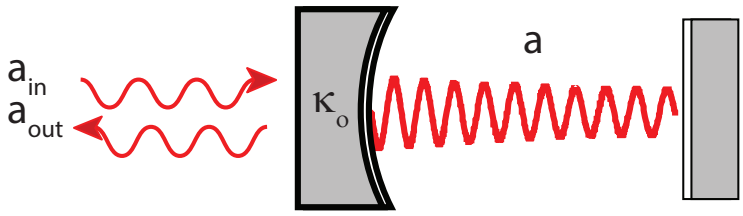

Figure 2.2: **Optical cavity coupling schematic.** A single electromagnetic mode in a Fabry-Perot cavity, characterized by the annihilation operator a which couples at rate κ_o to an incoming field a_{in} and an outgoing field a_{out}.

in the Heisenberg picture, where the equations of motion are written in terms of operators, in this case the annihilation operator $a(t)$, whose eigenstates are coherent states $a\,|\alpha\rangle = \alpha\,|\alpha\rangle$. The Heisenberg-Langevin equation of motion for a single cavity mode is:

$$\dot{a}(t) = \left(-i\omega_{\text{cav}} - \frac{\kappa}{2}\right) a(t) + \sqrt{\kappa_{\text{ext}}}\, a_{\text{in}}(t) + \sqrt{\kappa_{\text{int}}}\, f_{\text{in}}, \tag{2.1}$$

where w_{cav} is the resonant frequency, and $a^\dagger(t)a(t) = |a(t)|^2$ is number of photons in the cavity, and $a_{\text{in}}^\dagger(t)a_{\text{in}}(t) = |a_{\text{in}}(t)|^2$ is the incident power in units of photon number per second. Incident fields couple to the cavity at a rate κ_{ext} that we refer to as the external coupling rate. The external coupling rate is usually an engineered parameter and is determined by geometrical or material properties of the particular cavity. Fields inside the cavity are coupled to various loss mechanisms such as absorption or scattering to other modes. The loss rate κ_{int} can also be driven by bath modes f_{in}. The total cavity coupling rate is the sum of external couplings and internal coupling $\kappa = \kappa_{\text{int}} + \kappa_{\text{ext}}$. The dynamics of the cavity field are contained in the Heisenberg-Langevin equation along with the instantaneous relationship between the input fields, cavity fields, and output fields

$$a_{\text{out}}(t) = \sqrt{\kappa_{\text{ext}}}\, a(t) - a_{\text{in}}(t) \tag{2.2}$$

where a_{out} is the outgoing field and is normalized such that $|a_{\text{out}}|^2$ has units of photons/second.

We solve for the transfer function in the frequency domain (denoted by tilde symbols)

$$\Xi_{\text{1port}}(\omega) = \frac{\tilde{a}_{\text{out}}(\omega)}{\tilde{a}_{\text{in}}(\omega)} = -\frac{2i\Delta + \kappa_{\text{int}} - \kappa_{\text{ext}}}{2i\Delta + \kappa_{\text{int}} + \kappa_{\text{ext}}}. \tag{2.3}$$

Where ω is Fourier transform variable of t and it has been shifted from the cavity frequency ω_{cav} by Δ by working the rotating frame. By measuring the amplitude and phase response of a cavity, we characterize the external and internal coupling rates. There are three regimes of coupling that are commonly referred to, overcoupled, critically coupled, and undercoupled. Overcoupled is when the external coupling rate is the dominant loss rate for photons in the cavity and is usually desired as it means most the information leaves the cavity into a mode that can be measured. Critically coupled means the two loss rates are equal, and undercoupled means that the internal loss rate of the cavity dominates.

2.2 Cavities coupled to mechanical oscillators

The coupling of a cavity to a mechanical oscillator is examined here. An uncoupled mechanical oscillator is describable with the same equations of motion as the cavities. Here we use the Hamiltonian formalism to calculate the coupling between a harmonic oscillator and a cavity. This can be used to describe the dynamics of optomechanical systems in both classical and quantum regimes. The optical and mechanical modes used in this derivation are completely generic. The Hamiltonian for an uncoupled system is just the sum of the two harmonic oscillators, and without constant terms is written as

$$H = \hbar\omega_{\mathrm{cav}} a^\dagger a + \hbar\omega_{\mathrm{m}} c^\dagger c. \tag{2.4}$$

Where c is the mechanical oscillator's annihilation operator, and ω_{m} is the mechanical oscillator's resonance frequency.

We now introduce the coupling of the cavity's resonance frequency to the position of the mechanical element. We find an interacting term linear in x by Taylor expanding the x dependent cavity resonance frequency to first order in x. The cavity resonance frequency as a function of the position is written as

$$\omega_{\mathrm{cav}}(x) = \omega_0 + x\frac{\partial\omega_{\mathrm{cav}}(0)}{\partial x} + \mathcal{O}\big(x^2\big). \tag{2.5}$$

Substituting this in and only keeping terms to first order gives an interaction Hamiltonian as

$$H_{\rm int} = -\hbar G x a^\dagger a, \tag{2.6}$$

where $G = -\frac{\partial \omega_{\rm cav}}{\partial x}$ is the frequency shift per unit displacement. The coupling term can also be understood because the radiation pressure of light is proportional to the intensity, thus the interaction Hamiltonian is the number operator $a^\dagger a$ multiplied by the position operator. The position x is written in terms of creation and annihilation operators as $x = x_{\rm ZPF}(c+c^\dagger)$, where $x_{\rm ZPF}$ is the mechanical oscillators zero-point fluctuation amplitude. It has the form $x_{\rm ZPF} = \sqrt{\hbar/2M_{\rm eff}\omega_{\rm m}}$ where $M_{\rm eff}$ is the effective mass of the oscillator. We also define a single photon phonon coupling rate $g_0 = G x_{\rm ZPF}$ which is a useful parameter to characterize the strength of the optomechanical interaction. We change the description of the optical mode by switching to a frame rotating at the pump or laser frequency ω_L. Now the interaction Hamiltonian takes the following form

$$H_{\rm int} = -\hbar g_0 a^\dagger a (c + c^\dagger). \tag{2.7}$$

The interaction is simplified by linearizing the optical field by splitting it into a classical amplitude and a remaining fluctuating term, $a = \alpha + \delta a$. The classical component sets the scale of the interaction. Terms proportional to $|\alpha|^2$ represent static shifts that we will absorb into a new cavity resonance frequency and equilibrium oscillator displacement. Terms proportional to δa^2 are dropped. The terms of the form $\delta a \alpha^\dagger$ and c.c. contain the interesting dynamics. In the rotating frame around the laser frequency we introduce detuning $\Delta = \omega_{\rm L} - \omega_{\rm cav}$. With these changes, we write the Hamiltonian

$$H^{\rm lin} = -\hbar\Delta\delta a^\dagger \delta a + \hbar\omega_{\rm m} c^\dagger c - \hbar g_0 \sqrt{n_{\rm cav}}(\delta a^\dagger + \delta a)(c^\dagger + c). \tag{2.8}$$

Where $n_{\rm cav} = |\alpha|^2$ is the intracavity photon number. Here one could return to using input-output formalism to write down the full Heisengberg-Langevin equations of motion. Instead we look at the interaction for different detunings to elucidate the effects of laser detuning.

The detuning of the pump tone leads to different forms of the Hamiltonian which have different physical effects. First, if the pump is detuned below the cavity by the mechanical resonator

frequency $\Delta = -\omega_m$, and the rotating wave approximation is used, the dominant term is the Hamiltonian of two oscillators at the same frequency that can exchange energy with the interaction

$$H_{\text{int}}^{\text{red}} = -\hbar g(\delta a^\dagger c + \delta a c^\dagger) \tag{2.9}$$

at rate $g = g_0\sqrt{n_{\text{cav}}}$. From the language of quantum optics this is the beamsplitter Hamiltonian. It swaps a mechanical excitation with an electromagnetic excitation. If the fluctuating piece δa is in its vacuum state, then this cools the mechanical oscillator as it swaps thermal phonons for optical vacuum states. This is also the interaction used to transduce electromagnetic excitations into mechanical oscillations that we take advantage of in our converter operation. This cooling process can be understood from a conservation of energy argument. Photons from the pump are converted to photons at the pump frequency plus mechanical frequency. This difference in energy is provided by one mechanical phonon..

The interaction takes a different form if the pump is detuned above the cavity by the frequency of the mechanical oscillator $\Delta = \omega_m$. This is referred to as blue detuned and the interaction has the form

$$H_{\text{int}}^{\text{blue}} = -\hbar g(\delta a^\dagger c^\dagger + \delta a c). \tag{2.10}$$

This interaction creates pairs of entangled excitations. It represents two mode squeezing and parametric amplification [86]. Again, this can be understood from energy conservation. The energy is scattered into a lower frequency sideband and therefore gives up energy to create a mechanical excitation, entangling mechanical motion with light. In the language of atomic physics, the two interactions are the stokes and anti-stokes sidebands and in the same way are used to cool or excite mechanical motion of trapped atomic systems.

2.3 Bidirectional microwave optical conversion

For understanding the behavior of the converter we derive condensed equations of motion. We start with Hamiltonian again and then move to a state-space model, from which the full dynamics

can be implemented with computation software and are used to check our results of operating a converter.

The Hamiltonian with an additional electromagnetic resonator coupled to the same mechanical mode is written as

$$H = \hbar\omega_{\mathrm{o}}\hat{a}^{\dagger}\hat{a} + \hbar\omega_{\mathrm{e}}\hat{b}^{\dagger}\hat{b} + \hbar\omega_{\mathrm{m}}\hat{c}^{\dagger}\hat{c} + \hbar G_{\mathrm{o}}(\hat{a}^{\dagger}\hat{a})\hat{x} + \hbar G_{\mathrm{e}}(\hat{b}^{\dagger}\hat{b})\hat{x} \tag{2.11}$$

where, $\hat{a}$, $\hat{b}$, and $\hat{c}$ denote annihilation operators for the optical, electrical and mechanical modes, respectively. Frequencies ω_i describe the mode resonant frequencies, with subscripts $i = \{\mathrm{o}, \mathrm{e}, \mathrm{m}\}$ denoting optical, electrical, and mechanical. The couplings from the optical and microwave resonators to the mechanical mode are denoted G_{o} and G_{e}.

The Hamiltonian used to calculate the Heisenberg-Langevin equations of motion [87] can then be linearized about a strong, coherent pump field as in Section 2.2. The resulting system of first-order, linear differential equations are concisely described as a state space model [88].

$$\dot{\mathbf{a}}(t) = A\mathbf{a}(t) + B\mathbf{a}_{\mathrm{in}}(t) \tag{2.12}$$

$$\mathbf{a}_{\mathrm{out}}(t) = C\mathbf{a}(t) + D\mathbf{a}_{\mathrm{in}}(t) \tag{2.13}$$

where $\mathbf{a} = (\hat{a}, \hat{b}, \hat{c}, \hat{a}^{\dagger}, \hat{b}^{\dagger}, \hat{c}^{\dagger})$ is a vector of the resonator modes that represents the internal state of the converter, and $\mathbf{a}_{\mathrm{in}}$ ($\mathbf{a}_{\mathrm{out}}$) is a vector of input (output) fields. See Ref. [85] for full matrix forms. The state-space model reduces to a transfer function

$$\mathbf{a}_{\mathrm{out}}(\omega) = \Xi(\omega)\mathbf{a}_{\mathrm{in}}(\omega) \tag{2.14}$$

$$\Xi(\omega) = C(-i\omega I - A)^{-1}B + D \tag{2.15}$$

Where we use $f(\omega) = \int_{-\infty}^{\infty} f(t)e^{-i\omega t}\mathrm{d}t$. This formalism reflects our measurement, where we apply fields (i.e. modify $\mathbf{a}_{\mathrm{in}}$) and measure fields (i.e. measure components of $\mathbf{a}_{\mathrm{out}}$). It provides us with a framework to understand the performance of our converter device. For example, the efficiency, characterized by the transmission coefficient corresponds to the transfer function element $\Xi_{a_{\mathrm{out,L}},b_{\mathrm{in,R}}}(\omega) = a_{\mathrm{out,L}}(\omega)/b_{\mathrm{in,R}}(\omega)$.

Frequency-dependent fluctuations leaving each port are useful for describing added noise, two mode squeezing and mechanical temperature. The spectra of the output fields are expressed in terms of a matrix $\mathbf{S}(\omega)$, whose elements are given by

$$S_{ij}(\omega)\delta(\omega-\omega') = \frac{1}{2}\langle\{[\mathbf{a}_{\mathrm{out},i}(\omega')]^{\dagger}, \mathbf{a}_{\mathrm{out},j}(\omega)\}\rangle. \tag{2.16}$$

Chapter 3

Converter Device Used for Highest Efficiency, Lowest Added Noise, and Feedforward

This chapter describes the apparatus used to couple a harmonic oscillator to both microwaves and light. Section 3.1 explains the transducer chip geometry that forms the LC circuit and mechanical membrane. The wireless coupling method is outlined in Section 3.2, which allowed us to reach the highest efficiency converter. Next, is a discussion of the optical cavity geometry in Section 3.3, and how the integration with the 3D microwave cavity allowed for higher optomechanical coupling and greater optical stability. The chapter finishes by laying out the data acquisition setup in our measurement network in Section 3.4. Iterations and improvements made to the device will be discussed later in Chapters 6 and 7

3.1 Electromechanical transducer chip

The basic concept and layout of the transducer chip is described in detail by Andrews [89]. Therefore we will summarize the device and highlight salient features and changes that made the results of this thesis possible. One challenge of a mechanical microwave optical transducer is working with mechanical modes that couple to both microwave and optical photons. Silicon nitride (SiN) membranes have performed well in pure optomechanical applications.. They have low loss at optical wavelengths and can be made with high stress to increase their quality factors. Although ground state cooling has been achieved for SiN membranes with optics [90], and for aluminum drum heads with microwaves [78], a mechanical oscillator that couples to both microwaves and

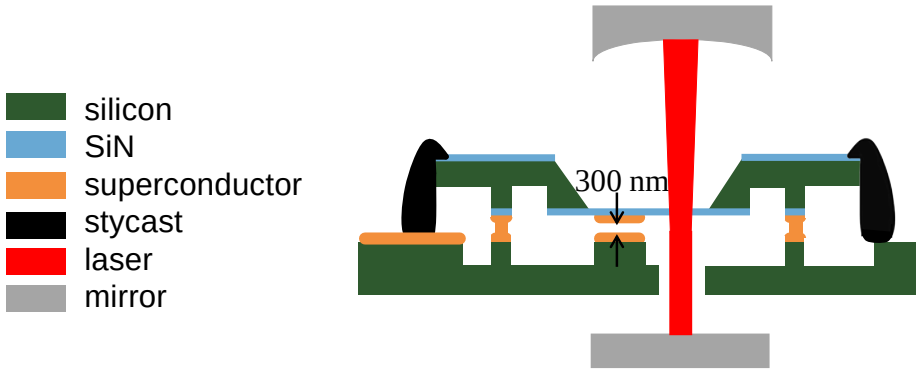

Figure 3.1: **Profile view of flip-chip device.** The transducer flip-chip is formed by two pieces of silicon. The bottom has an inductor loop and one part of a capacitor. The top chip consists of a high stress membrane stretched across a silicon frame with one portion covered by a patch of superconductor. When the top chip is brought very close, it forms a LC circuit whose resonance is modified by the motion of the membrane. It is aligned to the mode of an optical cavity so that the optical resonance is modulated by the motion of the membrane. The areas of silicon that are not critical for the posts or circuit are recessed away to reduce the chance of dust dictating the separation.

optics has yet to be ground state cooled. Our approach is to couple a SiN membrane to a high finesse optical cavity, with one corner coated in a superconducting thin film to form one plate of a parallel plate capacitor. In this way when the membrane moves from regions of high intensity to low in the standing wave of the optical cavity, it changes the optical length of the cavity and therefore modulates the resonant frequency. Likewise when the metal plate moves, it changes the capacitance of the microwave circuit and modulates its resonance frequency. This realizes the physics described in Section 2.2 where in both cases deflection causes a linear change in cavity resonance frequency.

We realize the electromechanical converter hardware by microfabricating a transducer chip. The transducer chip consists of two silicon chips: one with an inductive wire loop and the bottom plates of the capacitor, the other with a suspended slab of dielectric with a patch of metal for the top capacitor plate. The mechanical oscillator is a 100 nm thick, 500 μm wide silicon nitride membrane suspended from a silicon chip. A 25 nm thick, niobium film which serves as one capacitor pad is fabricated on one quadrant of the membrane before it is released. The membrane chip is flipped

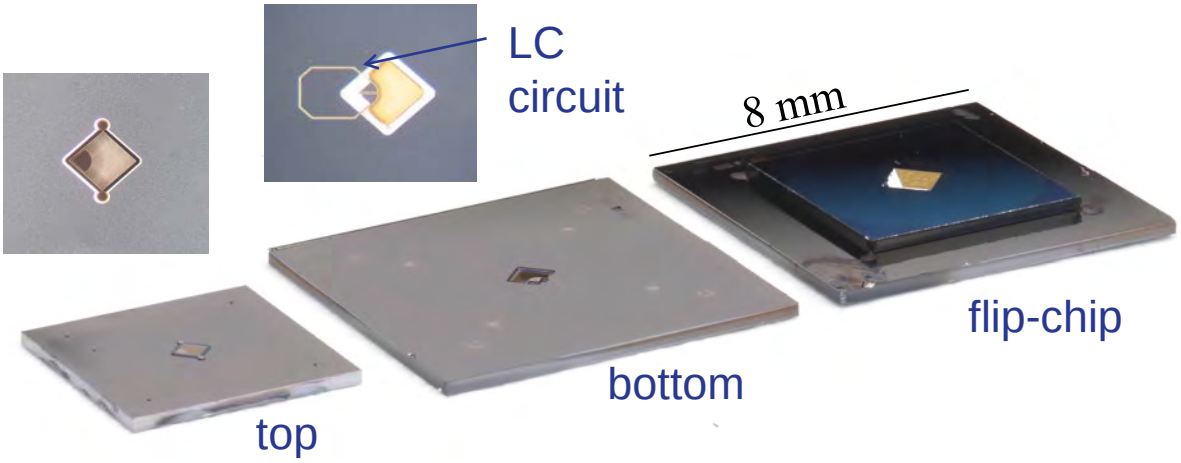

Figure 3.2: **Photo of fabricated top and bottom chip and flip-chip.** The top and bottom chips are shown with zoomed in regions of the centers. The flip-chip is formed by epoxying the top chip to the bottom chip.

over and affixed to a second silicon chip, on which a microfabricated niobium circuit comprising an inductor and a second capacitor pad was previously patterned using standard lithographic techniques. Figure 3.1 shows a profile schematic view of the assembled flip-chip device in an optical cavity, while Figure 3.2 shows the top and bottom chips and assembled flip-chip. The areas of the top and bottom chip that do not have the capacitor plate or posts are recessed away to reduce the chance of dust limiting the chip separation.

The flip-chip assembly is constructed with a West Bond manual die bonder, and the chips are affixed using Stycast 2850. In the fully assembled flip-chip device, the two niobium pads form a parallel-plate capacitor with a plate spacing of 300 nm, and the resonant frequency of the resulting LC circuit is modulated by vibrations of the mode of interest.

3.2 Wireless microwave coupling to the circuit

By using a 3D cavity to couple to the LC circuit on the transducer chip [91], we were able to reduce the optical cavity length, which improved the optomechanical coupling but more importantly reduced the optical cavity loss. Because the cavity removes the need for a galvanic connection to

the chip, we refer to it as wireless coupling. Here we motivate the need for wireless coupling and describe the coupling method.

The total converter efficiency is limited by our ability to make strongly overcoupled microwave and optical cavities. The external coupling rate is set by design, but the internal loss rate is dependent on the optical cavity stability to misalignment. In the first iteration of the converter the efficiency was limited to 8.5% [85] mainly due to loss in the optical cavity. In that experiment, the optical cavity had a length that was limited to greater than 4 mm to accommodate the components needed for the microwave chip and the transmission lines. This relatively long cavity length and numerous components made the cavity more sensitive to geometric misalignment. The chip was connected to microwave transmission lines by flexible circuit boards of gold coated copper printed on polyimide film. This cavity design became more misaligned upon cooling down than other pure optomechanics experiments by our group. This could have been because the flexible circuit boards stressed the chip holder, or could just be from the long cavity having so many components, each with its own epoxy joint with the potential to misalign as the epoxy and components shrank when cooled down. Moving to a smaller cavity geometry improves the cavity coupling efficiency by making it less sensitive misalignment. However, even moving to 2 mm in the old geometry, a reduction by a factor of two, would not have been possible as the chip holder and components between the mirrors were too thick. In order to reduce the optical cavity length the microwave coupling scheme was changed to remove components needed for the wired connection.

Previously, the coupling from the LC circuit to the transmission line was via an on-chip coplanar waveguide that was terminated with the center conductor forming a loop to ground (Figure 3.3). Mutual inductance between the loop and the inductor of the circuit sets the external coupling rate of the circuit. The chip was then wire-bonded to a flexible circuit board. Our strategy to remove bulky components and reduce connections to the chip was to use a 3D cavity with a circulating magnetic field to inductively couple to the chip. The cavity mode and coupling can be understood by considering the cavity as a distributed LC circuit, where the inductive current path is through the cavity and the capacitance is set by the area and separation of the central post. This produces

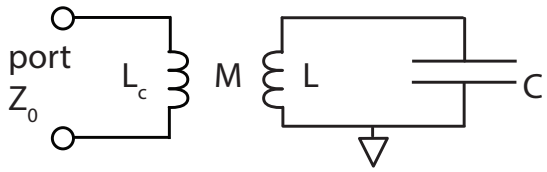

Figure 3.3: **Circuit coupling diagram.** Port with impedance Z_0 is terminated in inductor L_C with mutual inductance M to circuit formed by inductor L and mechanically compliant capacitor C

cavity modes with well separated electric and magnetic fields. The circulating magnetic field couples effectively to the magnetic antennae formed by the wired loop inductor on chip. A schematic of the coupling cavity and the chip are shown in Figure 3.4. The resonance of the cavity is set by the path length inductance the capacitance of the center posts. Being able to make changes to the resonance frequency by only adjusting either the capacitance or inductance makes this cavity geometry easy to work with as these can be adjusted in machining or by making modular pieces. The cavity also couples to external microwave ports via loop antennas. The cavity is made of gold and copper-coated invar. The invar was used to reduce misalignment of the optical cavity from thermal contraction, while the coatings were used for their low loss microwave properties.

Figure 3.5a presents the integration of the microwave cavity with an optical Fabry-Pérot cavity. The exploded view in Figure 3.5b shows how the microwave and optical parts of the device have been physically decoupled. This greatly reduces the complexity of the setup. The optical cavity and membrane on the chip can now be aligned and assembled in the same way as a pure optomechanics system [92]. The small number of interfaces and symmetric design of the mount are expected to minimize misalignment that arises from thermal contraction. Parts E-F, dubbed the "hat" of the microwave cavity, contain the center posts and connect the device to the microwave circuitry via coaxial loop couplers. We can readily change to a hat with different center post separation without interfering with any other part of the device. The external coupling can also be adjusted by changing the size of the loop couplers. In this way, we have precise control over the

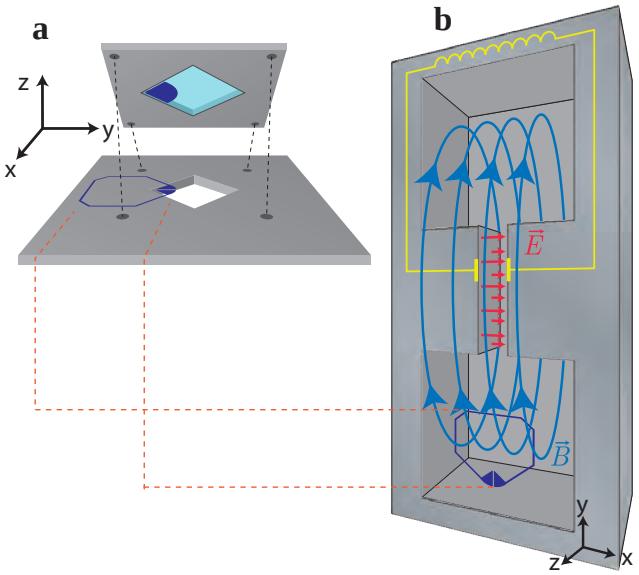

Figure 3.4: **3D cavity coupling. a,** The microwave-to-optics transducer is assembled from two silicon chips (gray). A silicon nitride membrane (light blue) is suspended on the top chip and a niobium circuit (dark blue) is patterned on the chips. **b,** Cutaway drawing of the re-entrant microwave cavity. The cavity (gray) can be modeled as an effective LC circuit (yellow line), spatially separating electric field (red) and magnetic field (blue arrows).

microwave cavity's resonant frequency and coupling to the external ports.

Figure 3.6a outlines the relevant coupling rates of the 3D microwave cavity and electromechanical chip. The cavity has two ports and couples to them with external coupling rates $\kappa_{\mathrm{cav},1}$ and $\kappa_{\mathrm{cav},2}$, respectively. The coupling rates are chosen such that $\kappa_{\mathrm{cav},1} \gg \kappa_{\mathrm{cav},2}$. In this way, transmission and reflection measurements can be performed while minimizing the signal that is lost in reflection. In addition, there is an internal cavity loss rate $\kappa_{\mathrm{cav,loss}}$ due to absorption and radiation through seams. In total, energy stored in the cavity decays at the rate $\kappa_{\mathrm{cav,tot}} = \kappa_{\mathrm{cav},1} + \kappa_{\mathrm{cav},2} + \kappa_{\mathrm{cav,loss}}$. The inductive coupling rate between the cavity and LC is quantified by the frequency g. It depends on the size and position of the LC circuit's loop inside the re-entrant cavity. The external and inductive coupling rates can be estimated by finite element simulations to guide the design process

The coupling of the re-entrant microwave cavity mode to both the transmission line and the LC circuit gives rise to an effective, wireless coupling of the external microwave ports to the LC

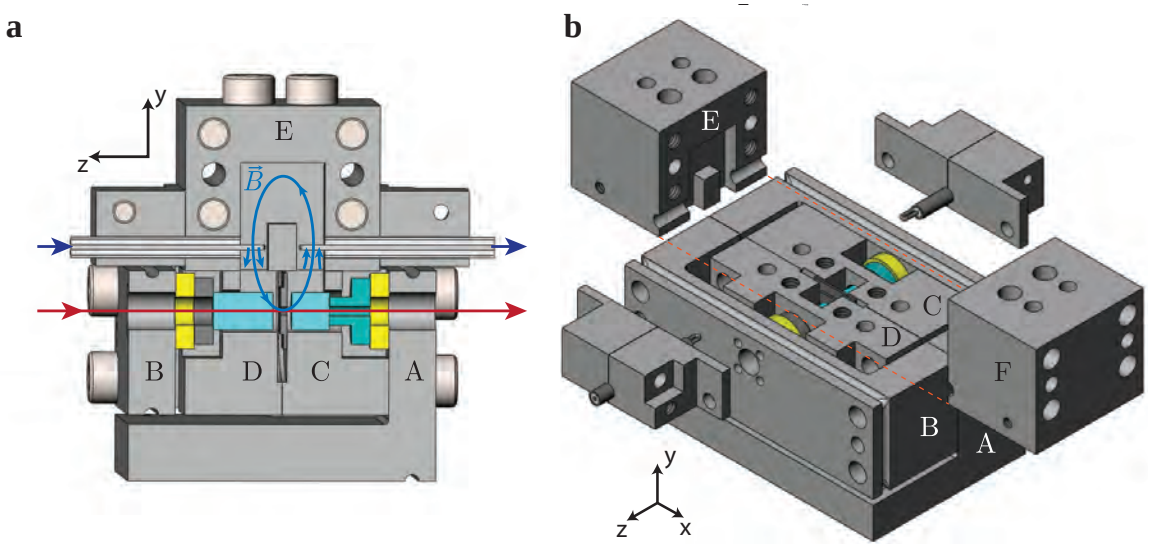

Figure 3.5: **Converter microwave and optical cavity designs. a,** Cutaway drawing of the complete assembly. The device mount consists of pieces labeled A-E. The re-entrant cavity volume is formed in the middle with magnetic field (blue arrows). The cavity couples to microwave input and output (dark blue arrows) via loop antennas made from coaxial cables. The transducer chip (dark gray) is located inside an optical Fabry-Pérot cavity. The mirrors (light blue) are brought in through holes in the microwave cavity walls. They are connected to piezoelectric crystals (yellow) via aluminum and fused-silica spacers (dark gray and turquoise, respectively). The optical path is shown as a red arrow. **b,** Partially exploded view of the device, showing how the microwave and optical parts separate. The optical cavity is mounted on parts A-B. Excess piezo wiring (not shown) can be wrapped around the grooves on the sides of parts A-B, relieving stress from the connection between piezo and wire. Part C serves as the sample holder for the transducer chip. At the same time, parts C-F form the microwave cavity volume. The "hat" consisting of parts E-F contains the re-entrant cavity's center posts and has holders for the loop antennas attached. The microwave and optical parts are in contact only via part C.

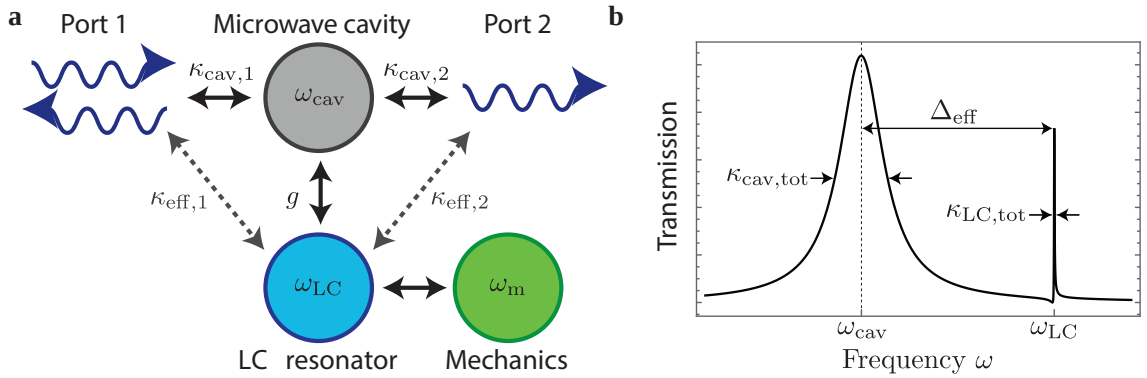

Figure 3.6: **3D cavity theoretical coupling description.** **a,** Schematic overview of the components and coupling rates involved in the setup. The microwave cavity (gray) couples to the transmission line (dark blue) via two ports, with external coupling rates $\kappa_{\mathrm{cav},1}$ and $\kappa_{\mathrm{cav},2}$, respectively. It also couples to the LC resonator (light blue) with rate g. This results in effective coupling rates $\kappa_{\mathrm{eff},1}$ and $\kappa_{\mathrm{eff},2}$ of the two ports to the LC resonator, given by Eq. (3.1). Additionally, the microwave cavity and LC resonator have internal decay rates $\kappa_{\mathrm{cav,loss}}$ and $\kappa_{\mathrm{LC,bare}}$, respectively (not shown). In electromechanical measurements, the LC resonator also couples to the mechanical mode of the membrane. **b,** Magnitude squared of the theoretical transfer function in absence of mechanical coupling. Cavity linewidth $\kappa_{\mathrm{cav,tot}}$, effective detuning Δ_{eff}, LC linewidth $\kappa_{\mathrm{LC,tot}}$ labeled.

circuit. The cavity resonant frequency ω_{cav} and the LC resonator frequency ω_{LC} have been shifted from their bare values by the coupling, and their effective detuning is $\Delta_{\mathrm{eff}} = \omega_{\mathrm{cav}} - \omega_{\mathrm{LC}}$. For sufficient detuning $\Delta_{\mathrm{eff}} \gtrsim \kappa_{\mathrm{cav,tot}}$, g, the effective coupling of the LC circuit to the cavity ports is given by

$$\kappa_{\mathrm{eff,i}} = \kappa_{\mathrm{cav,i}} \frac{g^2}{\Delta_{\mathrm{eff}}^2 + (\kappa_{\mathrm{cav,tot}}/2)^2}, \tag{3.1}$$

where $\mathrm{i} \in \{1, 2, \mathrm{loss}\}$. We call the couplings $\kappa_{\mathrm{eff},1}$, $\kappa_{\mathrm{eff},2}$ to the transmission line "wireless" because there is no direct connection of the LC circuit to a waveguide or coaxial cable. Note that the effective coupling leads to an LC dissipation rate $\kappa_{\mathrm{LC,loss}} = \kappa_{\mathrm{LC,bare}} + \kappa_{\mathrm{eff,loss}}$ that is higher than the bare loss rate $\kappa_{\mathrm{LC,bare}}$ of the circuit.

The design targets an effective coupling $\kappa_{\mathrm{eff},1}/2\pi$ in the 1.5-2.0 MHz range. In this way, the LC circuit is well over-coupled with respect to its expected internal loss rate, which is typically 0.4 MHz for our niobium circuits. The total LC decay rate $\kappa_{\mathrm{LC,tot}} = \kappa_{\mathrm{eff},1} + \kappa_{\mathrm{eff},2} + \kappa_{\mathrm{LC,loss}}$ then also fulfills the resolved sideband criterion: $\kappa_{\mathrm{LC,tot}} \ll 4\omega_{\mathrm{m}}$, where the chip is designed to have a mechanical

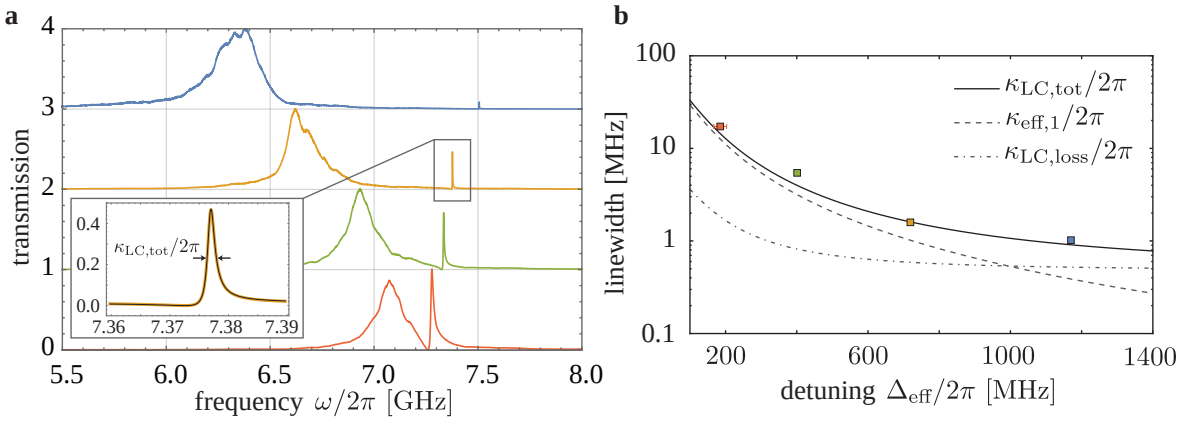

Figure 3.7: **Varied LC couplings a,** Normalized transmitted power versus frequency for four different center post separations: 238 μm (blue), 270 μm (orange), 300 μm (green), 316 μm (red). The broad peak corresponds to the cavity resonance, and the narrow peak corresponds to the LC resonance. Offsets added to curves for clarity. Inset: Zoom of LC line shape for 270 μm post separation, with FWHM, $\kappa_{\mathrm{LC,tot}}$, labeled. Fit of the theoretical transfer function shown in black. Averaging over fits to all four curves gives the cavity-LC coupling $g/2\pi = 57(2)$ MHz, and the bare LC loss rate $\kappa_{\mathrm{LC,bare}}/2\pi = 0.48(3)$ MHz. **b,** LC linewidth versus effective detuning. Colored squares indicate the $\kappa_{\mathrm{LC,tot}}$ obtained for the different post separations. Lines show theoretical predictions for the total LC linewidth ($\kappa_{\mathrm{LC,tot}}$, solid), effective coupling ($\kappa_{\mathrm{eff,1}}$, dashed) and loss rate ($\kappa_{\mathrm{LC,loss}}$, dot-dashed) with g and $\kappa_{\mathrm{LC,bare}}$ fixed from (a). The measured range of effective couplings contains the target regime 1.5-2.0 MHz.

resonance frequency $\omega_{\mathrm{m}}/2\pi \sim 1.5$ MHz. The last inequality ensures that electro-optic conversion occurs without photon number gain, as required for quantum state preservation. From Eq. (3.1) we understand that we need to couple the re-entrant cavity strongly to both the LC circuit and the transmission line. In particular, the re-entrant cavity should couple to port 1 much more strongly than it couples to its internal loss such that most of the LC decay is due to its coupling to the transmission line: $\kappa_{\mathrm{cav,1}} \gg \kappa_{\mathrm{cav,loss}}$. In order to limit the dissipation added to the LC resonator, an internal Q-factor of about 500 for the re-entrant cavity is targeted. Finite element simulations show that an inductive coupling $g^{\mathrm{theo}}/2\pi = 60$ MHz and external coupling $\kappa_{\mathrm{cav,1}}^{\mathrm{theo}}/2\pi = 150$ MHz to port 1 can be achieved. A desired effective coupling then requires a detuning $\Delta_{\mathrm{eff}}^{\mathrm{theo}}/2\pi \sim 600$ MHz.

The device behaviour is accurately modeled by Eq. (3.1). Figure 3.7b shows the LC linewidths $\kappa_{\mathrm{LC,tot}}$ that are extracted directly from the measured transmission spectra. These are compared to

a plot of the theoretical total loss rate $\kappa_{\mathrm{LC,tot}}$ that is obtained from Eq. (3.1) using the fitted model parameters. Both agree well for large detuning. The desirable and undesirable LC loss are plotted as $\kappa_{\mathrm{eff},1}$ and $\kappa_{\mathrm{LC,loss}}$ in the figure. Note that the wireless coupling has been varied by over an order of magnitude by using the different hats. In the target regime of 1.5-2.0 MHz for the effective coupling, the unwanted dissipation rate $\kappa_{\mathrm{LC,loss}}$ constitutes at most 30 % of the total LC loss rate. The dissipation contribution is reduced to 17 % when operating the device in the millikelvin regime.

3.3 Optical cavity

The optical cavity design and assembly is described in Ref. [93]. Here we discuss it in enough detail to motivate its limitations and improvements. Using a 3D cavity to mediate coupling between the chip and a transmission line allowed for the removal of all other components between the mirrors except the chip itself. The chip is 0.7 mm thick which allowed for a reduced the cavity length by a half to 2 mm, any smaller and the cavity assembly becomes unwieldy. Figure 3.5a shows a side view of the optical Fabry-Pérot cavity. The cavity consists of two stacks of components ending in highly reflective surfaces. The stacks have piezoelectric elements for adjustments of the optical cavity length and membrane position, as well as invar and fused silica spacers to shorten the cavity. The cavity components are all referenced to parts A and B. Piezoelectric elements are mounted outside of the microwave cavity volume.

The optical cavity is comprised of two mirrors, with 29 ppm and 98 ppm power transmission respectively, which can give a range of external couplings $\kappa_{\mathrm{ext}}/2\pi = 1.0 - 2.0$ MHz depending on membrane position (Figure 6.8). The chip assembly is placed in the standing wave of the optical cavity with the membrane 750 μm from the high-transmission mirror, such that the membrane's vibrations modulate the cavity's resonant frequency [94]. The optical mode intersects the membrane in the quadrant opposite the capacitor, and these two regions of the membrane move in phase for the mechanical mode of interest. We refer to this as a three-element cavity because the mirrors and membranes are all fixed relatively separate to each other. The main challenge here is to control the alignment of the three surfaces while they are referenced to larger invar pieces that are 3 cm

further away. Each joint of the stack of components is held together with stycast and represents a possible source of misalignment upon cooling down.

Unlike the microwave cavity which needs to be tuned to the right frequency at room temperature and then is inaccessible cold, the optical cavity parameters are partially adjustable. By applying voltage to the piezoelectric actuators, the mirrors can be moved. Common-mode motion moves where the membrane is in the standing wave and differential motion changes the resonant frequency. During operations, one of these actuators is used in a Pound-Drever-Hall cavity locking scheme to keep the optical pump at a fixed detuning from the cavity resonance [95]; the other may be used to change the membrane position within the optical standing wave of the cavity. The locking scheme uses an optical beam to monitor the cavity and slow drifts are fed back to the piezo, while fast changes are fed directly to the laser. The locking beam is injected on resonance with the cavity and is always present during converter operation. This is important to highlight because it means that even with no conversion beam, there is a fixed level of optical power in the cavity from the lock beam that affects the LC circuit in the form of added noise that depends on the amount of locking power.

3.4 Data acquisition

The device is characterized by making scattering parameter measurements and by collecting spectral data. Measurements are made by sweeping the frequency of a tone incident on a network component. The phase and amplitude of the reflected or transmitted signal are measured and used to extract scattering parameters. For example, the converter box is characterized by a series of probe-tone scattering parameter measurements $S_{ij}(\delta)$, where $i = \mathrm{e}, \mathrm{o}$ is the measured port, $j = \mathrm{e}, \mathrm{o}$ is the excited port, and δ is the frequency of the probe relative to the pump [85]. Spectral information is acquired by acquiring a signal at the output of a network port for some amount of time and then taking the Fourier transform to acquire power spectral density information.

The full experimental setup is detailed in Figure 3.8. Data acquisition is performed with a Zurich Instruments HF2LI lock-in amplifier. Scattering parameters are measured by sweeping

an output tone and demodulator frequency, and spectra can be measured by taking a time trace and computing the Fourier transform. The converter is operated at the base temperature of a dilution refrigerator with optical access, and a cryogenic HEMT amplifier is used for microwave measurements. Microwave signals are measured by demodulating with an I/Q mixer, remodulating at a frequency of 10 MHz, then feeding into the HF2LI. The demodulate-remodulate procedure allows both microwave quadratures to be measured by a single physical channel, and makes the signal processing functions performed by the HF2LI symmetric between the microwave and optical domains. Optical signals are measured by combining the beam exiting the cavity with an LO on a beamsplitter and reading out the difference port of a balanced heterodyne detector.

When computing device output spectra, a signal to be measured $s(t)$ is demodulated at a frequency $f_\mathrm{d} = f_\mathrm{c} + f_\mathrm{m}$, where f_c is the carrier frequency: $f_\mathrm{c} = 10$ MHz for microwave measurements and $f_\mathrm{c} = 12$ MHz for optical measurements. The resulting quadratures, $q(t)$ and $p(t)$, are used to compute,

$$a(t) = (q(t) + ip(t))e^{i2\pi f_\mathrm{d} t}, \tag{3.2}$$

which is the complex-equivalent signal of $s(t)$,

$$a(t) = s(t) + iH[s(t)], \tag{3.3}$$

where H denotes the Hilbert transform. The Fourier transform of $a(t)$, $a(\omega) = \int_{-\infty}^{+\infty} a(t)e^{-i\omega t}\,\mathrm{d}t$ is then computed approximately using DFT. $a(\omega)$ is a complex-valued function,

$$a(\omega) = X(\omega) + iY(\omega), \tag{3.4}$$

with real component $X(\omega)$ and imaginary component $Y(\omega)$, and is zero when $\omega < 0$. In the limit of narrow-band demodulation the quadrature variances satisfy e.g., $\mathrm{Var}(q_\mathrm{o}) = \langle X_\mathrm{o}(\omega_\mathrm{m}) X_\mathrm{o}(\omega_\mathrm{m})\rangle$. A demodulation bandwidth of $2\pi \times 50$ Hz is used for all quadrature data. Note that away from mechanical resonance, $X(\omega)$ is not just the Fourier transform of $q(t)$, but rather contains contributions from both $q(t)$ and $p(t)$. Spectra are displayed shifted so that f_c appears at zero frequency.

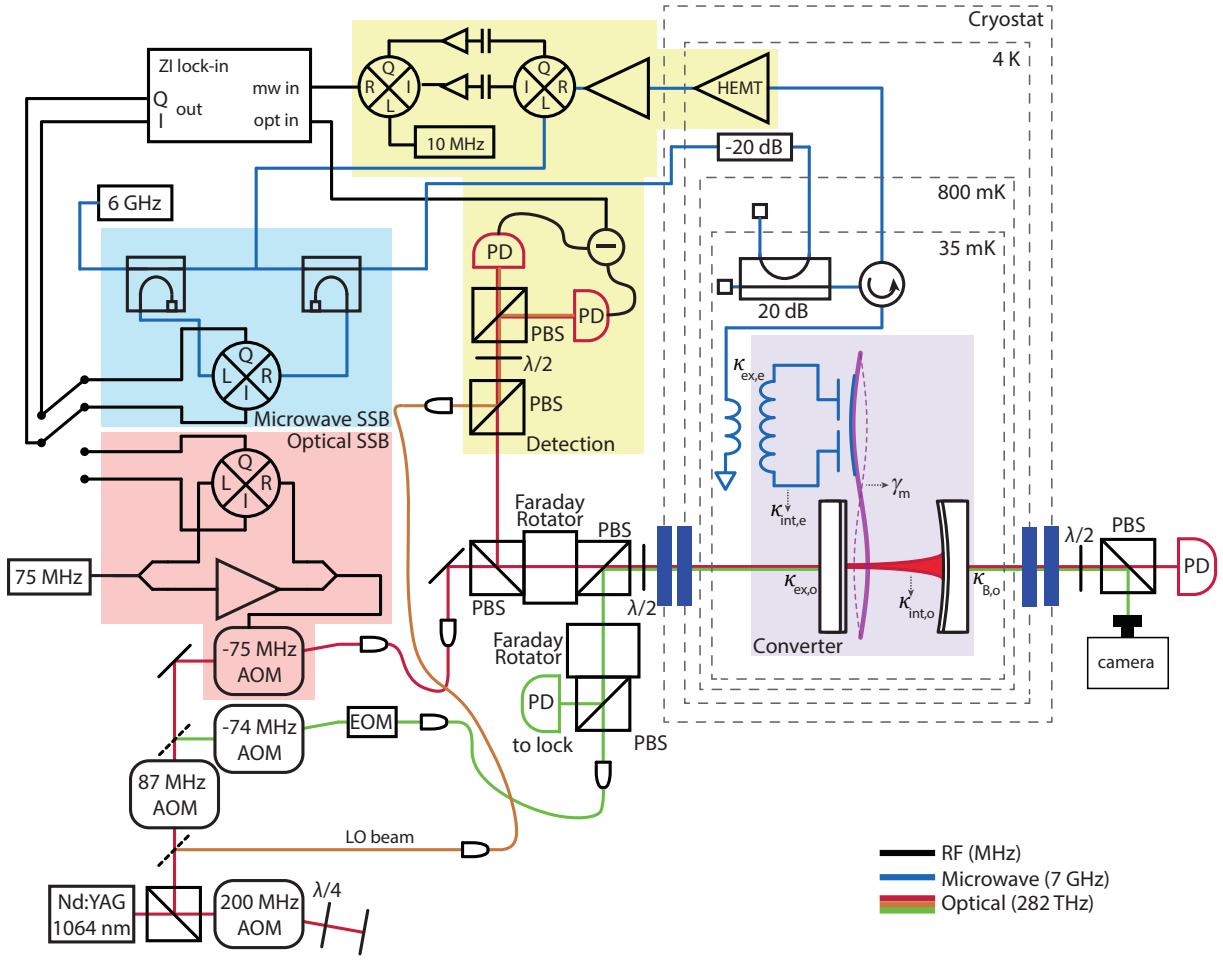

Figure 3.8: **Measurement Network**. A Zurich Instruments Lock-in Amplifier (ZI) is used as a spectrum and network analyzer. Outputs are driven 90° out of phase to produce a single sideband probe tone. In the microwave single sideband generator (blue box), a mixer is used to produce a single upper sideband directly on the microwave pump. The optical single sideband modulation (red box) is first mixed with an intermediate 75 MHz tone to drive an AOM. A lock beam (green) is used to reference and lock the optical cavity. The converter (purple box) is thermalized to the base plate of an optical access dilution refrigerator (grey dashed box), and microwave and optical tones are routed in with appropriate filtering. A directional coupler is used at base to provide filtering and an effective cold load. Transmission through the optical cavity can be used for characterization. Reflected and converted signals are routed by circulators to detection (yellow). A cryogenic HEMT amplifier is used for microwave amplification. The microwave output signal is demodulated with an I/Q mixer, remodulated at a frequency of 10 MHz, and then routed to the ZI. The optical beam is mixed with a local oscillator beam (orange) and measured in heterodyne. Spectrum analyzer measurements can be made by turning the ZI outputs off and fixing the demodulation frequency.

Chapter 4

State-of-the-Art Conversion

This chapter characterizes the conversion performance of the device described in Chapter 3. The metrics described are converter bandwidth, efficiency, and added noise. The device parameters and coupling terms are laid out in Section 4.1. Next the measurement network and procedure is discussed in Section 4.2. Experimental results follow, highlighting our highest efficiency device (4.3) as well as added noise performance (4.4). Section 4.5 concludes with a summary of the calibrations used to determine the added noise.

4.1 Converter parameters

The device described in Chapter 3 is housed in a cryostat with base temperature $T = 35$ mK. This realizes microwave and optical cavities simultaneously coupled to a single vibrational mode of a suspended dielectric membrane. Each cooldown represents a separate realization of the converter device as the device parameters change from cooldown to cooldown both due to our design choices and uncontrolled changes to physical geometries upon thermal cycling. Therefore, the table 4.1 lists the parameters from one device, in this case our highest efficiency device. The microwave and optical cavities are characterized first in the absence of the optomechanical interaction.

4.1.1 Microwave cavity parameters

The microwave network is characterized by reflection, and scattering measurements. Off-resonance of the LC circuit, all the power is reflected, allowing us to use this value to calibrate the net

Table 4.1: Converter parameters for high efficiency $\eta_{\mathrm{M}} = 0.43$ device configuration.

$\kappa_{\mathrm{e}}/2\pi$	2.5	MHz
$\kappa_{\mathrm{ext,e}}/2\pi$	2.3	MHz
$\kappa_{\mathrm{int,e}}/2\pi$	0.2	MHz
$\Delta_{\mathrm{e}}/2\pi$	-1.47	MHz
$G_{\mathrm{e}}x_{\mathrm{zp}}/2\pi$	3.8	Hz
$\kappa_{\mathrm{o}}/2\pi$	2.1	MHz
$\kappa_{\mathrm{ext,o}}/2\pi$	1.1	MHz
ϵ	0.87	
$\kappa_{\mathrm{B,o}}/2\pi + \kappa_{\mathrm{int,o}}/2\pi$	1.0	MHz
$\Delta_{\mathrm{o}}/2\pi$	-1.11	MHz
$G_{\mathrm{o}}x_{\mathrm{ZPF}}/2\pi$	6.6	Hz
$\omega_{\mathrm{m}}/2\pi = f_{\mathrm{m}}$	1.4732	MHz
$\gamma_{\mathrm{m}}/2\pi$	11	Hz

loss and gain of the microwave chain. By normalizing to the off-resonance value the response of the LC cavity can be isolated and is described by the transfer function of a one-port cavity as in Eq. 2.3. Measuring the amplitude and phase response and fitting to the transfer function (see Figure 4.1), extracts internal and external coupling rates, $\kappa_{\mathrm{ext,e}}/2\pi = 2.3$ MHz and $\kappa_{\mathrm{int,e}}/2\pi = 0.2$ MHz. Narrow band measurements around the LC resonance frequency have background levels that match the resonant dip value, $|S_{\mathrm{ee}}(0)|^2 = 0.69$.

4.1.2 Optical cavity parameters

Unlike in the microwave domain, the optical measurement does not have a well calibrated frequency knob. Because our experiment does not have some fixed transition like an atomic energy level, the laser and cavity are allowed to drift slightly as long as they track together. This makes wide band scattering parameter style measurements of the optical cavity difficult. Instead the optical cavity is characterized by sweeping a beam with sidebands of a known frequency across resonance as in Figure 4.2. The optical beam is modulated with an EO so that sidebands show up at a known frequency spacing. As the frequency of the carrier is swept across resonance the reflected voltage is measured as a function of time. Three dips appear corresponding to the main

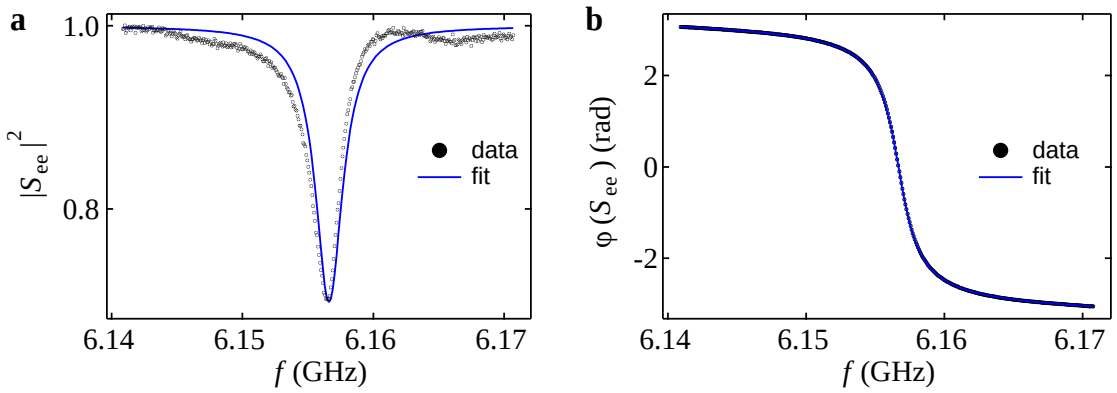

Figure 4.1: **Microwave scattering parameters.** Measured scattering parameter of microwave circuit (black), with fit (blue) to extract cavity coupling rates. (a) Power response shows Lorentzian dip with some background ripple characteristic of wide band measurement. (b) Phase response.

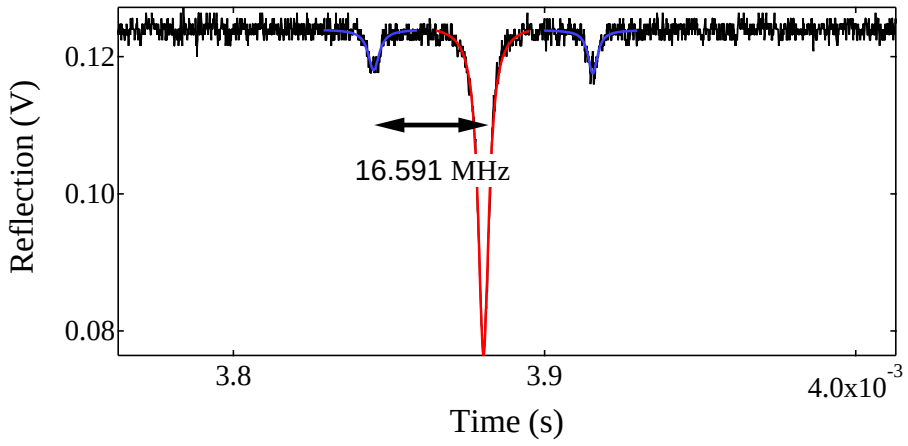

Figure 4.2: **Optical cavity linewidth characterization.** Reflection of the optical cavity is measured on a photodetector. Carrier beam is modulated using EO to produce sidebands of known frequency. Carrier beam frequency is swept through cavity resonance. The x-axis is the real measured time. Fitting to the three peaks allows for calibration for the x-axis into frequency units as the peak spacing is well known. A fit to the center peak extracts optical cavity linewidth.

beam and the two sidebands sweeping across the cavity. The two sidebands are used to calibrate the x-axis from time to frequency units. Then, a fit to the Lorentzian dip extracts the optical cavity coupling rates. The optical response is further complicated compared to the microwave cavity by the mode matching between the incident beam and cavity mode. This is discussed in more detail in Section 4.3.2.

4.2 Measurement procedure and converter operation

The device is characterized by making scattering parameter measurements or by looking at the output spectrum from either port. In scattering parameter measurements we measure the fraction of power transmitted or reflected by the converter. Noise characteristics can be made by looking at the output spectrum of the device. A simplified measurement setup showing signal routing to and from the device is shown in Figure 4.3. The mechanical oscillator is shown coupled to both the LC circuit and optical cavity. Strong pump tones are single-sideband modulated to produce a probe tone whose frequency can be tuned. Signals are directionally routed to heterodyne measurement chains discussed in more detail in Section 3.4. The device is studied by making reflection or transmission measurements or by measuring the power spectra at either port.

The converter is turned on by using two strong pump tones, one optical and one microwave. These pump tones are detuned from there respective cavities by roughly the mechanical resonator frequency. Along with the two pump tones, a weak probe tone, incident on either the microwave or optical cavity, is measured in heterodyne detection, and used for characterization. The probe frequency is swept relative to the pump tone to measure response as a function of frequency. Signals from the device are routed to measurement chains that measure scattering parameters or spectra.

With a strong red-detuned pump beam incident on the optical cavity, the optomechanical interaction couples the mechanical oscillator to propagating optical fields at a rate Γ_o that exceeds the intrinsic mechanical damping rate $\gamma_m = 2\pi \times 11$ Hz. At pump detuning $\Delta_o = -\omega_m$ and in the

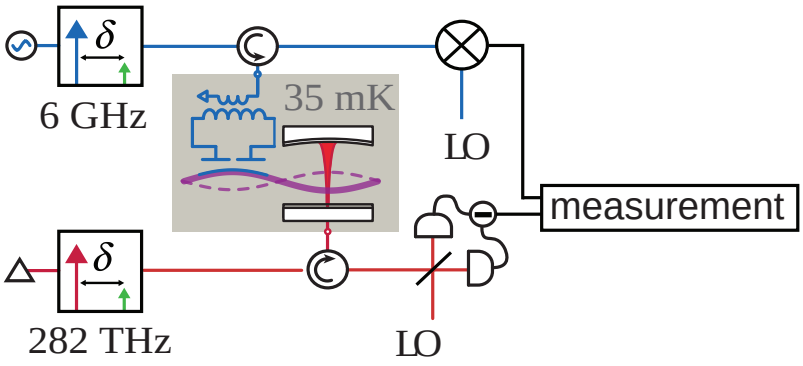

Figure 4.3: **Simplified measurement network.** Microwave (optical) signal routing chain in blue (red). Grey box represents base of dilution refrigerator. Carrier tones are single sideband modulated to produce probe tone at frequency δ. Measurements are made in heterodyne. Reflection and transmission measurements can be made of converter device.

resolved sideband limit ($4\omega_{\mathrm{m}}/\kappa_{\mathrm{o}} \gg 1$), the optomechanical damping rate has the simple form[85]

$$\Gamma_{\mathrm{o}} = \frac{4G_{\mathrm{o}}^2 x_{\mathrm{zp}}^2 \alpha_{\mathrm{o}}^2}{\kappa_{\mathrm{o}}}, \tag{4.1}$$

where α_{o} is the intracavity pump amplitude and x_{zp} is the zero-point amplitude of the membrane mode. The electromechanical damping in the presence of a strong red-detuned microwave pump tone has the same form:

$$\Gamma_{\mathrm{e}} = \frac{4G_{\mathrm{e}}^2 x_{\mathrm{zp}}^2 \alpha_{\mathrm{e}}^2}{\kappa_{\mathrm{e}}}. \tag{4.2}$$

In practice, our converter is moderately sideband-resolved ($4\omega_{\mathrm{m}}/\kappa_{\mathrm{o}} \approx 4\omega_{\mathrm{m}}/\kappa_{\mathrm{e}} \approx 2.5$), with pump detunings $\Delta_{\mathrm{e}}/2\pi = -1.47$ MHz and $\Delta_{\mathrm{o}}/2\pi = -1.11$ MHz. These details change the precise form of the expressions for Γ_{o} and Γ_{e} but not the essential physics. The full details are derived from equations in Chapter 2. Imperfect sideband resolution leads to some power gain in the converter which in the resolved sideband regime and $\Delta = -\omega_{\mathrm{m}}$ simplifies to $\mathcal{A} = \left[1 + (\frac{\kappa_{\mathrm{e}}}{4\omega_{\mathrm{m}}})^2\right]\left[1 + (\frac{\kappa_{\mathrm{o}}}{4\omega_{\mathrm{m}}})^2\right]$. We set the optical pump detuning Δ_{o} to maximize the optomechanical damping rate per incident photon. In the resolved sideband limit, this maximum damping occurs at $\Delta_{\mathrm{o}} = -\omega_{\mathrm{m}}$, but this is not generally the case with imperfect sideband resolution.

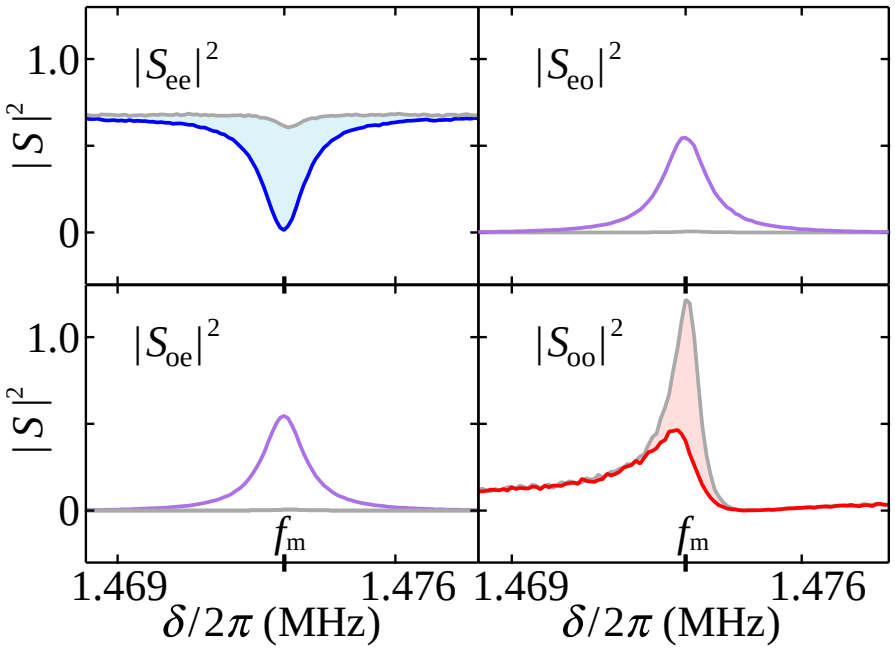

Figure 4.4: **Converter scattering parameters.** Measured converter scattering parameters versus probe frequency δ: microwave reflection (S_{ee}), optical reflection (S_{oo}), microwave-to-optical transmission (S_{oe}), and optical-to-microwave transmission (S_{eo}). Colored trace is $\Gamma_e \approx \Gamma_o$. Gray trace is $\Gamma_e \ll \Gamma_o$, with same Γ_o. Shaded region highlights induced absorption of incident power when conversion rates are matched.

4.3 Extracting bandwidth and efficiency from scattering parameters

A series of probe-tone scattering parameter measurements $S_{ij}(\delta)$ characterize the converter box as described in Section 3.4. The device performance is explored for a range of pump powers, and therefore conversion rates, in order to extract bandwidths and efficiencies. As shown in Figure 4.4, when $\Gamma_e \approx \Gamma_o$, a dip in microwave reflection occurs near $\delta/2\pi = f_m$, with a corresponding peak in microwave-to-optical transmission, indicating the absorption of signals in the microwave port and their emission at the optical port. A nearly identical optical-to-microwave transmission signal is also observed. The peak transmission $|t|^2 = 0.55$ corresponds to a conversion efficiency of $\eta = |t|^2/\mathcal{A} = 0.41$, where $\mathcal{A}$ is the independently measured converter gain due to imperfect sideband resolution. The converter bandwidth (measured as the full width at half maximum of the transmission peak) is given by the total linewidth of the optomechanically and electromechanically damped membrane

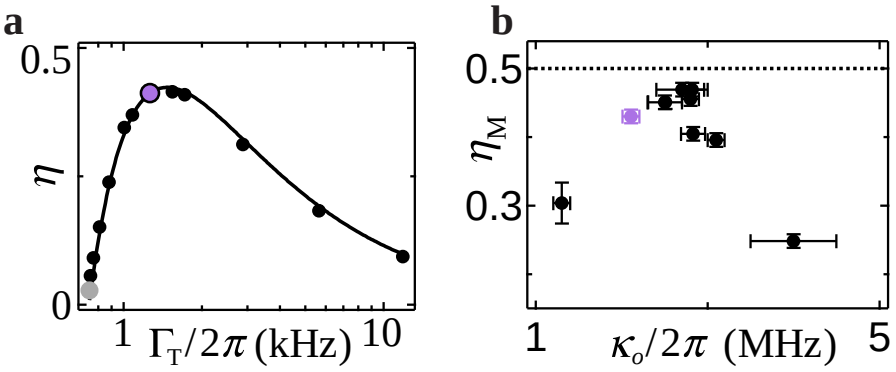

Figure 4.5: **Converter efficiency. a,** Converter efficiency η versus total damping Γ_T. Γ_T is swept by tuning Γ_e with Γ_o fixed. Black line is a fit to Eq. 4.3. Purple and gray points correspond to data in Figure 4.4. **b,** Matched efficiency η_M versus optical cavity linewidth κ_o. The ratio of external optical cavity coupling to internal loss varies with κ_o. Black dotted line indicates quantum feedforward threshold at $\eta_\mathrm{M} = 0.5$, discussed in Chapter 5. Horizontal error bars represent the standard deviation of several repeated linewidth measurements. Vertical error bars are obtained by propagating standard error in individual scattering parameter measurements.

mode, $\Gamma_\mathrm{T} = \Gamma_\mathrm{e} + \Gamma_\mathrm{o} + \gamma_\mathrm{m}$.

For comparison, if Γ_e is decreased such that $\Gamma_\mathrm{e} \ll \Gamma_\mathrm{o}$, microwave reflection becomes almost flat, with a value determined by the microwave cavity coupling, and nearly zero power is transmitted. At the same time, a peak is observed in optical reflection resulting from optomechanically induced transparency effects. The peak height exceeds one due to converter gain from not being sideband resolved (see Section 4.3.1). The optical reflection peak is suppressed when $\Gamma_\mathrm{e} \approx \Gamma_\mathrm{o}$, constituting electromechanically induced optical absorption.

The efficiency of the device is characterized by the total efficiency from the microwave port to the optical port. Inefficiencies in the measurement chain are not counted against the efficiency of the device. However, we do consider external coupling efficiency from both the microwave and optical cavities rather than just the internal efficiency of resonant microwave fields converted to resonant optical field. There are several compromises that are made in building a full converter in comparison to pure optical or microwave experiments and only looking at the internal efficiency would not accurately represent the potential use of this device.

The efficiency is extracted from peak transmission for a range of Γ_e with $\Gamma_\mathrm{o} = 2\pi \times 725$ Hz

fixed (figure 4.5a). For fixed optical cavity parameters, efficiency is maximized when damping rates are matched ($\Gamma_e = \Gamma_o$, $\Gamma_T = 2\pi \times 1.45$ kHz). The conversion efficiency is fit to [85]

$$\eta = \frac{4\Gamma_e\Gamma_o}{(\Gamma_e + \Gamma_o + \gamma_m)^2}\eta_M = \frac{4(\Gamma_T - \Gamma_o - \gamma_m)\Gamma_o}{\Gamma_T^2}\eta_M, \tag{4.3}$$

where γ_m and Γ_o are fixed from independent measurements and η_M is the only fit parameter. For our converter $\Gamma_e, \Gamma_o \gg \gamma_m$, and thus $\eta = \eta_M$ when the converter is matched. Therefore we refer to η_M as the matched efficiency. In this low mechanical dissipation regime, there is negligible energy loss in the electro-optic transduction process itself, but some energy is absorbed in each electromagnetic resonator, and the spatial profile of the optical cavity mode does not perfectly match that of the external modes used for measurement and signal injection. This is described in more detail in Section 4.3.2. We thus expect $\eta_M = \epsilon(\kappa_{ext,o}/\kappa_o)(\kappa_{ext,e}/\kappa_e)$, where κ_o and $\kappa_{ext,o}$ (κ_e and $\kappa_{ext,e}$) are the optical (microwave) cavity linewidth and external coupling respectively, and ϵ parameterizes the optical cavity mode matching. The fit result, $\eta_M = 43 \pm 1\%$, agrees with the theoretical expectation, $\eta_M = 43 \pm 4\%$ obtained from independent measurements of ϵ, $\kappa_{ext,o}/\kappa_o$, and $\kappa_{ext,e}/\kappa_e$.

Tuning the membrane position *in situ* within the optical cavity changes both $\kappa_{ext,o}$ and κ_o due to interference effects (see Limitations chapter), and therefore alters the matched conversion efficiency (Figure 4.5b). Matched conversion efficiency initially increases with κ_o, reaching a maximum at $\kappa_o = 2\pi \times 2.7$ MHz, and then decreases as internal optical cavity loss begins to dominate. The *in situ* tuning of the optical cavity also changes the optomechanical coupling and thus the achievable converter bandwidth Γ_T. For intermediate linewidths near the highest efficiencies, the optical cavity became unstable, possibly due to large optomechanical coupling in these regions. The peak conversion efficiency achieved was $47 \pm 1\%$, approaching the quantum feedforward threshold efficiency discussed in Chapter 5. At peak conversion efficiency, the matched converter bandwidth was 12 kHz, while a 100 kHz bandwidth was achieved at $\kappa_o = 2\pi \times 3$ MHz. As a figure of merit, the peak efficiency represents significant technical progress relative to the 8% efficiency achieved in a prototype system operated at 4 K [85].

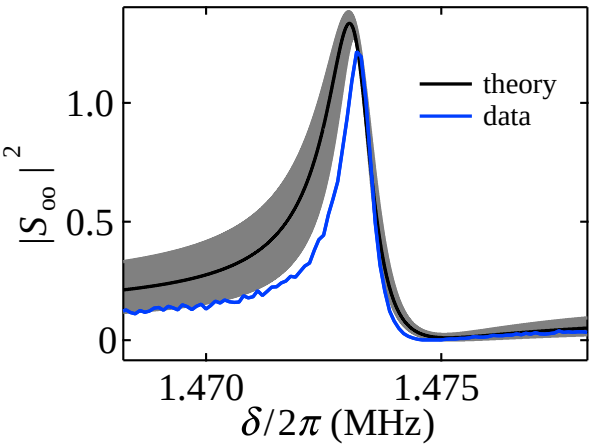

Figure 4.6: **Optical scattering parameter.** Measured scattering parameter of the optical port vs probe frequency δ (blue) showing optomechanically induced transparency. Black line shows expected response from independent parameter measurements. Grey band expresses uncertainty of system parameters.

4.3.1 Optomechanical response theory

Reflection measurements of the optical cavity can be understood using the mechanically mediated state transfer defined in Section 2.3. The optical cavity has a Lorentzian response and shows up as dip in reflection, from which we detune a pump tone and study mechanical response.

Figure 4.6 shows narrow-band measured and expected scattering parameters of the mechanical response for the optical port, with $\Gamma_e \ll \Gamma_o$. Fixing all the cavity and pump parameters in the equations of motion generates a line shape that reproduces salient features observed in the experiment. The peak value exceeds one due to gain from imperfect sideband resolution, and the Fano-like shape arises from the mechanical response not being on the flat bottom of the dip, but on the slope of the optical cavity response (due to $\Delta_o \neq -\omega_m$).

4.3.2 Mode matching and efficiency calibration

Careful calibration of probe-tone scattering measurements requires correctly treating various optical mode matching factors. Mode matching is important for calibration as it affects reflection measurements of the optical port. Specifically, we care about mode matching between input light

and cavity mode, and between the signal and the heterodyne LO beam. Any light that is not properly matching to the mode of the cavity is promptly reflected by the input mirror and does not make it into the cavity. As a result, the measured dip in reflection on resonance will be measured to be smaller than expected We parameterize the mode matching between two optical fields E_1, E_2 of the same polarization by the overlap of the electric fields, given by

$$\epsilon = \frac{\left|\int E_1^* E_2 \mathrm{d}^2x\right|}{\sqrt{\int |E_1|^2 \mathrm{d}^2x \int |E_2|^2 \mathrm{d}^2x}}. \tag{4.4}$$

We can extract the mode matching through a interference measurement. Here, we direct the two beams on to a single photon detector The beams are set to different frequencies and their power is balanced. If the two beams are mode matched, then they will interfere and a beat note will appear on a scope measuring the voltage output of a photo detector as seen in Figure 4.7. The visibility is given by

$$v = \frac{I_{\max} - I_{\min}}{I_{\max} + I_{\min}}, \tag{4.5}$$

where $I_{\max(\min)}$ is the maximum (minimum) intensity of oscillations. The mode matching is the square root of the fringe visibility so that maximal mode matching corresponds to perfect extinction at the fringe minimum.

The converter is calibrated by dividing the transmission in each direction by the off-resonant reflection off each port [85]. In this way the individual gains and losses of the measurement network need not be known, and yet they can still be calibrated out. With this calibration procedure, mode matching ϵ_d between the incident beam and the cavity mode is automatically included in the downconversion efficiency, and mode matching ϵ_u between the outgoing cavity mode and the LO is included in the upconversion efficiency. In practice $\epsilon_\mathrm{u} \approx \epsilon_\mathrm{d}$, and we define the mode matching factor ϵ that appears in the expression for the bidirectional conversion efficiency η_M as $\epsilon = \sqrt{\epsilon_\mathrm{u}\epsilon_\mathrm{d}}$.

We must also account for the imperfect mode matching optical heterodyne measurement ϵ_LO between the local oscillator and the reflection from the optical port, which only affects the off-resonant reflection measurement used to calibrate out path losses. Since ϵ_LO is not an inherent quality of the converter, it should not be included in the measured conversion efficiency, and must

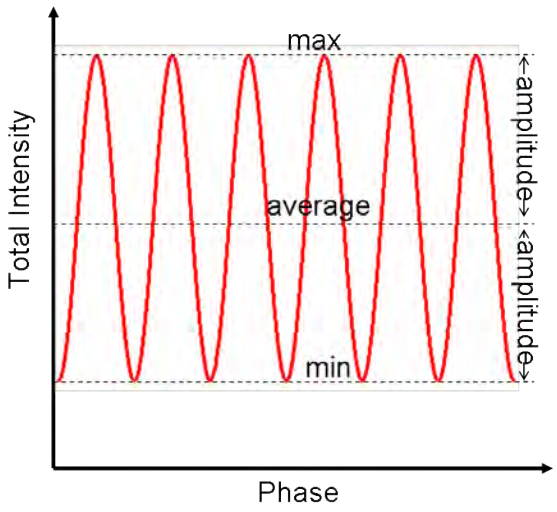

Figure 4.7: **Visibility.** As two tones interfere they create a beat note. The x-axis is the phase of this beat note. The phase can be tied to some physical change in time, for example the end mirror of one arm of a Michelson interferometer moving. A beat note will also show up if the two tones are at slightly different frequency in which case the phase oscillates at the difference frequency between them. Our measurement uses beams of different frequency. Visibility and mode matching are extracted from the maximum and minimum of this curve. Figure from Wikipedia.

be calibrated out separately. An independent measurement of the interference visibility between the LO and a far-detuned beam reflected off the cavity yields $\epsilon_{\mathrm{LO}} = 0.83$, which is similar to $\epsilon = 0.87$ as expected.

4.4 Added noise

Although this device shows exceptional efficiency, that is not the current limiting factor for quantum operation. With efficiency of less than 50% entanglement distillation and heralding [96, 97, 98, 99] could still allow for quantum enabled operation. However, for a device to work in the quantum regime, the noise added by the converter needs to be less than one photon (per photon converted). Heralding and distillation help combat loss but do not address added noise. This strict requirement comes from the fact that quantum signals are not as robust to added noise as classical signals. In classical signals, the signal to noise ratio is what matters, but in quantum signals, even one photon of added noise is enough to destroy the information. For example if you're encoding a

qubit as $0+1$ photon, then 1 photon added noise ruins the fidelity of the qubit.

Due to the high Q of our mechanical resonators, an insignificant amount of information leaks out to the environment through the internal loss of the mechanics. This allows us to easily access a regime where the conversion rate is much higher than the intrinsic damping $\Gamma \gg \gamma_{\mathrm{m}}$. However, the low frequency of the mechanical element means that the thermal occupation of the device is still $n_{\mathrm{th,m}} >> 1$ even at dilution refrigerator temperatures because $k_{\mathrm{B}}T >> \hbar\omega_{\mathrm{m}}$. This means that although the rate for a signal excitation (γ_{m}) lost to the environment is relatively low, the number of phonons leaking into the signal are scaled by the number of phonons in the bath (n_{th}) and therefore there are many opportunities for excitations to degrade the signal. For this reason, to achieve added noise less than one, the damping rate needs to exceed not only the mechanical dissipation rate, but also needs to reach the requirement $\Gamma \gg n_{\mathrm{th}}\gamma_{\mathrm{m}}$. If this requirement is not met, a large portion of the mechanical oscillator's motion will be due to fluctuations from the thermal environment instead of coherent state information from the conversion process, i.e. you transduce these excess phonons in addition to the photons you wanted. In addition to these thermal fluctuations, noise can be added from other technical imperfections.

4.4.1 Measuring added noise

Instead of sweeping a probe tone across resonance to characterize the efficiency, the noise properties are inferred from measuring the power spectral density at the output of the converter. An example of the power spectral density of a upconverted microwave tone measured optically is shown in Figure 4.8. The narrow spike is the signal tone corresponding to converted microwave photons Ideally the spectrum would show only the conversion tone on a flat background which would correspond to no added noise. Instead we see the signal riding on a Lorentzian skirt at the frequency of the mechanical oscillator. This skirt is a measure of how well we are transducing thermo-mechanical motion into optical photons, and is also a measure of the added noise.

Characterization of the added noise is done in the high-stability configuration with $\eta_{\mathrm{M}} = 43\%$ described in Section 4.3. We perform heterodyne measurements of the noise exiting both converter

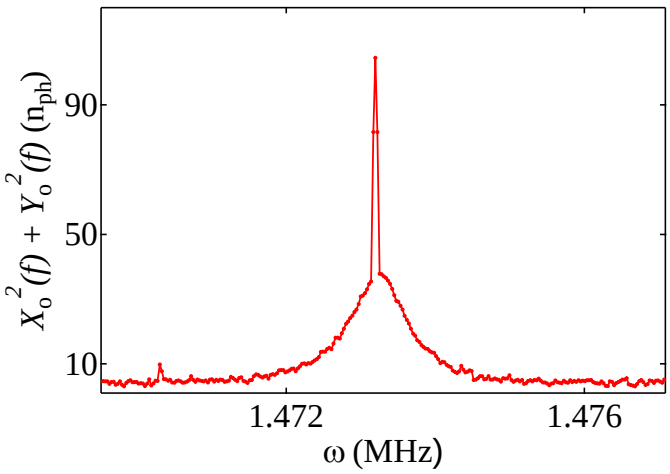

Figure 4.8: **Optical power spectrum,** $X_o^2(\omega) + Y_o^2(\omega)$, for a upconverted microwave signal measured in the optical domain. Narrow spike corresponds to signal while Lorentzian skirt is a measure of the added noise. This is done with $\Gamma_e \approx \Gamma_o$ and $\Gamma_T = 550$ Hz.

ports, and analyze the results in the frequency domain: $X(\omega)$ and $Y(\omega)$ will denote respectively the real and imaginary parts of the Fourier transform of the noise time stream at detuning $+\omega$ from the pump. The total power spectral density is then $S(\omega) = \langle X^2(\omega)\rangle + \langle Y^2(\omega)\rangle$, and is reported in units of photons/s/Hz, or more simply photons, referred to the converter output. For example, an ideal heterodyne measurement of $S(\omega)$ gives a background noise level of 1 photon, and 50% loss in the measurement chain would double the background level. The added noise of the converter can be calculated by

$$N_{\text{add}} = (S(f_m) - 2n_o)/(\mathcal{A} \cdot \eta) \tag{4.6}$$

Where n_o is the single quadrature noise of the optical measurement, and $\mathcal{A}$ is the independently measured converter gain due to imperfect sideband resolution. The added noise depends on calibrations of the measurement chains, and therefore as we approach the threshold for a quantum protocol, $N_{\text{add}} < 1$, these calibrations need to be accurate. Our calibration methods are detailed in Section 4.5.

We record the power spectral density for a range of pump powers. The damping rates are

matched so that efficiency is always maximized. As the pump powers are turned up, the conversion rate increases relative to the fixed thermal decoherence rate. In this way the added noise peak is broadened and the peak height is reduced due to cooling of the mechanical oscillator. As shown in Figure 4.9, increasing the total damping, Γ_{T}, while maintaining matching, $\Gamma_{\mathrm{e}} \approx \Gamma_{\mathrm{o}}$, improves noise performance while increasing bandwidth. The peak center frequency moves down due to the optical spring effect [62]. Ideally we would keep turning up the pumps until the high cooperativity regime is reached and the added noise was below one photon. However, Figure 4.9 also shows how technical noise is limiting the performance. Starting at the lowest bandwidth, as the conversion rate is doubled the height of the peak drops by a factor of two as expected. When the bandwidth is doubled to the highest shown bandwidth, the peak height is no longer reduced by the same factor. This is the consequence of technical noise sources from the strong pump tones and is explored further in Chapter 6.

For reporting noise performance of the converter, the relevant metric is noise referred to converter input (right side of Figure 4.9). This reference point allows us to quote the added noise of our device independent of measurement chain noise, but importantly it takes into account the converter efficiency. A poor efficiency will correspond to a worse added noise for all else being equal. The added noise can be calculated using Eqn. 4.6 from the output noise on resonance by dividing by the apparent converter efficiency, $\mathcal{A} \cdot \eta$. For this device, laser cooling achieved a best value of $N_{\mathrm{add}} = 34$ photons of input-referred added noise. Again, this figure of merit represents significant technical progress relative to the 1500 photons of added noise achieved in a prototype system operated at 4 K [85].

4.4.2 Mechanical dissipation and added noise

In the presence of technical noise that limits damping rates, the performance of laser cooling is set by $n_{\mathrm{th,m}}\gamma_{\mathrm{m}}$, where $n_{\mathrm{th,m}}$ is the thermal phonon occupancy of the membrane. This means reductions to the added noise could be achieved by cooling the mode or by decreasing the mechanical dissipation. Ideally, the final membrane phonon occupancy $n_{\mathrm{f,m}}$ scales as $n_{\mathrm{th,m}}\gamma_{\mathrm{m}}/\Gamma_{\mathrm{T}}$. At $\Gamma_{\mathrm{T}}/2\pi =$

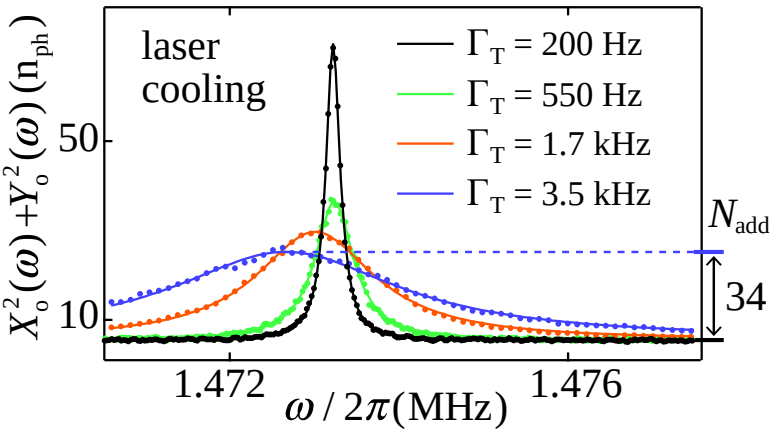

Figure 4.9: **Laser Cooling. e,** Total noise power spectra, $X_o^2(\omega)+Y_o^2(\omega)$, for different laser cooling rates, Γ_T, while maintaining $\Gamma_e \approx \Gamma_o$. Best added noise in photons referred to converter input, N_{add}, indicated on right axis.

3.5 kHz, laser cooling reduced the membrane's phonon occupancy from $n_{th,m} \approx 1200$ to a best value of $n_{f,m} = 18.6$. Laser cooling the mechanical mode is limited by technical noise, but another way to improve the added noise metric is by reducing γ_m so that phonons leak in at a slower rate. Indeed, we have studied laser cooling in a different converter with 10 times lower mechanical dissipation but a lower conversion efficiency of 12%, and achieved an $N_{add} = 13$ photons of added noise. This device is not highlighted as much in this thesis because of the low efficiency, but it is important to highlight as it is the lowest added noise yet achieved.

4.4.3 Operating without matching criteria for technical noise reduction

With the strong pump powers needed for our experiment, two distinct effects lead to excess noise within the LC circuit bandwidth. First, we observe excess phase noise on resonance which scales with the microwave pump power and overwhelms the intrinsic phase noise of the pump signal generator. We also observe excess noise in the LC circuit that scales with the total laser power incident on the membrane, to which both the lock beam and the optical pump contribute. Both of these effects are explored in more detail in chapters 6 and 7. Without any further mention of their

cause we point out a way to address technical noise in converters. If the technical noise is due to one pump more than the other, then the added noise can be reduced by reducing power on that pump and compensating for it with the other. If one of the microwave or optical pumps contributes more technical noise than the other, then the added noise can be reduced by reducing power on that pump and compensating for it by increasing the other to keep the total converter bandwidth constant. In this way the added vibrational noise is constant, but the technical noise is reduced. However, this reduction does not come for free. By moving away from the matched condition, the efficiency reduces which impacts the added noise referred to converter input. Because the efficiency reduces as $1/\Gamma_{e,o}$ (see Eq. 4.3), this approach only helps if the technical noise scales higher than monotonically with the damping rate.

4.5 Measurement efficiency calibrations

The performance quoted is sensitive to the calibration of the microwave and optical measurement chain and is therefore detailed here. The scattering parameters are nearly self calibrating up to some factors of gain and mode matching, but added noise depends on independent calibrations of the measurement chains. The goal of the calibration is to find the efficiency after the output of the converter. Many microwave amplifier characterizations are done with a known noise source at the input of the amplifier by varying the temperature of a resistor [100]. Comparing the measured noise to the expected allows for a calibration in terms of photons at the amplifier input. For our device, we use the mechanical bath as the known noise source. As the base temperature of the fridge is swept, the occupation of the thermal bath that the mechanics couples to varies. This signal along with independent measurements of the cavity parameters allows us to calibrate the measured signal peak height to the expected number of photons at the device. The calibration and consistency checks are described in detail here.

4.5.1 Microwave and optical calibrations

A temperature sweep of the base plate of the dilution refrigerator is used to calibrate output-referred noise spectra like those shown in Figure 4.10. Raw spectra are normalized to the noise level with the pump off, to which the only contributions are vacuum noise and measurement chain added noise; the peak height is σ in these units. The peak exhibits a linear temperature dependence due to the thermally driven motion of the mechanical oscillator (figure 4.10), except at the lowest temperatures where the membrane evidently falls out of equilibrium with the dilution refrigerator (open circles, Figure 4.10c and d). The temperature below which the membrane falls out of equilibrium is higher in the optical measurement, indicating that optical heating is a significant factor below $T = 100$ mK. We find that this membrane heating occurs whenever the locking beam is introduced, but is independent of damping power, consistent with the observations in Ref. [90].

The spectra are calibrated by fitting the observed peak heights $\sigma(T)$ to an expected linear dependence obtained from combining the full optomechanical equations of motion [85] with independently measured parameters in Table 4.1 [92]. The only fit parameter is a proportionality factor that converts uncalibrated thermal peaks to units of photons at the converter output; the normalization of the uncalibrated spectra implies that the single-quadrature background noise (vacuum noise plus measurement chain added noise) is simply given by the calibration factor for each measurement. This procedure yields a single-quadrature background noise $n_{\mathrm{e}} = 29.6$ photons at the microwave output port and $n_{\mathrm{o}} = 2.7$ photons at the optical output port. Inverting this calibration procedure, we can associate the number of output-referred photons on resonance in spectra with an effective mechanical bath temperature.

The microwave cavity coupling ratio $\kappa_{\mathrm{ext,e}}/\kappa_{\mathrm{e}}$ is easily measured using the HF2LI as a network analyzer (see Section 4.1.1). The optical cavity parameters are needed to predict the optical field output noise using optomechanical theory [62]. The mode matching between the cavity and the pump beam is obtained by directing a transmitted beam and the reflected pump onto the heterodyne detector, and measuring the visibility of the resulting interference pattern (see Section 4.3.2). The

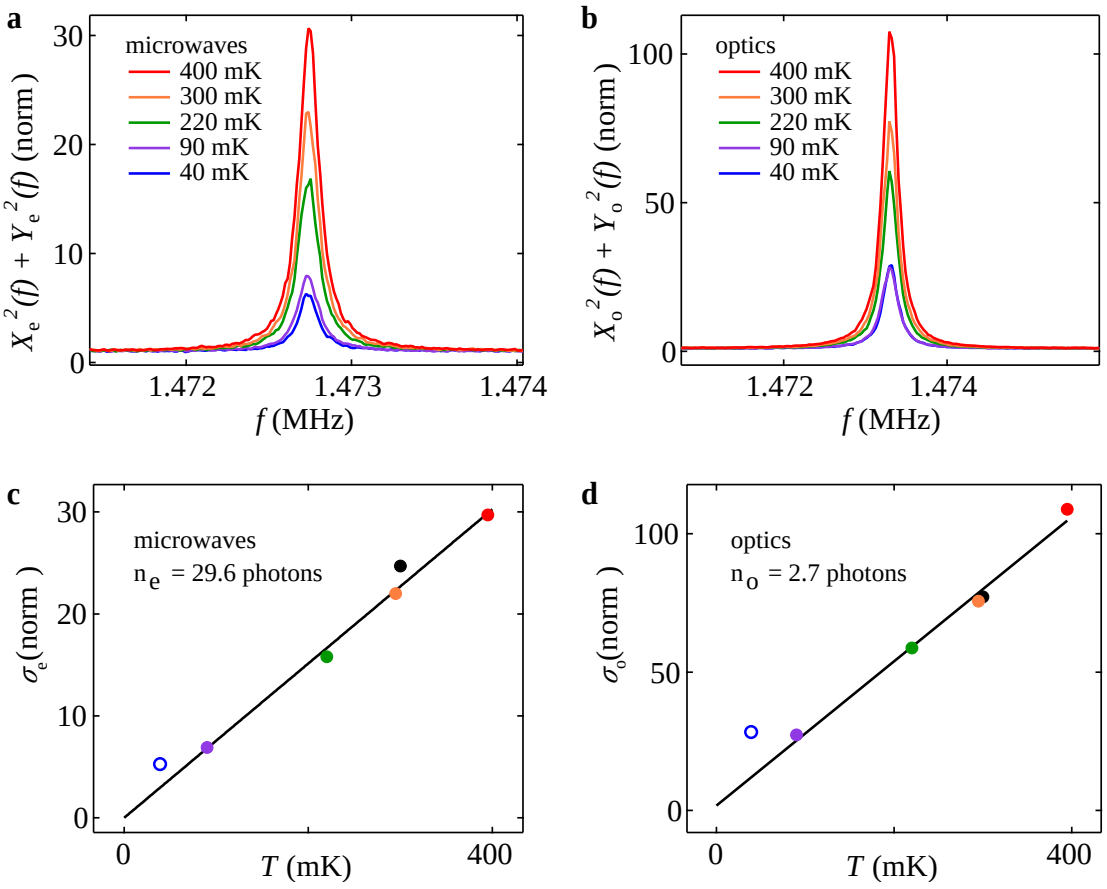

Figure 4.10: **Temperature sweep for calibrations.**(a) Total microwave noise power spectra, $X_e^2(f)+Y_e^2(f)$, shown for a range of base plate temperatures. Optical pump off. Noise is normalized to unity with pumps off. (b) Total optical noise power spectra, $X_o^2(f) + Y_o^2(f)$, shown for a range of base plate temperatures, with the same normalization procedure. Microwave pump off. (c) Microwave peak height σ_e vs. temperature T, with a single-parameter linear fit to extract total noise (see text). Open data point, indicating imperfect thermalization to the cryostat at low temperature, is excluded from fit. (d) Optical peak height σ_o vs. temperature T, with a similar fit. Open data point, indicating imperfect thermalization to the cryostat at low temperature, is excluded from fit.

optical cavity linewidth is measured by sweeping a probe with two sidebands at a known frequency through resonance. The optical cavity coupling ratio $\kappa_{\mathrm{ext,o}}/\kappa_{\mathrm{o}}$, which is used to determine $\kappa_{\mathrm{ext,o}}$ in Table 4.1, is then fixed based on the measured converter efficiency. As a check, $\kappa_{\mathrm{ext,o}}/\kappa_{\mathrm{o}}$ is independently extracted from reflection and transmission measurements of both ports of the optical cavity [101]. This procedure yields $\kappa_{\mathrm{ext,o}}/\kappa_{\mathrm{o}} = 0.53$, which can also be used to determine the expected microwave-optical conversion efficiency, $\epsilon(\kappa_{\mathrm{ext,o}}/\kappa_{\mathrm{o}})(\kappa_{\mathrm{ext,e}}/\kappa_{\mathrm{e}}) = 43 \pm 4\%$.

4.5.2 Checking the consistency of the calibrations

As a check of the optical calibration, we independently measure the optical path loss and heterodyne detector dark noise. This measurement gives an effective transmission of 16%, or equivalently an expected single-quadrature background noise of $(1/4 \times 2) \times 1/0.16 = 3.1$ photons, where the three factors correspond to the single-quadrature vacuum variance, inefficiency of an ideal heterodyne detector, and effective loss, respectively. The added noise Figure 4.9 is a two quadrature measurement and therefore has a background value $2n_{\mathrm{o}}$. This is in reasonable agreement with the thermal calibration.

As a check of the microwave calibration, the amplifier chain can be characterized by measuring off-resonance noise, as shown in Figure 4.11. Data are fit to

$$S_{\mathrm{out}} = G\left(\frac{1}{2}\coth\left(\frac{hf}{2k_{\mathrm{B}}T}\right) + N_{\mathrm{HEMT}}\right), \tag{4.7}$$

where the two fit parameters are the gain G and two-quadrature receiver added noise N_{HEMT}, which we expect is dominated by the added noise of the HEMT preamplifier. We obtain $N_{\mathrm{HEMT}} = 20$ photons, which implies 10 photons of added noise in a single-quadrature measurement. Comparing this result to the single-quadrature noise in Section 4.5.1, $n_{\mathrm{e}} = 29.6$ photons, naively implies 4.6 dB of loss from the LC circuit output to the effective cold load, a somewhat high value. This loss inference should be treated with caution, as the temperature sweep in Figure 4.11 was performed with some stages of the dilution refrigerator slightly colder, which lowers total chain noise compared to Figure 4.10.

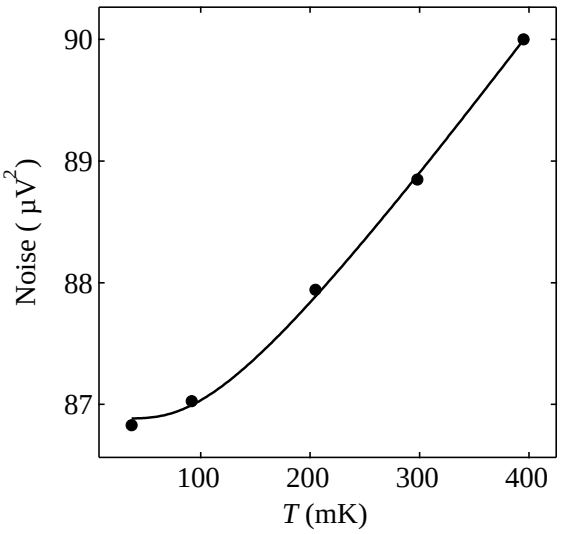

Figure 4.11: **Microwave chain noise for calibration check.** Noise measured in the microwave domain off LC resonance as temperature is varied, fit to Eq. 4.7.

Chapter 5

Correlations and Feedforward

This chapter focuses on the experimental identification of correlations in the noise at each port of the converter. A feedforward protocol harnesses the discovery that noise emitted from the two converter output ports is strongly correlated because both outputs record thermal motion of the same mechanical mode as introduced in Section 5.1. The mathematical framework needed to understand the correlations is examined in Section 5.2. An experimental demonstration in Section 5.3 leverages the correlations to reduce the added noise. Section 5.4 discusses the theory of feedforward and shows that a quantum feedforward protocol that, given high system efficiencies, would allow quantum information to be transferred even when thermal phonons enter the mechanical element faster than the electro-optic conversion rate.

5.1 Feedforward introduction

We consider classical and quantum feedforward protocols in a microwave-mechanical-optical converter in which the mechanical element is thermally occupied (figure 5.1a). When the mechanical oscillator coupling rate to the hot bath is small compared to the opto-electromechanical damping rates, the thermal bath acts as classical random force on the oscillator. The force noise is then present in both the optical and electrical fields exiting the converter, and as such measuring them in the electrical domain should permit you to remove them in the optical domain. During operation, the signal to be converted is injected into the microwave port and an ancilla state is injected into the optical port. The upconverted signal, with noise added, is emitted from the optical port.

The ancilla state, contaminated with the same added noise, is emitted from the microwave port. Measuring the downconverted ancilla and feeding forward to the propagating optical mode can remove this correlated added noise.

Classical and quantum feedforward protocols are distinguished by the choice of ancilla. Simply choosing the ancilla to be optical vacuum causes zero-point fluctuations (vacuum noise) to be fed forward along with the thermal noise. In this case, although thermal noise may be completely removed, vacuum noise from the ancilla is necessarily written onto the upconverted signal. Choosing vacuum as the ancilla therefore prohibits upconversion of a state with negative Wigner function or squeezing, so we refer to it as classical feedforward. Classical feedforward is a resource for recovering classical signals, whose performance — interestingly — depends on system efficiencies rather than temperature, quality factor, or cooperativity. However, classical feedforward is unhelpful for quantum tasks.

A different choice of ancilla would allow quantum tasks to be accomplished, even in the presence of thermal noise. For example if the ancilla is an infinitely squeezed vacuum state, one quadrature can be fed forward noiselessly, permitting noiseless measurement of a single upconverted quadrature or upconversion of a squeezed quadrature without high cooperativity. This quantum protocol does however place limits on measurement and converter efficiencies, as any loss will add noise to the feedforward process. In the limit of perfect measurement efficiencies and squeezing, a converter efficiency $\eta > 50\%$ is still required to upconvert a squeezed quadrature or measure a remotely prepared microwave quadrature with added noise less than vacuum. We therefore refer to 50% as a quantum threshold efficiency for feedforward protocols. More sophisticated tasks can be imagined with quantum feedforward, albeit with more stringent efficiency requirements. In particular, quantum feedforward could be used to upconvert a qubit state given a qubit encoding robust to noise in one quadrature. One example of such a feedforward-based qubit upconversion scheme is explored in Section 5.4.3.

Experimentally we focus on the identification of correlations that allow feedforward, and perform classical feedforward with a vacuum ancilla. For this demonstration we measure both

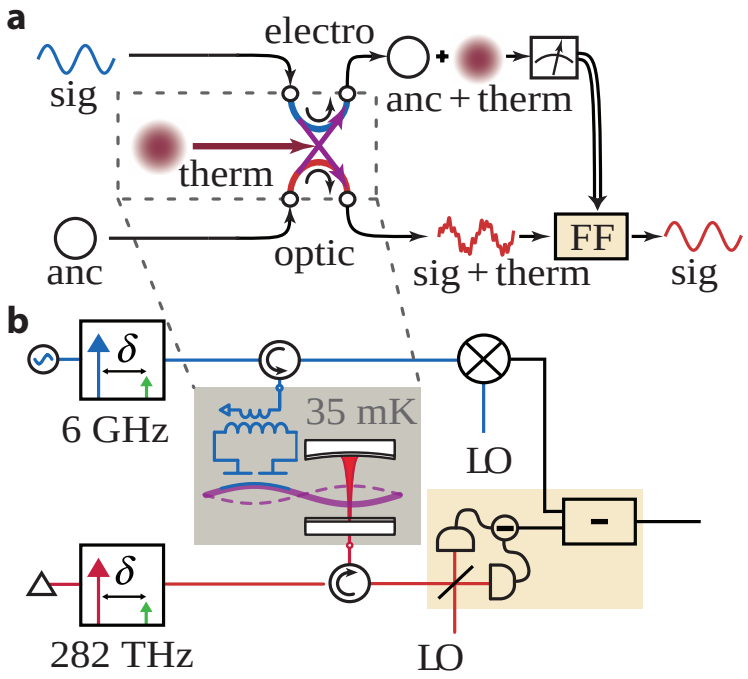

Figure 5.1: **Feedforward schematic and measurement network. a,** A signal incident on the microwave port (blue sinusoid) is output from the optical port (red sinusoid) with thermal noise coupled in from the internal port (maroon disk). Optical ancilla (black circle) is simultaneously downconverted with correlated noise added. The ancilla is measured and a feedforward protocol (FF) is applied. Dotted line is the converter box. Blue and red arrows show microwave and optical reflections, and purple arrows show conversion process. **b,** Feedforward operations are indicated by beige-shaded regions. For our classical demonstration these operations are optical heterodyne measurement and subtraction in post-processing. The corresponding operation in a quantum feedforward protocol would be a unitary displacement of the optical field conditioned on the microwave measurement result.

converter outputs in heterodyne detection and perform subtraction in post-processing to remove the correlated noise (figure 5.1b). A quantum protocol would instead entail homodyne measurement of the ancilla at the microwave port, and conditional unitary displacement at the optical port [102].

5.2 Electro-optic correlation theory

Here the full input output formalism developed in Section 2.3 is leveraged to describe the correlations in noise from each port.

Spectra of the output fields are expressed in terms of a matrix $\mathbf{S}(\omega)$, whose elements are given by

$$S_{ij}(\omega)\delta(\omega-\omega') = \frac{1}{2}\langle\{[\mathbf{a}_{\mathrm{out},i}(\omega')]^\dagger, \mathbf{a}_{\mathrm{out},j}(\omega)\}\rangle, \tag{5.1}$$

where $\mathbf{a}_{\mathrm{out}} = (\hat{a}_{\mathrm{out,B}}, \hat{a}_{\mathrm{out,F}}, \hat{b}_{\mathrm{out}}, \hat{a}^\dagger_{\mathrm{out,B}}, \hat{a}^\dagger_{\mathrm{out,F}}, \hat{b}^\dagger_{\mathrm{out}})^T$ is a vector of optical ($\hat{a}_{\mathrm{out}}$) and microwave ($\hat{b}_{\mathrm{out}}$) output field operators. For completeness optical operators are written for both the front, $\hat{a}_{\mathrm{out,F}}$, and back, $\hat{a}_{\mathrm{out,B}}$, optical ports, but in most of this thesis we make single port measurements and therefore the front port is simply referred to as 'external,' as it is the only port where signals are measured, and the back port is included in the loss budget. Output fields are related to input fields by the matrix $\mathbf{\Xi}(\omega)$, $\mathbf{a}_{\mathrm{out}}(\omega) = \mathbf{\Xi}(\omega)\mathbf{a}_{\mathrm{in}}(\omega)$, calculated from linearized equations of motion following Ref. [85]. Here

$$\mathbf{a}_{\mathrm{in}} = \left(\hat{a}_{\mathrm{in,B}}, \hat{a}_{\mathrm{in,F}}, \hat{a}_{\mathrm{in,int}}, \hat{b}_{\mathrm{in,ex}}, \hat{b}_{\mathrm{in,int}}, \hat{c}_{\mathrm{in}}, \hat{a}^\dagger_{\mathrm{in,B}}, \hat{a}^\dagger_{\mathrm{in,F}}, \hat{a}^\dagger_{\mathrm{in,int}}, \hat{b}^\dagger_{\mathrm{in,ex}}, \hat{b}^\dagger_{\mathrm{in,int}}, \hat{c}^\dagger_{\mathrm{in}}\right)^T \tag{5.2}$$

is a vector of input fields for optical ($\hat{a}_{\mathrm{in}}$), microwave ($\hat{b}_{\mathrm{in}}$), and mechanical ($\hat{c}_{\mathrm{in}}$) modes.

In terms of input fields, the spectral matrix is then

$$\mathbf{S}(\omega)\delta(\omega-\omega') = \frac{1}{2}\mathbf{\Xi}^*(\omega')\left(\langle[\mathbf{a}_{\mathrm{in}}(\omega')]^\dagger\mathbf{a}^T_{\mathrm{in}}(\omega)\rangle + \langle[\mathbf{a}_{\mathrm{in}}(\omega)[\mathbf{a}^T_{\mathrm{in}}(\omega')]^\dagger]^T\rangle\right)\mathbf{\Xi}^T(\omega), \tag{5.3}$$

where transposes act only on matrices and adjoints act only on operators. The input fields are thermal states, satisfying for example $\langle[c_{\mathrm{in}}(\omega')]^\dagger c_{\mathrm{in}}(\omega)\rangle = \delta(\omega-\omega')n_{\mathrm{th,m}}$ and $\langle c_{\mathrm{in}}(\omega)[c_{\mathrm{in}}(\omega')]^\dagger\rangle = \delta(\omega-\omega')(n_{\mathrm{th,m}}+1)$, where $n_{\mathrm{th,m}}$ is the number of thermal phonons in the mechanical oscillator.

Integrating over ω', Eq. 5.3 can then be rewritten

$$\mathbf{S}(\omega) = \frac{1}{2}\mathbf{\Xi}^*(\omega)\mathbf{\Xi}^T(\omega) + \mathbf{\Xi}^*(\omega)\mathbf{\Sigma}\mathbf{\Xi}^T(\omega). \tag{5.4}$$

The first term originates from quantum noise of the input modes, whereas the second is a thermal contribution that vanishes at zero temperature, due to the fact that

$$\mathbf{\Sigma} = \begin{pmatrix} \mathbf{N} & 0 \\ 0 & \mathbf{N} \end{pmatrix}, \tag{5.5}$$

where $\mathbf{N} = \mathrm{Diag}[n_{\mathrm{th,o}}, n_{\mathrm{th,o}}, n_{\mathrm{th,o}}, n_{\mathrm{th,e}}, n_{\mathrm{th,e}}, n_{\mathrm{th,m}}]$ is a diagonal matrix of thermal noise contributed by each input mode.

Note that the diagonal entries of $\mathbf{S}(\omega)$ are real, whereas the off-diagonal components are in general complex. In terms of quantities measured, for example, $[\hat{a}_{\mathrm{out,F}}(\omega)]^\dagger \hat{a}_{\mathrm{out,F}}(\omega) = X_{\mathrm{o}}^2 + Y_{\mathrm{o}}^2$, whereas

$$[\hat{a}_{\mathrm{out,F}}(\omega)]^\dagger \hat{b}_{\mathrm{out}}(\omega) = X_{\mathrm{o}}X_{\mathrm{e}} + Y_{\mathrm{o}}Y_{\mathrm{e}} + iX_{\mathrm{o}}Y_{\mathrm{e}} - iY_{\mathrm{o}}X_{\mathrm{e}}. \tag{5.6}$$

In practice one can adjust the optical and microwave demodulator phases to make all entries real, which corresponds to removing X-Y microwave-optical correlations, $\langle X_{\mathrm{o}}Y_{\mathrm{e}}\rangle = \langle Y_{\mathrm{o}}X_{\mathrm{e}}\rangle = 0$. In the experiment, the demodulator phases are adjusted to approximately fulfill this condition.

While the full expressions for the matrix elements of Eq. 5.4 are cumbersome, in the limit of optimal detuning ($\Delta_{\mathrm{o}} = \Delta_{\mathrm{e}} = -\omega_{\mathrm{m}}$), weak damping ($\Gamma_{\mathrm{e}}, \Gamma_{\mathrm{o}} \ll \kappa_{\mathrm{e}}, \kappa_{\mathrm{o}}$), and resolved sidebands ($\kappa_{\mathrm{o}}, \kappa_{\mathrm{e}} \ll \omega_{\mathrm{m}}$), on mechanical resonance the electro-optic correlations take the simple form

$$\mathbf{S}_{\mathrm{eo}}(\omega_{\mathrm{m}}) = \frac{1}{2}\mathbb{I}_2 + \mathbf{S}^{(\mathrm{th})}(\omega_{\mathrm{m}}), \tag{5.7}$$

$$\mathbf{S}^{(\mathrm{th})}(\omega_{\mathrm{m}}) = \frac{4n_{\mathrm{th,m}}\gamma_{\mathrm{m}}}{(\Gamma_{\mathrm{o}} + \Gamma_{\mathrm{e}} + \gamma_{\mathrm{m}})^2} \begin{pmatrix} \Gamma_{\mathrm{o}} & \sqrt{\Gamma_{\mathrm{o}}\Gamma_{\mathrm{e}}} \\ \sqrt{\Gamma_{\mathrm{e}}\Gamma_{\mathrm{o}}} & \Gamma_{\mathrm{e}} \end{pmatrix}, \tag{5.8}$$

where $\mathbb{I}_2$ is the 2x2 identity, representing the contribution of quantum noise. The diagonal elements of $\mathbf{S}^{(\mathrm{th})}$ have a straightforward interpretation. Thermal noise added to the optical output mode, $S_{1,1}^{(\mathrm{th})}$, is due to the resonant transmission of mechanical noise $n_{\mathrm{th,m}}$ from the bath, coupled at rate γ_{m}, to the optical mode, coupled at rate Γ_{o}. Similarly, thermal noise added to the microwave output

mode, $S_{2,2}^{(\mathrm{th})}$, is due to the resonant transmission of mechanical noise from the bath to the microwave mode, coupled at rate Γ_e. Since the mechanical resonator couples to the optical, microwave, and bath modes, its total linewidth is $\Gamma_\mathrm{o} + \Gamma_\mathrm{e} + \gamma_\mathrm{m}$.

The elements of $\mathbf{S}^{(\mathrm{th})}$ satisfy the property

$$S_{1,2}^{(\mathrm{th})} = \sqrt{S_{1,1}^{(\mathrm{th})} S_{2,2}^{(\mathrm{th})}}. \tag{5.9}$$

As a consequence, the smallest eigenvalue of $\mathbf{S}_\mathrm{eo}$ is equal to 1/2 photon. If $S_{1,2}^{(\mathrm{th})}$ were to exceed $\sqrt{S_{1,1}^{(\mathrm{th})} S_{2,2}^{(\mathrm{th})}}$ in magnitude, then the smallest eigenvalue of $\mathbf{S}_\mathrm{eo}$ would be less than 1/2 photon, signaling the presence of two-mode squeezing. Eq. 5.9 therefore represents the condition for maximal classical correlations, as they are as large as possible without implying the presence of squeezed quantum noise.

While Eq. 5.8 is derived under restricted assumptions, we have verified numerically that Eq. 5.9 is satisfied for arbitrary detunings and linewidths, including for the system parameters reported in Table 4.1. Interestingly, the property $S_{1,1}^{(\mathrm{th})} = S_{2,2}^{(\mathrm{th})}$ can also be obtained under more general conditions, provided an appropriate detuning is used. For instance, if we had instead chosen $\Delta_\mathrm{o} = -0.38$ MHz but kept all other parameters the same as Table 4.1 we would have obtained $S_{1,1}^{(\mathrm{th})} = S_{2,2}^{(\mathrm{th})}$ at the expense of weaker optomechanical damping per incident photon.

Importantly, imperfect sideband resolution does not weaken the strength of the classical correlations. With imperfect sideband resolution, arbitrary detunings, and cavity loss, the correlation matrix still can still be written in the form

$$\mathbf{S}_\mathrm{eo}(\omega_\mathrm{m}) = \frac{1}{2}\mathbb{I}_2 + \mathbf{S}'(\omega_\mathrm{m}), \tag{5.10}$$

with $\mathbf{S}'$ satisfying

$$S'_{1,2} = \sqrt{S'_{1,1} S'_{2,2}}. \tag{5.11}$$

The correlations are still classically maximal, but, in contrast to Eq. (5.9), there are now contributions both from thermal and quantum noise.

5.3 Feedforward harnesses correlations to reduce added noise

We now turn to experimental measurements of the correlations in the noise and explore a classical feedforward in a microwave-mechanical-optical converter in which the mechanical element is thermally occupied (figure 5.1). In order to explore correlations in this noise, we turn off the weak probe tone and again work in a high-stability configuration with $\eta_{\mathrm{M}} = 43\%$, but smaller pump power ($\Gamma_{\mathrm{e}} \approx \Gamma_{\mathrm{o}}$, $\Gamma_{\mathrm{T}} = 2\pi \times 200$ Hz). In this configuration electro/optomechanical cooling of the mechanical mode is diminished, while still maintaining $\Gamma_{\mathrm{e}}, \Gamma_{\mathrm{o}} \gg \gamma_{\mathrm{m}}$.

The microwave real power spectral density, $\langle X_{\mathrm{e}}(\omega) X_{\mathrm{e}}(\omega) \rangle$, exhibits a peak of width $\Gamma_{\mathrm{T}}/2\pi =$ 200 Hz around $\omega/2\pi = f_{\mathrm{m}}$ (figure 5.2a). The peak height relative to background, $\langle (X_{\mathrm{e}}^{(\mathrm{th})})^2 \rangle =$ 69.2 photons, is obtained from a Lorentzian fit to the data and attributed to thermally driven mechanical motion at a bath temperature $T = 87 \pm 4$ mK (see 4.5), which exceeds the cryostat base temperature of 35 mK. The elevated membrane temperature is consistent with independently measured optical heating (see 4.5). The background noise level, 31.8 photons, corresponds to $n_{\mathrm{e}} = 29.6$ photons from vacuum noise and the added noise of the microwave measurement chain, with the remaining 2.2 photons due primarily to parameter noise in the LC circuit (independently calibrated, see 6.1.1).

The optical real spectral density, $\langle X_{\mathrm{o}}(\omega) X_{\mathrm{o}}(\omega) \rangle$, shows a similar peak (figure 5.2b). The peak height above noise, $\langle (X_{\mathrm{o}}^{(\mathrm{th})})^2 \rangle = 33.1$ photons, provides a second measure of the bath temperature, $T = 80 \pm 4$ mK, consistent with Figure 5.2a. The background noise, $n_{\mathrm{o}} = 2.7$ photons, corresponds to vacuum noise plus the effect of loss in the optical measurement chain. Note that $n_{\mathrm{o}} < n_{\mathrm{e}}$, indicating that the optical measurement apparatus is closer to ideal.

The real cross-spectral density, $\langle X_{\mathrm{e}}(\omega) X_{\mathrm{o}}(\omega) \rangle$, has a 47.7 photon peak at $\omega/2\pi = f_{\mathrm{m}}$, indicating that the thermal fluctuations are common to both outputs (figure 5.2c). The difference between the observed correlations and their maximum classical value, $\langle X_{\mathrm{e}} X_{\mathrm{o}} \rangle - \sqrt{\langle (X_{\mathrm{e}}^{(\mathrm{th})})^2 \rangle} \sqrt{\langle (X_{\mathrm{o}}^{(\mathrm{th})})^2 \rangle} =$ -0.2 ± 0.3 photons, is consistent with zero, indicating that thermal noise is perfectly correlated between the two outputs, as expected from optomechanical theory. Away from mechanical res-

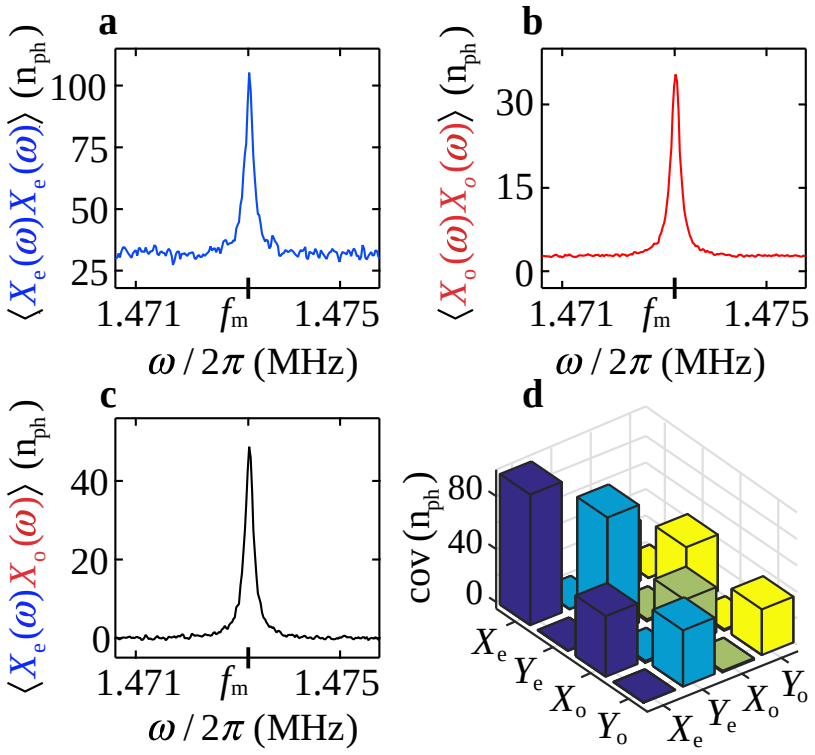

Figure 5.2: **Electro-optic correlations.** **a,** Microwave real spectral density, $\langle X_e(\omega)X_e(\omega)\rangle$, in units of photons referred to converter output, showing thermal-mechanical noise peak and background noise from microwave measurement chain. **b,** The optical real spectral density, $\langle X_o(\omega)X_o(\omega)\rangle$, exhibits similar features. **c,** Real cross-spectral density, $\langle X_e(\omega)X_o(\omega)\rangle$, illustrating that thermal noise exhibits perfect classical correlations between outputs and background noise is uncorrelated. **d,** Covariance matrix obtained from averaging the spectral and cross-spectral densities around ω_m with a $2\pi \times 50$ Hz bandwidth, indicating similar behavior for the imaginary microwave and optical spectral densities and the imaginary cross-spectral density; no correlations exist between real and imaginary parts.

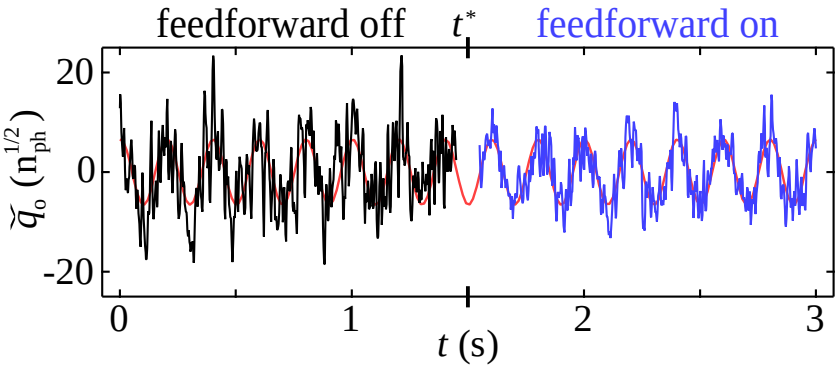

Figure 5.3: **Time domain feedforward.** Fed-forward optical quadrature $\check{q}_\mathrm{o}$ versus time with feedforward off ($t < t^*$) and feedforward on ($t > t^*$). A weak signal incident on the microwave port is recovered at the optical port. Red trace shows what signal form should be to guide eye.

onance the cross-correlation vanishes, as expected for uncorrelated noise from the independent measurement chains. Similar behavior is observed for $\langle Y_\mathrm{e}(\omega)Y_\mathrm{o}(\omega)\rangle$. The full covariance matrix (figure 5.2d), obtained from averaging the spectral and cross-spectral densities around ω_m with a $2\pi \times 50$ Hz bandwidth, shows that the imaginary spectral densities are also positively correlated, but that no correlations exist between real and imaginary parts due to our choice of demodulator phase

Harnessing the observed correlations, we use classical feedforward to recover a weak upconverted signal (figure 5.1). With the weak signal incident on the microwave port and detuned from the pump by $\delta/2\pi = f_\mathrm{m} + 5$ Hz, microwave reflection and converter transmission to the optical port are simultaneously measured. The microwave reflection is fed forward to remove noise from the upconverted optical signal. In a quadrature picture where demodulated microwave and optical fields are described in the time domain by $(q(t), p(t))$ position-momentum pairs, the fed-forward optical quadrature $\check{q}_\mathrm{o}$ is given by

$$\check{q}_\mathrm{o} = q_\mathrm{o} - w\sqrt{\frac{n_\mathrm{o}}{n_\mathrm{e}}}q_\mathrm{e}, \tag{5.12}$$

where q_o is the measured optical quadrature, q_e is the microwave quadrature, n_e (n_o)is the added noise of the microwave (optical) measurement chain, and w is the feedforward weight; a similar definition is used for $\check{p}$.

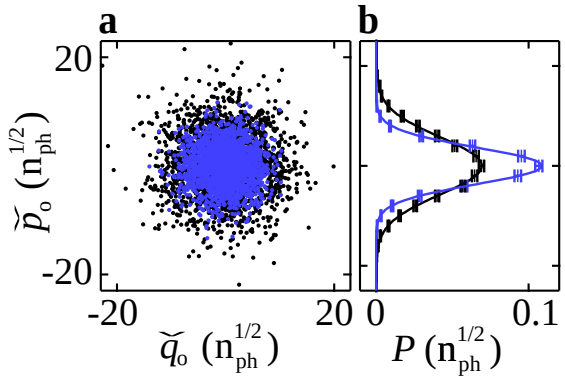

Figure 5.4: **Feedforward variance.** **a,** Repeated measurements of both optical quadratures $(\check{q}_o, \check{p}_o)$ with and without feedforward. Signal tone turned off. **b,** $P(\check{p}_o)$, the inferred probability density of $\check{p}_o$, with and without feedforward, with Gaussian fits. The variance decreases by 59% with feedforward on. Error bars obtained from Poisson counting statistics.

Initially, with feedforward turned off ($w = 0$ for $t < t^*$), the upconverted signal, a $2\pi \times 5$ Hz quadrature oscillation, is difficult to resolve (figure 5.3). After feedforward is turned on ($w = 1.6$ for $t > t^*$), the weak signal becomes clearly visible. The red line is on the figure to help guide the eye and does not represent real data. To quantify the improvement, the optical quadratures $(\check{q}_o, \check{p}_o)$ are repeatedly measured without a signal tone, as shown in Figure 5.4a. The quadratures are Gaussian distributed (figure 5.4b), and feedforward reduces each quadrature variance by 59%.

Feedforward performance is limited mainly by the addition of uncorrelated noise from imperfect measurement chains. This limitation can be understood by examining the power spectral density of the feedforward signal, $\langle \check{X}_o^2 \rangle + \langle \check{Y}_o^2 \rangle$, where

$$\langle \check{X}_o^2 \rangle = \langle X_o^2 \rangle + w^2 \frac{n_o}{n_e} \langle X_e^2 \rangle - 2w \sqrt{\frac{n_o}{n_e}} \langle X_e X_o \rangle, \tag{5.13}$$

$$\langle \check{Y}_o^2 \rangle = \langle Y_o^2 \rangle + w^2 \frac{n_o}{n_e} \langle Y_e^2 \rangle - 2w \sqrt{\frac{n_o}{n_e}} \langle Y_e Y_o \rangle, \tag{5.14}$$

in terms of the measured real and imaginary spectral densities. As shown in Figure 5.5, as the feedforward weight w is increased, the peak noise power near f_m decreases due to the presence of correlations near mechanical resonance. However, Figure 5.5 also illustrates that the noise power off resonance increases with increasing w. At $w = 1$, the background noise receives equal contributions

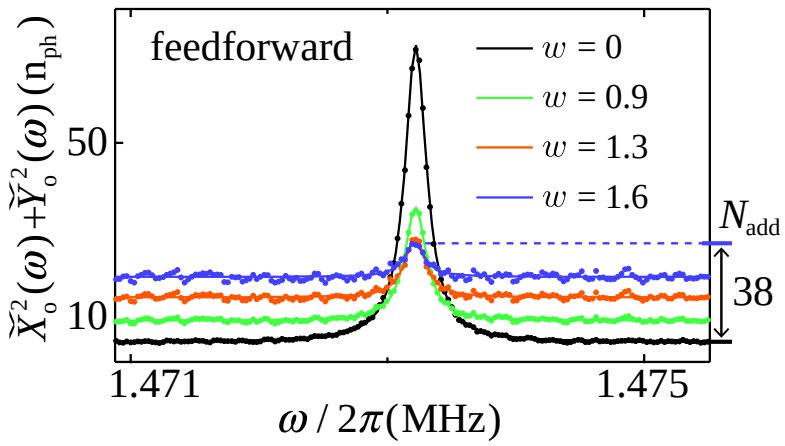

Figure 5.5: **Feedforward operation of a microwave-mechanical-optical converter.** Total noise power spectra, $\breve{X}_{\rm o}^2(\omega) + \breve{Y}_{\rm o}^2(\omega)$, for different feedforward weights, w, with $\Gamma_{\rm T} = 2\pi \times 200$ Hz. Best added noise in photons referred to converter input, $N_{\rm add}$, indicated on right axis.

from the optical measurement noise and fed-forward noise from the microwave measurement chain; for $w > 1$ the noise introduced by feedforward will dominate off-resonance while the thermal noise around f_m continues to decrease.

5.4 Feedforward theory

The feedforward framework is developed further in order to explore the potential and limitations of the technique.

5.4.1 Feedforward eliminates thermal noise

After passing through a sideband-resolved and impedance-matched converter, the signal and ancilla states are described by the quadratures

$$q_{\rm s,out} = \sqrt{\eta} q_{\rm s,in} + \sqrt{1-\eta} V_1 + q_{\rm th,out}, \tag{5.15}$$

$$q_{\rm a,out} = \sqrt{\eta} q_{\rm a,in} + \sqrt{1-\eta} V_2 + q_{\rm th,out}, \tag{5.16}$$

where $q_{\rm s,in}$ and $q_{\rm a,in}$ are the input signal and ancilla quadratures, V_1 and V_2 are vacuum noise introduced by imperfect conversion, and $q_{\rm th,out}$ is the thermal noise in the output spectrum. It

has been assumed that the pumps are configured to give identical thermal noise on microwave and optical outputs. For vacuum signal and ancilla, the quadratures in Eqs. (5.15-5.16) give a correlation matrix of the appropriate form, as discussed in Section 5.2. Assuming noiseless single-quadrature measurement and perfect converter efficiency, one can construct the fed-forward quadrature $\check{q}_{\mathrm{s}} = q_{\mathrm{s}} - wq_{\mathrm{a}}$. Choosing $w = 1$ yields

$$\check{q}_{\mathrm{s}} = q_{\mathrm{s,q}} - q_{\mathrm{a,q}}, \tag{5.17}$$

so thermal noise can be completely eliminated using feedforward. With a non-ideal measurement or converter, some additional noise will be fed forward along with the quantum noise of the ancilla; $w = 1$ will not in general be the optimal value for cancelling the thermal noise.

In the more realistic case of imperfect sideband resolution and imperfect cavities, gain and loss terms are introduced which cause an impedance mismatch. Due to the mismatch, some signal is reflected at peak efficiency. Reflected signals are inevitably fed forward along with the correlated noise, and feedforward is therefore degraded. Reflections can be reduced by operating away from peak efficiency, but this also degrades feedforward. Interestingly, an adaptive control strategy that avoids the matching requirement has recently been proposed [103]. The compatibility of this technique with feedforward, and other considerations for optimally handling imperfect sideband resolution, are interesting problems for future investigation.

Because our device is well matched, signal reflections are small for the feedforward experiment, and feedforward performance is overwhelmingly limited by measurement efficiency. Equations (5.15-5.16) therefore represent a useful limit for understanding the experiment and its main limitations. A full treatment should include explicitly the effects of gain and loss, and thoroughly explore the trade-offs for optimizing feedforward, which remains an open problem. It should be emphasized that the experimental characterization of feedforward performance does not require any assumptions about sideband resolution: we explicitly measure the variance of the fed-forward optical quadrature and observe that it is reduced.

5.4.2 Gaussian states

For a gaussian signal and ancilla, one need only keep track of quadrature variances. For the ideal case introduced above, the variance of the fed-forward quadrature is

$$\langle \check{q}_{\mathrm{s}}^2 \rangle = \langle q_{\mathrm{s,q}}^2 \rangle + \langle q_{\mathrm{a,q}}^2 \rangle. \tag{5.18}$$

When the ancilla is simply vacuum, feedforward adds vacuum noise, while removing all thermal noise. Our experimental efforts have only used vacuum ancilla and therefore are all referred to as classical feedforward. If a squeezed ancilla is chosen, then in the limit of perfect squeezing where $\langle q_{\mathrm{a,q}}^2 \rangle = 0$, the squeezed quadrature can be fed forward noiselessly. This enables upconversion of a squeezed state or noiseless measurement of a remotely prepared microwave quadrature.

The squeezed protocol requires a threshold converter efficiency to be reached. For a finite conversion efficiency, but with an otherwise perfect homodyne measurement apparatus, the fed-forward variance is

$$\langle \check{q}_{\mathrm{s}}^2 \rangle = \eta \langle q_{\mathrm{s,in}}^2 \rangle + \eta \langle q_{\mathrm{a,in}}^2 \rangle + 2(1-\eta)\langle V^2 \rangle, \tag{5.19}$$

where $q_{\mathrm{s,in}}$ is the input signal quadrature and $q_{\mathrm{a,in}}$ is the input ancilla quadrature, and $\langle V^2 \rangle$ denotes the vacuum variance. In the limit of perfect ancilla squeezing, $\langle q_{\mathrm{a,in}}^2 \rangle = 0$, less than one vacuum of noise is only added when $\eta > 1/2$. This is a threshold for measuring squeezing in an upconverted signal, or more generally measuring a remotely prepared microwave state with added noise less than 1/2 photon, referred to as a quantum threshold.

If one considers separate efficiency thresholds for microwave-optical and optical-microwave conversion and operates in a regime where thermal noise is added asymmetrically, it is possible to relax the threshold $\eta = 1/2$. If much less noise is added to one output port than the other, performance is improved when the low-noise output is used for the signal, so a lower efficiency can be tolerated in that direction. However, if the high-noise output is used for the signal, a higher efficiency is required. Strictly, $\eta = 1/2$ is therefore the minimum threshold for bi-directional conversion of squeezed states.

5.4.3 Qubit up-conversion

With a squeezed ancilla, the feedforward protocol can be used to remove noise in one quadrature. The task then is to encode a qubit in a single quadrature, and to find an encoding that makes this qubit robust to noise in that same quadrature. Here we examine one encoding to demonstrate that upconversion of a quantum signal in the low-cooperativity limit is possible in principle, without regard to technical feasibility. While our encoding has the virtue of formal simplicity, it is unlikely to be optimal with regard to efficiency requirements. We speculate that a Gottesman-Kitaev-Preskill qubit encoding may improve efficiency thresholds for qubit conversion as it would be robust to displacements in both quadratures [104, 105].

Consider using a squeezed ancilla to eliminate classical noise in the Y quadrature, leaving classical noise in the X quadrature. The noise operator $\mathcal{N}$ is of the form

$$\mathcal{N}(\rho) = \int U_\beta \rho U_\beta^\dagger p(\beta) \mathrm{d}\beta, \tag{5.20}$$

where ρ is the density operator of the qubit, $U_\beta|x\rangle \to |x+\beta\rangle$, and

$$p(\beta) = \frac{1}{\sqrt{2\pi}\sigma_X} e^{-\beta^2/(2\sigma_X^2)}. \tag{5.21}$$

Our goal is to show that, with a suitable decoder, this channel can transmit a qubit. This is equivalent to showing the channel can transmit a half of a maximally entangled state with high fidelity. It is formally simplest to demonstrate the required fidelity for an encoding expressed in terms of X eigenstates, $X|x\rangle = x|x\rangle$, but similar encodings for coherent states should work as well.

A decoder should preserve the quantum state, but should allow for information to be gained about β so that the state can be shifted back into its original space. What we want now is a pair of logical states $|\bar{0}\rangle$ and $|\bar{1}\rangle$ and a decoding operation $\mathcal{D} : H \to A$, where H is the output space of $\mathcal{N}$ and A is a single-qubit space (spanned by $|\bar{0}\rangle$ and $|\bar{1}\rangle$), such that the entanglement fidelity

$$F_{\text{ent}} = \langle\phi_0| I \otimes (\mathcal{D} \circ \mathcal{N})(|\phi_0\rangle\langle\phi_0|) |\phi_0\rangle \approx 1, \tag{5.22}$$

where $|\phi_0\rangle = \frac{1}{\sqrt{2}}(|00\rangle + |11\rangle)$. This fidelity can be rewritten as

$$F_{\text{ent}} = \frac{1}{4}\sum_{s=0}^{1}\sum_{t=0}^{1} \langle \bar{s}| \mathcal{D} \circ \mathcal{N}(|\bar{s}\rangle \langle \bar{t}|) |\bar{t}\rangle \,, \tag{5.23}$$

which will make it easier to calculate.

The encoding we will choose depends on an X eigenvalue $b > 0$, and is of the form

$$|\bar{0}\rangle = |b\rangle \tag{5.24}$$

$$|\bar{1}\rangle = |-b\rangle \,. \tag{5.25}$$

Noise of the form Eq. (5.20) will shift this codespace to a new space spanned by $|b+\beta\rangle$ and $|-b+\beta\rangle$. Choosing $b \gg \sigma_X$ will enable us to figure out the displacement β and shift the codespace back.

An excellent observable to measure to determine the value of β is

$$A_b = \int_{-b}^{b} \gamma P_\gamma \mathrm{d}\gamma. \tag{5.26}$$

Here, $P_\gamma = |b+\gamma\rangle\langle b+\gamma| + |-b+\gamma\rangle\langle -b+\gamma|$ is the projector onto the codespace after being displaced by γ in the x direction. Given outcome γ (which we will show below will almost surely equal the true shift β), our decoding will be completed by applying a conditional displacement U_γ to map P_γ back to the original codespace P_0.

It is useful to re-express A_b in terms of the X operator as follows:

$$\begin{aligned}
A_b &= \int_{-b}^{b} \gamma P_\gamma \mathrm{d}\gamma && (5.27)\\
&= \int_{-b}^{b} \gamma \left(|b+\gamma\rangle\langle b+\gamma| + |-b+\gamma\rangle\langle -b+\gamma|\right) \mathrm{d}\gamma && (5.28)\\
&= \int_{-b}^{b} \gamma |b+\gamma\rangle\langle b+\gamma| \mathrm{d}\gamma + \int_{-\mathrm{b}}^{\mathrm{b}} \gamma |-\mathrm{b}+\gamma\rangle\langle -\mathrm{b}+\gamma| \mathrm{d}\gamma && (5.29)\\
&= \int_{0}^{2b} (x-b)|x\rangle\langle x| \mathrm{dx} + \int_{-2\mathrm{b}}^{0} (\mathrm{x}+\mathrm{b})|\mathrm{x}\rangle\langle \mathrm{x}| \mathrm{dx} && (5.30)\\
&= \int_{-2b}^{2b} f_b(x)|x\rangle\langle x| \mathrm{dx} && (5.31)\\
&= \int_{-\infty}^{\infty} f_b(x)|x\rangle\langle x| \mathrm{dx} && (5.32)\\
&= f_b(X), && (5.33)
\end{aligned}$$

where

$$f_b(x) = \begin{cases} x - b \text{ for } 2b \geq x \geq 0 \\ x + b \text{ for } 0 \geq x \geq -2b \\ 0 \text{ for } |x| > 2b. \end{cases} \tag{5.34}$$

The function $f_b(x)$ is plotted in Figure 5.6.

To derive a result for the entanglement fidelity we would like to evaluate Eq. (5.23). The following calculation will be useful: fixing $|\bar{s}\rangle$ and requiring $|\beta| < b$ and $|\gamma| < b$, we have

$$\langle \bar{s}| U_\gamma^\dagger P_\gamma U_\beta |\bar{s}\rangle = \langle \bar{s}| \left(|b\rangle \langle b+\gamma| + |-b\rangle \langle -b+\gamma| \right) U_\beta |\bar{s}\rangle \tag{5.35}$$

$$= \langle (-1)^s b| \left(|b\rangle \langle b+\gamma| + |-b\rangle \langle -b+\gamma| \right) |\beta + (-1)^s b\rangle \tag{5.36}$$

$$= \langle (-1)^s b + \gamma | \beta + (-1)^s b\rangle \tag{5.37}$$

$$= \langle \gamma | \beta \rangle . \tag{5.38}$$

Our decoder $\mathcal{D}$ is implemented by a two-step process. The first step is the quantum nondemolition measurement of $A_b = f_b(X)$ which results in an estimate γ of the noise β that was applied. The second step is a translation $U_\gamma^\dagger$ to map back to the original codespace. We now evaluate the fidelity achieved by this decoding. To evaluate Eq.(5.23), we first fix $|\bar{s}\rangle$ and $|\bar{t}\rangle$,and compute

$$\langle \bar{s}| \mathcal{D} \circ \mathcal{N}(|\bar{s}\rangle \langle \bar{t}|) |\bar{t}\rangle \geq \int_{|\beta|<b} \int_{|\gamma|<b} \langle \bar{s}| U_\gamma^\dagger P_\gamma U_\beta |\bar{s}\rangle \langle \bar{t}| U_\beta^\dagger P_\gamma U_\gamma |\bar{t}\rangle \, p(\beta) \mathrm{d}\gamma \mathrm{d}\beta \tag{5.39}$$

$$= \int_{|\beta|<b} \int_{|\gamma|<b} \langle \gamma|\beta\rangle \langle \beta|\gamma\rangle \, p(\beta) \mathrm{d}\gamma \mathrm{d}\beta \tag{5.40}$$

$$= \int_{|\beta|<b} p(\beta) \mathrm{d}\beta \tag{5.41}$$

$$= \int_{|\beta|<b} \frac{1}{\sqrt{2\pi}} \exp\left(-\frac{\beta^2}{2\sigma_X^2} \right) \mathrm{d}\beta \tag{5.42}$$

$$= 1 - \mathbf{erfc}\left(\frac{b}{\sigma_X} \right) \tag{5.43}$$

$$= 1 - O\left(\exp\left(-\frac{\beta^2}{2\sigma_X^2} \right) \right). \tag{5.44}$$

Averaging over $\bar{s}$ and $\bar{t}$ gives us the result

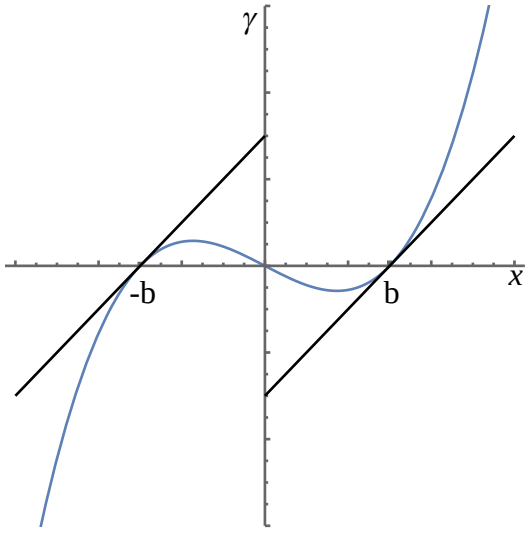

Figure 5.6: **Quantum feedforward observable.** Plot of measurement outcome for ideal observable $f_b(x)$ (black) and approximated observable $\tilde{f}_b(x)$ (blue).

$$F_{\text{ent}} \geq 1 - O(\exp(-b^2/(2\sigma_X^2))), \tag{5.45}$$

which will be close to 1, for $b \gg \sigma_X$. In other words, if the displacement b far exceeds thermal noise, errors can be diagnosed and corrected with an appropriately chosen decoding operation.

A key step in the decoding procedure described above is the QND measurement of $f_b(X)$, but implementing this measurement could be a challenge. We therefore consider a more physical decoding procedure, and argue that it will give similar fidelity to the one described above. In particular, we let

$$\tilde{f}_b(x) = \frac{1}{2b^2}x^3 - \frac{1}{2}x. \tag{5.46}$$

This is a good approximation to f_b near $\pm b$ (see Figure 5.6): for $|\gamma| \ll b$ we have $\tilde{f}_b(\pm b + \gamma) = \gamma$, which is exactly what we require. Because of our choice $b \gg \sigma_X$, we are very likely to get a measurement outcome in this range if we measure $\tilde{f}_b(X)$, so doing so is a good proxy for measuring $f_b(X)$.

Our decoding procedure is again two-step: First, do a QND measurement of

$$\tilde{A}_b = \frac{1}{2b^2} X^3 - \frac{1}{2} X, \tag{5.47}$$

obtaining a result γ. Second, apply $U_\gamma^\dagger$. This gives a transmitted fidelity close to 1 as long as $b \gg \sigma_X$.

Chapter 6

Converter Limitations

This chapter discusses the limitations of the transducer in order to highlight why quantum operation has eluded us. First, Section 6.1 lays out a detailed study of the sources of added noise. Next, Section 6.2 delineates the challenges of making a flip-chip with a reliable, reproducible gap separation. Section 6.3 contains a brief discussion of some of the consequences of the compromises made in building the optical cavity around a microwave enabled chip to motivate the improvements discussed in Chapter 7.

6.1 Conversion pumps lead to added noise

Although feedforward and laser cooling achieve comparable noise performance in the current setup, their limitations are quite different. In the presence of technical noise that limits damping rates, the performance of laser cooling at a given pump power is set by $n_{\mathrm{th,m}}\gamma_{\mathrm{m}}$, where $n_{\mathrm{th,m}}$ is the thermal phonon occupancy of the membrane. In feedforward, the main limitation is noise from the measurement chain, which is indistinguishable from the deviations being corrected for. For the quantum feedforward protocol, we considered the case with perfect measurement efficiency more broadly however, the product of both measurement efficiencies and converter efficiency needs to be above 50%. Our work has not focused on improving the measurement chains and therefore the focus of this chapter will be on the limitations of the more standard laser cooling method. Although many of the technical limitations for laser cooling are not the limiting factor for feedforward, addressing them would still help the feedforward method.

noise source	noise photons	
	high efficiency	high Q_{m}
parameter noise	23	1
generator phase noise	2	0
thermal motion	7	11
laser heating	2	1
total	34	13

Table 6.1: **Added noise budget for each contributing source**. The high efficiency device reached $\eta = 47\%$ and was the focus of Chapter 4. The Q_m device reached lower added noise but had lower efficiency. Noise budgets are shown for the best laser cooled added noise configuration in each device. That is, the point where the pumps are turned up as high as possible before technical noise dominates.

In the low conversion rate regime, the transducer is dominated by thermal noise from the mechanical oscillator. As the conversion rate is turned up, the contribution from thermal motion is reduced, but the pumps also introduce potential noise sources. These are referred to as technical noise sources because, unlike the thermal motion, they are not inherent to the device but rather arise due to the non-ideal behaviour from the pumps needed to operate the device. The technical noise sources include: classical phase noise from our microwave source, laser heating of the LC circuit, and parameter noise in our LC circuit due to the high microwave pump power. In the absence of technical sources of added noise, the pump powers could be increased until the conversion rate dominates over the fixed thermal decoherence rate to overcome the thermal added noise. The pumps can introduce noise simply by being spectrally dirty or through more complicated processes that induce fluctuations in the device. Table 6.1 shows a budget of the noise figure quoted in Chapter 4. The total noise figure is categorized in order that solutions can address the independently.

The optomechanical cooperativity compares the conversion rate to the intrinsic mechanical damping rate and is useful in understanding the sources of added noise as it highlights the high pump powers needed (Eq. 6.1). The criterion of low mechanical added noise is analogous to the more common optomechanics goal of ground state cooling. Ground state cooling is when the mechanical oscillator is damped by the pumps until it spends the majority of its time in the ground state. If a mechanical oscillator is in the ground state then information can be transmitted through it

without the environment adding photons to the signal. Therefore the limit of no added mechanical noise is the limit of spending 100% of the time in the ground state. This is also equivalent to the high cooperativity regime: the optomechanical damping rate being much higher than the intrinsic dissipation,

$$\frac{\Gamma}{n_{\mathrm{th}}} > \gamma_{\mathrm{m}}. \tag{6.1}$$

Here we express

$$\Gamma = \frac{4g_0^2 n_{\mathrm{cav}}}{\kappa_{\mathrm{T}}} \tag{6.2}$$

to highlight technical values needed, where n_{cav} is the number of photons in the cavity. Due to the low frequency of our mode, the thermal occupation is fairly large even at millikelvin temperatures. The mechanical excitations are bosonic and therefore follow Bose-Einstein statistics

$$n_{th}(\omega = 2\pi \times 1.5 \text{ MHz}, T = 100 \text{ mK}) = \frac{1}{e^{\hbar\omega/k_{\mathrm{B}}T} - 1} \approx 1400. \tag{6.3}$$

Combined with the modest quality factors we achieve thus far ($\gamma_m = 11 \times 2\pi$ Hz for the high efficiency device), it takes a high damping rate of $\Gamma \sim 15 \times 2\pi$ kHz to reach this regime. Feasibly we can reach the cooperativity requirement, but it is achieved with very high pump powers that cause technical added noise. The single photon-phonon coupling rate is very small for our device, (see table 4.1) which means very a high number of photons in the resonator ($n_{\mathrm{cav}} \sim 10^8$) are needed to reach the high cooperativity regime. Ideally this would not be a problem, and indeed for matched conversion the highest damping rate achieved was $\Gamma_{\mathrm{T}} = 100 \times 2\pi$ kHz. However, experimentally we find that the high pump powers introduce technical noise sources that are converted along with the signal that lead to higher added noise and preclude ground state cooling.

One example of technical noise is phase noise from the microwave pump. This source of noise is essentially a dynamic range problem. In which which the pump power needed is weighed against the excitation of a single photon. Because 10^8 photons in the resonator are needed for high cooperativity and the pump is off resonance, this means the pump tone needs 10^{16} photons

incident, or $P_{\text{in}} = -42$ dBm. For a detuned pump, the number of photons in the cavity is given by

$$n_{\text{cav}} = \frac{P_{\text{in}}}{\hbar\omega} \frac{\kappa_{\text{ext}}}{\Delta^2/4 + \kappa_{\text{T}}^2}. \tag{6.4}$$

The power from a single photon in a 1 Hz bandwidth, P/BW, can be obtained for using Bose-Einstein statistics,

$$n_{MW} = \frac{1}{e^{\hbar\omega/(P/BW)} - 1}. \tag{6.5}$$

Solving for the power in a 1 Hz bandwidth gives -204 dBm This corresponds to a difference of 162 dB between the power in pump tone and the PSD that can tolerated detuned by the mechanical frequency of 162 dB. This kind of dynamic range is difficult to achieve in microwave generators. The phase noise measured for the generator we use (Agilent PSG E8257D) at 1.5 MHz is -144 dBc/Hz. This means that for a given pump power, if a PSD is measured 1.5 MHz from the tone, there will be a noise floor 144 dB below the peak pump power. The noise will be converted along with the signal and would look like added noise in the converter. The best added noise performance in Table 6.1 was achieved with pump powers of -57 dBm incident on the cavity. This means that there is -201 dBm of noise 1.5 MHz from the carrier, which is equivalent to 2 photons of noise at 6 GHz.

Options for reducing generator phase noise are either buying a lower-noise microwave source or filtering the pump. Commercially available generators cannot offer much greater dynamic range than ours. There are optically generated microwave signals that can offer the dynamic range required, but are limited in power [106]. If we were to use the powers needed for high cooperativity with our current generator we would need nearly 20 dB of filtering. For narrow filter windows very close to the pump this requires high Q filter cavities. This possible but as the phase noise is not our main limiting factor it has only lightly been pursued. Increasing the electromechanical coupling would also relax this constraint by reducing the microwave power needed.

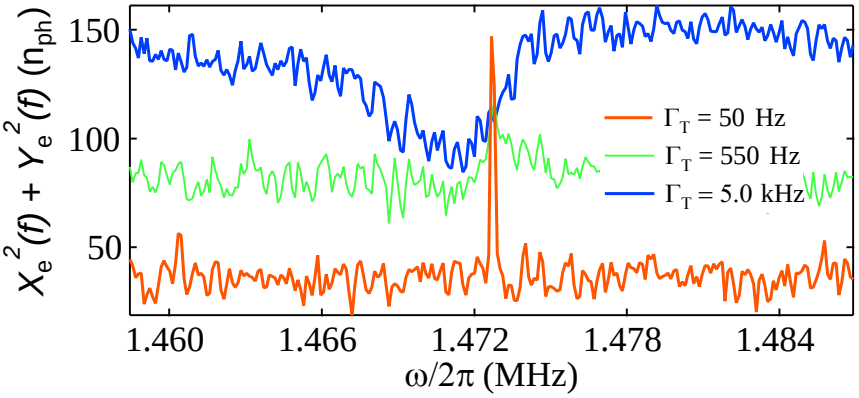

Figure 6.1: **Microwave noise squashing.** Noise measured at the microwave converter output. As power is increased, the mechanical peak is damped and the background noise increases. At the highest power, the mechanical peak becomes a dip in the background noise.

6.1.1 Microwave circuit parameter noise

Most of the conversion added noise plots shown so far show the noise emitted at the optical port. For the converter used in our high efficiency device, we can also look at the noise coming out the microwave port. The spectrum at the optical port looks distinctly different than the spectrum at the microwave port. The optical port shows the mechanical mode with a flat background as seen in Figure 4.9. In contrast, the microwave port shows the mechanical mode on a background that is dependent on microwave power. Spectra at the microwave port for increasing pump power are shown in Figure 6.1. In the microwave output spectrum the background increases, but looking at the optical spectrum the noise only increases in the converter bandwidth, which is evidence that the noise is present in the LC circuit. This background noise is due to an unanticipated source of fluctuations in the LC circuit. Under the strong microwave pump required for operating in the high cooperativity regime, the circuit's resonance frequency and quality factor both fluctuate with substantial frequency components around 1 MHz. Such fluctuations are essentially indistinguishable from fluctuations in the oscillator's position.

Fluctuations in the LC circuit parameters convert pump photons to power at the mechanical oscillators resonance frequency, therefore adding noise to the conversion process. At high pump

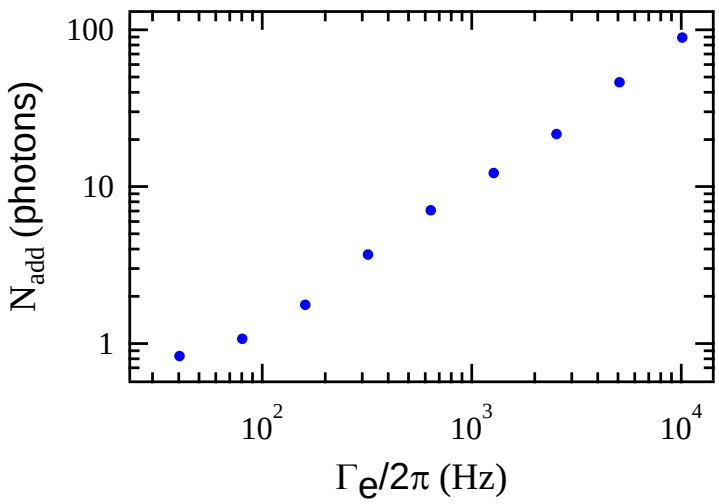

Figure 6.2: **Added noise from parameter noise.** The noise coming out the microwave port as the electromechanical damping rate is increased shown in units of conversion added noise.

powers, it looks as if the parameters of the LC circuit, either the Q or the frequency, are fluctuating in time, and we therefore refer to this noise as parameter noise. This can be understood by considering the pump from the frame of reference of the LC. From the fixed LC frame of reference it looks as if the pump power and frequency is fluctuating in time, and therefore this noise hurts us in exactly the same way as classical noise on the pump. The excess noise in the microwave circuit is correlated to an increase in loss, which is explored in more detail in 7.2. The noise budget for LC parameter noise was studied by monitoring the noise coming out the microwave port as the pump power was increased. Figure 6.2 shows the added noise vs damping rate. (Note, by referring to converter input we are referencing the noise at the microwave port, which conveniently is the same reference place made if we measure microwave noise and calibrate out the measurement chain. Therefore, the same calibration allows us to quote the excess noise in terms of added noise photons for a conversion process.)

Further evidence that the noise originates in the LC circuit can be seen from looking at a wider spectrum showing that the noise is filtered by the susceptibility of the LC circuit. The added noise shows up in the microwave spectrum as an excess of power around the LC frequency as shown

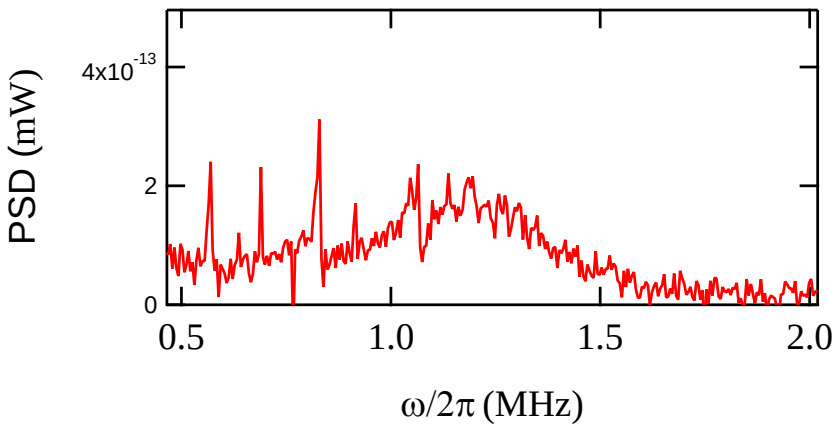

Figure 6.3: **Broadband parameter noise.** Noise measured for high pump power showing noise is originating in LC. This measurement was made on a device with 500 kHz linewidth. The LC shape shows up above the background noise floor. Sharp features are mechanical modes and electronic noise.

in Figure 6.3. The noise has the characteristic width of the LC circuit indicating that the noise is either originating in the LC, or is at least filtered by it, which eliminates sources of noise on the pump before the LC. Another way to tell that the noise is in the LC circuit is from looking at the spectrum around the mechanical frequency at the microwave port as a function of damping power. Unlike in measuring the noise in the optical domain, the noise increases off mechanical resonance with increasing pump power. As the power is increased, first the mode is broadened and the peak is reduced as in normal operation, but at higher powers noise squashing is observed. Noise squashing is interference between noise in the LC circuit coupling directly to the transmission line and coupling first to the mechanical oscillator and then to the transmission line [55, 107, 108, 109]. The noise is present in the LC circuit, so in the optical spectrum, the background remains constant with increasing power, while the transduced noise filtered by the mechanical susceptibility increases.

6.1.2 Microwave circuit noise induced by laser light

Perhaps the easiest source of noise to predict is laser heating of the LC circuit. Most superconducting experiments go to great lengths to isolate there quantum circuits from higher frequency

photons. They are placed inside a dilution refrigerator in light tight boxes and even the filtering on the cabling is an open area of research to reduce noise [110, 111, 112]. In our experiment we have done the complete opposite: we have a window out to room temperature as well as a bright laser shining less than a half millimeter away from the superconducting circuit. Therefore it is perhaps not surprising that turning on the laser adds some amount of noise in the LC circuit that is then upconverted along with the signal. The size of this effect, however, is determined empirically. There were concerns that this would make our approach impossible, and it was not until we cooled a converter device down in a dilution refrigerator and studied the noise that we understood the amount of noise that we would need to contend with.

The laser heating is one of the lower contributors of added noise (Table 6.1). This is reassuring in the sense that it is not orders of magnitude away from what is needed for quantum operation. The contribution from laser heating is measured by shining light into the optical cavity and measuring the PSD coming out the microwave port. This is similar to the conversion data except it is done without the microwave pump on, which allows the noise figure to be extracted independent of all other sources (thermal motion, generator phase noise, and parameter noise). Optical photons heating the superconductor convert optical photons to microwave photons, but in a noisy incoherent way that is detrimental to the conversion process.

Figure 6.4 shows the effect of the laser light on the microwave cavity linewidth and the noise coming out the microwave port. This is taken with the optical cavity configured in the high-stability regime used for efficiency measurements (Table 4.1). The LC linewidth increases by about 10% as the optical damping rate is increased. On the graph, both the noise and linewidth have two points that correspond to zero damping. The first point is the LC parameters with all lasers blocked, while the second, higher point is with the lock beam incident on cavity resonance, but with zero damping power. The initial increase from the lock is worrisome because it is already at a low lock power operating point of 500 nW. After the initial jump the added noise increases gradually. This is not understood, but is reassuring in that if the baseline can be lowered then the laser heating may not be the limiting factor, even at high pump powers. In this device we

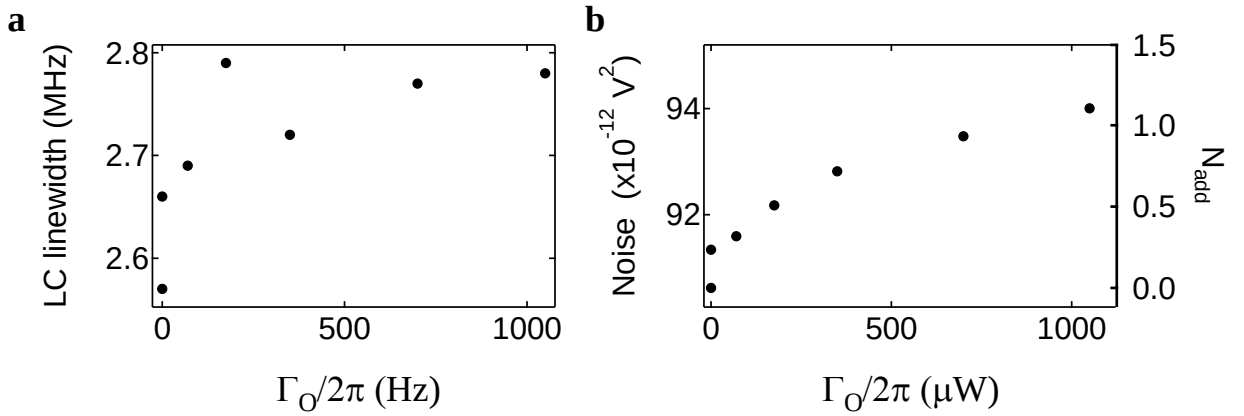

Figure 6.4: **Laser Heating of LC. a,** Laser light increases loss in the microwave circuit. There are two points at zero damp power. The lower one corresponds to no lasers, while the higher one is with the cavity locked with 500 nW. **b,** Noise increase for given damping rate. The left axis shows uncalibrated microwave noise while the right axis is in added photons.

were not able to lock at high optical damping rates but, this problem has been fixed by modifying room temperature electronics which has also allowed us to operate at lower lock powers. Moving to a higher optomechanical coupling rate should also lower this curve as less optical power will be needed for the same damping rate.

The laser heating has not been extensively explored. There is a bottle neck in acquiring more data as full devices with microwave and optical capabilities are difficult and time consuming to make. In the experiment, we can adjust the membrane's location within the optical standing wave. This changes the internal and external coupling rate but when normalized to photons lost the noise is relatively constant. Reducing the loss of the cavity should allow for a more strongly overcoupled cavity and fewer photons lost inside, minimizing the chance of depositing energy into the superconductor. The path a stray photon takes could be absorption in the silicon nitride that then leads to high energy phonons hitting the superconductor, the silicon nitride acting as a waveguide for scattered photons, or maybe multiple reflections leading to the superconducting pad. In future tests we plan to put a metal wall on the membrane meant to differentiate between energy pathways in the membrane and scattered photons.

6.2 Capacitor gap spacing is unreliable

One of the largest challenges of this experiment that I spent considerable effort grappling with is reliably achieving small capacitor gap sizes for high mechanical coupling rates. The chips are order cm in size and the intended gap separation is 100 nm, a five order-of-magnitude difference. That is equivalent to holding a kilometer long stick by the ends and trying to accurately control the separation near the middle of it down to the cm level. This analogy shows just how many things need to be accounted for to get this small gap. There can't be anything higher than a centimeter over that whole kilometer, things like the bow over that distance will matter, and upon cooling down the different coefficients of thermal expansion cause stress or strain on the chips and can distort the separation. Our flip-chip devices are fabricated with this in mind. In order to limit the chances of dust getting between the chips and defining a larger gap, there are 15 μm trenches cut out of the chips everywhere except for the posts that define the separation and capacitor plate as seen in Figure 3.1. This reduces the chance that any dust on the chip will be in a region that would dictate the separation.

This strategy allowed us to achieve a gap separation of a few hundred nanometers at room temperature. The first devices cooled down all had high resonant frequencies corresponding to large gap separations. A white light interferometer revealed that the separation matched the design at room temperature indicating that the separation was increasing upon cooling down. In order to verify that the SiN was not causing an error in the interferometer measurements, the most accurate method was to break the membrane and measure the height difference between the shards of SiN remaining on the membrane frame and the bottom capacitor.

6.2.1 Stycast affects capacitor gap spacing

Mismatches in the coefficients of thermal expansion cause the epoxy to strain the chips and change the capacitor gap separation. Even though the separation is set by a thin layer of aluminum, the posts are actually 30 um tall (because of the trenched away areas), which means

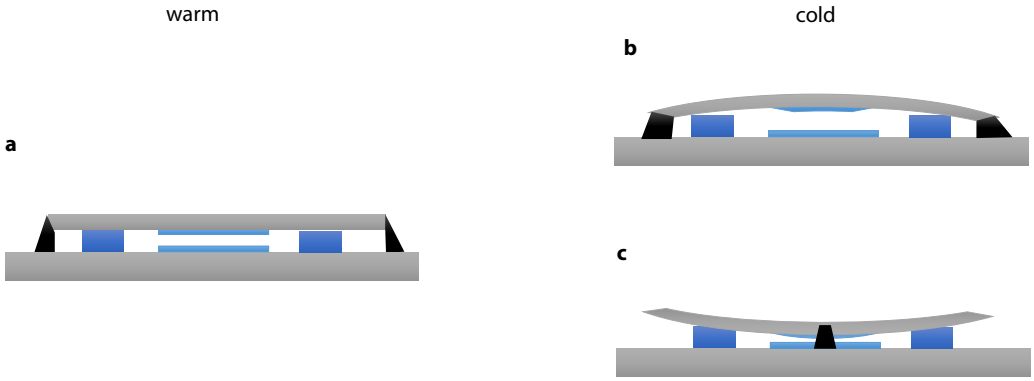

Figure 6.5: **Thermal contraction bows chip. a,** Profile view of assembled flip chip. At room temperature the chips are well aligned and have a capacitor gap spacing set by the chips posts. Grey is silicon top and bottom chip. Blue is posts defining separation and capacitor pads. Black is epoxy. **b,** In the corner epoxy design, when the epoxy contracts relative to the posts, the chip bows and the middle is bowed up, increasing the capacitor gap. **c,** Epoxying on the edge of the top chip pulls the capacitor pads closer together as the epoxy bows the chips. Epoxy on edge looks like it is between the post when viewed in profile. See Figure 6.6 for top layout.

that the stycast drops span that same height. The thermal contraction of silicon is a few parts per million while stycast which is an order of magnitude higher. This means that the epoxy shrinks on the order of a few hundred nanometers more than the post. The geometry of the posts causes the stycast to pull the corners down, and the middle of the chip is levered up, increasing the capacitor separation. Figure 6.5 shows the a profile view of the chip flex affecting the capacitor separation, while Figure 6.6 shows a finite element simulation of the silicon chip flexing for a given amount of strain at the epoxy joint. Switching the epoxy from the corners to the edges changes from a lever flexing up, to pulling the middle down (Figure 6.6) which allowed for a solution to the problem with the existing chips. There are small posts right near the membrane and therefore the spacing should be set by forcing those together.

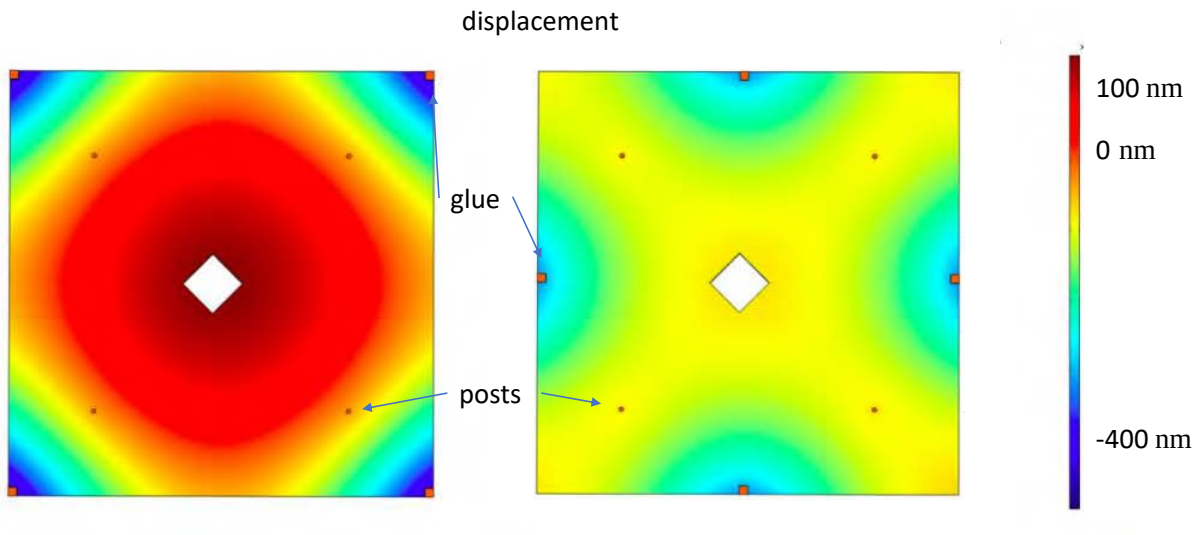

Figure 6.6: **Epoxy placement determines bow.** Finite element simulations of ship bowing due to stress at points of contact with epoxy. Epoxying on the corners levers the middle of the chip up, leading to increased capacitor gap separation. Epoxy on the edges pulls the middle of the chip down.

6.2.2 Chip frequency spread

The change of epoxy placement solved the high resonance problem, but the fact that our chips spacing was dependent on a relatively uncontrolled amount of epoxy meant that the spacing was still different from chip to chip and from cooldown to cooldown. In fact, the force from the chip flexing down was enough to squish the posts near the membrane in some devices, leading to lower resonance frequencies. We confirmed that the low frequencies were due to the posts deforming by breaking apart flip-chip devices after cooling down and measuring the height of the center post. In some devices it had reduced by up to 80 nm.

The uniqueness of each device leads to a range of LC frequencies across the 4-8 GHz band. The modular hats of the 3D cavity were designed to account for this spread, allowing us to chose a hat to match the chip frequency but the change from cooldown to cooldown could not be predicted or addressed. The 3D cavity coupling depends on the detuning between the LC and the 3D cavity resonance, as well as on the external coupling (see equation 3.1). A range of external couplings

work for our converter device, but there is an optimum for efficiency and added noise. The largest linewidths we could achieve for our 3D cavity were about 250 MHz, meaning that our device could change by about 50 MHz from the goal and we would still have a converter that had reasonable sideband resolution and external coupling. Our flip-chips changed by up to 500 MHz from cooldown to cooldown. Patience and multiple tries allowed this procedure to work well enough for a few experimental runs but was too tedious for long term viability. In addition, to help address technical noise sources we aim to reduce the design gap separation to increase the mechanical coupling rate, meaning fractionally we would be even more vulnerable to gap changes. Therefore the chips need higher reliability or the coupling method needs to be independent of the LC frequency. The 3D cavity allowed us to move to shorter cavities, so any solution that moved away from the 3D cavity needs to preserve the optical cavity length to avoid a step backwards in progress.

6.2.3 Deformation of top chip reduces Q_{m}

Strain in the top chip at the location of the membrane limits Q_{m}. There are two mechanisms by which the radiative loss could be changing. Deforming the chip down increases the contact between the top and bottom chip and could increase radiative loss. However, we observe deformation away from the bottom chip also lowers the Q_{m}, indicating that strain in the chip is the cause. If the central posts are clamped tightly down, then there is a more efficient link to the bottom chip right near the membrane and more mechanical loss is present. If this was the only effect then all chips above the design frequency should have high Q_{m} as well. The low Q_{m} of chips above the design frequency suggests that some amount of stress in the top chip from bending and flexing leads to more loss as well. In testing a range of devices we found a trend of lower Q_{m} the further the device resonance was from the design frequency. This was true for devices with frequencies above as well as below the design goal, as shown in Figure 6.7. Both points suggest a solution that more accurately hits the design frequency and reduces local strain near the membrane.

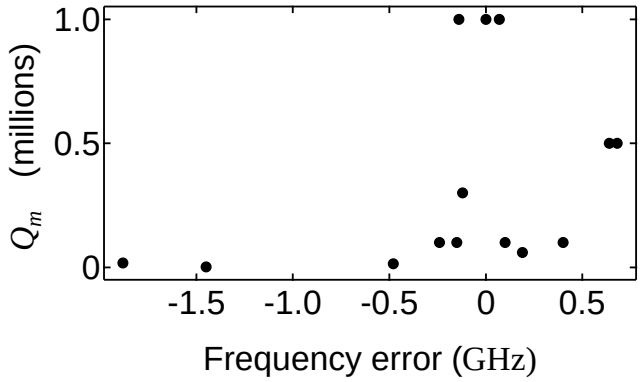

Figure 6.7: Q_m **is correlated to LC frequency.** Q_m for various devices is shown as a function of measured LC frequency compared to the design goal. The devices with the highest Q_m are the ones closest to the design frequency.

6.3 Loss in optical cavity limits efficiency

The limitation of the optical cavity geometry is discussed here to motivate the switch to an etalon cavity. The inability to make a strongly overcoupled cavity limits the over all conversion efficiency. The conversion efficiency scales as the microwave and optical coupling efficiencies

$$\eta \propto \frac{\kappa_{\mathrm{ext,o}}}{\kappa_\mathrm{o}} \frac{\kappa_{\mathrm{ext,e}}}{\kappa_\mathrm{e}}. \tag{6.6}$$

The limiting factor is set by the uncontrolled loss of the optical cavity. Our group has become very good at making strongly overcoupled cavities with membranes in the middle [90, 92]. However, the challenge of integrating the microwave components leads to higher internal loss and a lower coupling ratio. Even with microwave components, the optical cavities are overcoupled at room temperature, but upon cooling down the membrane and mirrors misalign relative to each other and lead to an increase in internal loss. For example, we can look at the cavity used for the high efficiency conversion described in Chapter 4, which had the highest optical efficiency yet for a converter device, but still shared the characteristic challenges of integrating all the components together. The empty cavity had an external coupling rate $\kappa_\mathrm{ext} = 1.1 \times 2\pi$ MHz and an internal coupling rate $\kappa_\mathrm{int} = 0.2 \times 2\pi$ MHz. Adding the membrane increased the internal loss rate to

$\kappa_{\text{int}} \approx 0.4 \times 2\pi$ MHz. The approximation symbol is used to highlight that once the membrane is in the cavity, the external coupling and the loss rate depend on the membrane spacing (see Figure 6.8), but for concreteness we quote values at the converter operating point. Cooling down increased the loss further to $\kappa_{\text{int}} \approx 1.0 \times 2\pi$ MHz, which leaves us with a marginally overcoupled cavity. The frequency of the mechanics and our desire to stay sideband resolved prohibit us from simply moving to a more strongly overcoupled cavity by increasing the external coupling.

The optical cavity parameters are partially adjustable cold by moving the mirrors. Both optical cavity mirrors can be translated longitudinally via piezoelectric actuators. During operations, one of these actuators is used for the locking scheme, and the other is used to change the membrane position within the optical standing wave of the cavity and then held stationary. The membrane and stationary mirror effectively constitute a low-finesse etalon whose transmission depends on their separation.

Figure 6.8 shows the theoretical and measured optical linewidth and the theoretical optomechanical coupling rate as a function of membrane-mirror separation. As the membrane position is varied, the light energy is stored predominately to one side or the other of the membrane [92], and the external coupling factors associated with the high-throughput input mirror and the low-throughput back mirror ($\kappa_{\text{ext,o}}$ and $\kappa_{\text{B,o}}$, respectively) vary accordingly. In order to further increase $\kappa_{\text{ext,o}}/\kappa_{\text{o}}$, the optical cavity mirrors have unequal transmission rates. This cavity asymmetry results in variation in the total optical cavity linewidth κ_{o} as the membrane position is varied. Furthermore, our membrane is placed closer to the input mirror, resulting in enhanced optomechanical coupling G_{o} when $\kappa_{\text{ext,o}}/\kappa_{\text{o}}$ is maximized. Ideally, we would operate at a position where G_{o} and $\kappa_{\text{ext,o}}$ are simultaneously maximized. However, due to optical instability, a configuration with $\eta_{\text{M}} = 0.43$ and $\kappa_{\text{ext,o}}/\kappa_{\text{o}} = 0.54$ was used instead for noise measurements.

Upon cooling down, misalignment leads to an increase in the internal loss across the membrane position as the light is scattered into higher order modes, but also leads to sharp deviations from the expected cavity linewidths as we sweep the membrane through the cavity (Figure 6.8). This is indicative of a misaligned membrane that is causing coupling to higher order lossy modes [113].

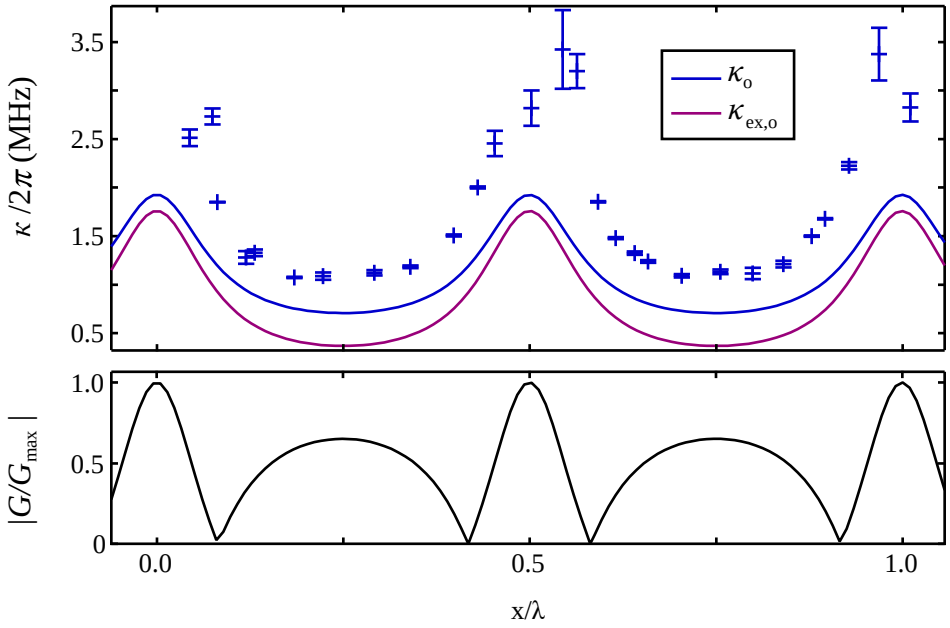

Figure 6.8: **Cavity couplings dependence on membrane position.** Upper plot: simulated (blue line) and measured (blue points) optical cavity linewidth, and simulated external coupling rate (purple line) as membrane distance from mirror, 750 μm + x, is varied. Difference between measured and expected is a result of increased loss. Error bars represent the standard deviation of several repeated linewidth measurements. Lower plot: absolute value of theoretical optomechanical coupling normalized to maximum coupling.

Although moving to the 3D microwave cavity allowed us to shorten the optical cavity and produce our first overcoupled optical cavity in a converter experiment, it still showed some characteristics of being misaligned. All of these things combined lead us to push for a more robust optical cavity design so that we can have higher overall efficiency, as well as work at higher mechanical coupling rates, and therefore need less optical power, which will help with laser heating of the superconductor.

Chapter 7

Technical Improvements to Reduce Added Noise

This chapter discusses the steps taken to address each limitation laid out in Chapter 6. The parameter space is interconnected and not all problems could be solved independently. Fabrication methods to improve Q_{m}, the capacitor gap separation, and microwave circuit parameter noise are discussed in sections 7.1 and 7.2. Fabrication techniques to improve the optical cavity and flip-chip assembly are introduced in Section 7.3. These improvements allow for a more robust LC coupling method to be used, which is described in Section 7.4. The chapter concludes in Section 7.5 with a projected noise budget for a new converter device that will test the range of improvements that I have worked on.

For completeness, here is a list of the problems and implemented solutions covered in this chapter

- Implementing suppression of acoustic radiation to reduce mechanical loss.
- Reducing capacitor gap separation for improved electromechanical coupling.
- Relieving silicon in top chip to improve capacitor gap accuracy.
- Changing superconductor to Niobium Titanium Nitride (NbTiN) to reduce LC parameter noise.
- Introducing etalons to improve optical cavity stability.
- Developing bonding methods for glueless etalons and flip-chips.

7.1 Fabrication methods to improve Q_{m} and reduce capacitor gap separation

7.1.1 Improved Q_{m}

We developed a method that improves the mechanical quality factor by an order of magnitude and allows us to reliably reach $Q_{\mathrm{m}} > 10^6$ in our flip-chip geometry. Reducing the mechanical coupling to the environment improves the added noise contribution from thermally driven motion. In our standard membrane designs Q_{m} was limited by radiation loss due to the variability in affixing the top and bottom chip as discussed in Section 6.2. The variability produced a range of quality factors, where almost all chips had $Q_{\mathrm{m}} > 10^5$, and occasionally some reached $Q_{\mathrm{m}} > 10^6$. While the quality factors achieved in our flip-chips are not too much worse than other simple membrane geometries, there is clearly room for improvement as evidenced by the multiple approaches that now use soft clamping [114] and phononic shielding [115] to achieve $Q_{\mathrm{m}} \geq 10^8$.

Incorporating a PNC structure into our flip-chips would be advantageous for several reasons. A PNC opens up a band gap around the frequency of the membrane mode and therefore reduces radiation loss as the substrate does not support those modes [116]. The elimination of thermally occupied substrate modes near the membrane mode of interest is also valuable in and of itself, beyond the enhancement of mechanical Q. In order to maximize the benefit of a PNC, it is desirable to have the only contacts from the membrane to the outside world be through the PNC. However, in order to avoid collapsing the capacitor when working with very small gap separations, we have always fabricated posts very near the membrane in our flip-chip devices. Whether a PNC would still improve Q_{m} in the presence of these posts is not clear, and the reliability of flip-chips with the points of contact outside multiple PNC unit cells has not been demonstrated.

We design a geometry that improves Q_{m} and tests fabrication techniques needed to incorporate phononic crystal (PNC) structures in our flip-chips. Because of these uncertainties, we decided to start with a simpler approach to improving Q_{m}: connecting the membrane to the top chip frame only through four narrow tethers (Fig. 7.1). Because the tether fabrication process is quite similar to the fabrication required for a PNC, the simple tether design also enabled us to test fabrica-

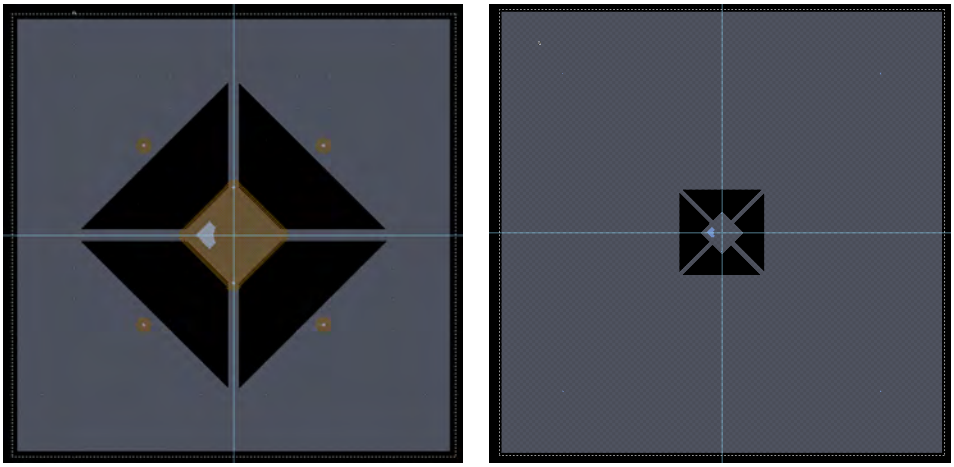

Figure 7.1: **Initial tether designs.** Different orientation of tethers to test whether Q_{m} depended on tether orientation along a nodal line of the mechanical mode. The two designs were tested on two different size chips. Two of four design configurations shown here. Light grey is Si, dark regions are holes that are etched away, light blue is capacitor pad, yellow shows areas that are not etched away for trenches (only shown on left design).

tion techniques needed to eventually incorporate PNC structures into our flip-chips. Tether/PNC fabrication challenges and our solutions are discussed further in section 7.1.3.

Figure 7.1 shows two designs for a top chip with cutouts for improving mechanical isolation. There are several distinct physical mechanisms through which these tethers might improve Q_{m}: by approximating a single-pole PNC, by making the silicon frame a less rigid boundary condition (i.e., approximating soft clamping), or simply by reducing strain from the bowing silicon chip. The two different designs were to test whether tethers along nodal or anti-nodal lines produced higher isolation, but initial tests were made for both designs and each showed reliable $Q_{\mathrm{m}} \sim 10^6$. This improvement reduces the contribution from thermal phonons by an order of magnitude.

7.1.2 Increasing electromechanical coupling through smaller gaps

We improve the electromechanical coupling rate by reducing the capacitor gap. The single phonon-photon coupling rate for the microwave circuit is

$$g_0 = \frac{w_0}{2d} C_{\mathrm{p}} x_{\mathrm{zp}}, \tag{7.1}$$

where $C_\mathrm{p} < 1$ is the participation ratio of the mechanically compliant capacitance to the total capacitance of the circuit, d is the capacitor gap separation, and w_0 is the LC resonant frequency. The zero-point motion was maximized for our membrane size by shaping the metal pad to have high spatial overlap with the mechanical mode of interest. The participation ratio is set by the geometry of the LC circuit can only be improved marginally from its present value $C_\mathrm{p} = 0.8$. Without changing the size or thickness of the membrane or in some other way changing the microwave circuit the most direct way to improve the electromechanical coupling is to reduce the gap size. Increasing the frequency of the microwave circuit would also increase g_0, and tradeoffs with other converter parameters are being explored to determine if this would result in a net improvement.

The mechanical coupling rate g_0 is doubled by reducing the capacitor gap by a factor of two from 300 nm in previous designs to 150 nm. However, flip chips with small gap separations are more susceptible to the capacitor collapsing. For comparison, aluminum drumhead devices collapse with gap separations below 40 nm [89], and they are usually an order of magnitude smaller in transverse dimension. A few test devices have been designed for 100 nm gap separation, but only one out of four tests led to a working device, suggesting that it is too ambitious a goal for reliably making a converter. A separation of 150 nm reduces the power needed to achieve a given electromechanical damping by a factor of 4 and reliably produces working devices.

Moving to smaller gap separations would not have been possible without solving the reliability issues, discussed in Section 6.2, that plagued devices designed for 300 nm gap spacings. These issues are addressed by engineering the top chip bulk substrate and the post geometry. The position of the posts and epoxy blobs affect how the strain due to thermal contraction is distributed over the chip, and thus how the capacitor gap changes. These positions can be adjusted to minimize strain near the membrane. An alternative and complementary approach to reducing strain near the membrane is to make the top chip more compliant. One way to do this is to make the chip larger, which provides a longer lever arm to take up the strain at the epoxy blob, and thus reduces the local curvature. This is difficult because larger chips means that the intrinsic bow of the wafer starts to matter and the area needed to keep clean increases. Alternatively, the silicon structure

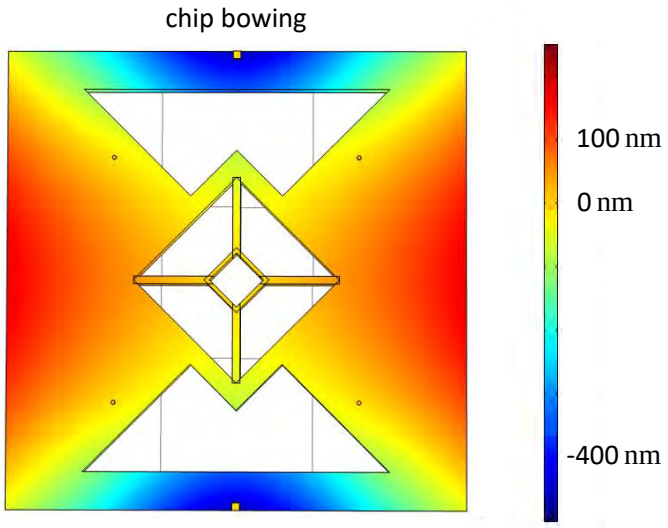

Figure 7.2: **Relieved silicon structure accommodates shrinking epoxy.** Simulation of chip bowing due to epoxy shrinking. Cutouts allow silicon to locally deform around the epoxy blobs (on the top and bottom edges) without transferring strain to middle of the chip. The post spacing has also been adjusted to null out motion at center of chip.

itself can be made more compliant by cutting out material, so that deformations are local and do not extend to the middle of the chip near the membrane. In this way the epoxy is able to shrink, deforming the top chip locally, without transferring that strain to the posts or to the middle of the chip. We also switched to only epoxying in two places to not over constrain the ways the chip can bend. Figure 7.2 shows a simulation of the chip bow for the final design of the top chip. The post spacing is set to null out motion near the membrane. By keeping the epoxy on the edge but changing the location of the posts the force on the middle of the chip can be swept from up to down through zero, which allows us to null out deformation at the membrane.

7.1.3 Fabrication challenge and solution: silicon frames patterned with holes

The cutouts used to increase chip compliance and improve mechanical isolation rely on new fabrication techniques in order to make them compatible with the flip-chip geometry. The new top chip fabrication involves three etches that are deeper than a few microns: one to etch trenches for dust, one for releasing the membrane, and the new one for the cutouts. Standard lithographic

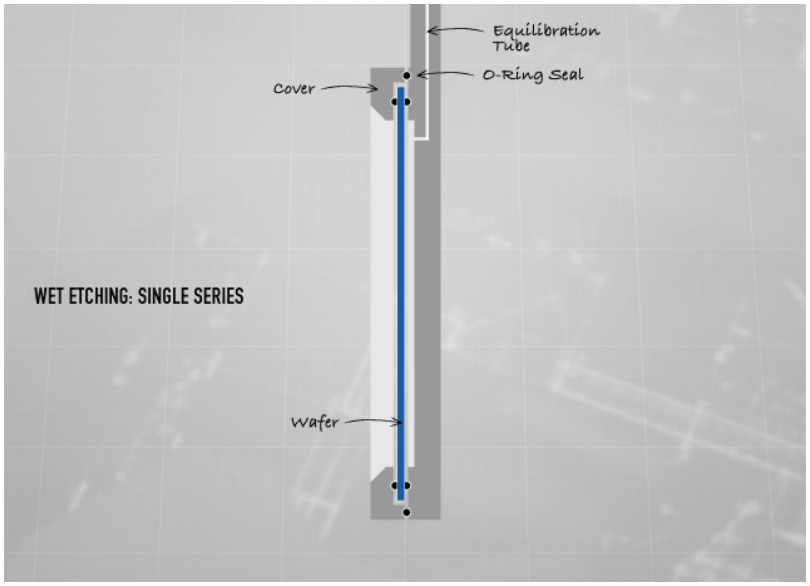

Figure 7.3: **One sided etch jig.** Profile view. The jig uses o-rings to seal around the wafer. When lowered into an etch solution, only one side is exposed. The equilibrium tube is for balancing pressure on the final released membranes. The concept is the same for wafers or for chips. We fabricate different jigs to accommodate different size chips. Photo from A.M.M.T https://www.ammt.com/products/wet-etching/single-series/

techniques require relatively smooth surfaces, and deep features are usually reserved for the last step. If that is not possible there do exist some solutions: spray-on resist and resist tape. Resist tape did not work for our application because it could not protect the already released membranes, and the spray-on technique was not pursued. We were able to implement two deep etches in our initial fabrication process by using a backside etch to release the membrane so that each deep etch lithography could be done on a smooth surface.

We developed a way to protect the released membranes and allow for an additional lithographic step over the uneven surface. The solution not only allowed for the fabrication of membranes with arbitrary cutouts in the surrounding silicon frame, but also reduced the longest single step in the fabrication from ~ 6 hours to ~ 1 hr and enabled a wafer-scale process for this step. The KOH etch that releases the membrane attacks silicon along its crystalline axis, which means that any exposed Si will be etched and the trenched side of the wafer must be protected. In our initial fab process, this KOH etch was the last step, and was done chip-scale with jigs to enable a one-sided

etch as shown in Figure 7.3. The slow etch rate of KOH (~ 1 μm/minute through a 380 μm chip) together with the chip-scale nature and 60% yield of this process made it painfully slow compared to the rest of the wafer-scale fabrication. We reduced the etch time by using deep reactive ion etching (DRIE) to etch through all but the last ~ 10 μm of silicon. Using a one sided jig for a wafer scale etch is not possible due to the low yield. If even a single membrane breaks, KOH can leak through and expose the entire side that is supposed to be protected by the jig. Instead, we protect the trenched side of the wafer by bonding it to a sapphire backing wafer using wax (Crystalbond$^{\text{TM}}$ 509). The wax dissolves in KOH so this is not a standard practice. However, the backing wafer confines the exposed area to a very thin surface of wax that it dissolves slowly simply due to lack of access. Over the duration of the shorter etch enabled by the DRIE technique, only on the outer ~ 1 mm of the wafer is the wax dissolved and the exposed silicon etched. This is not a problem because no chips are patterned that close to the edge of the wafer. Compared to a jig method, a membrane breaking is not catastrophic with the wax method. If a membrane breaks the KOH only reaches ~ 1 mm around the membrane which is not a problem for the rest of the wafer as seen in Figure 7.4.

After the membranes are released, the final step is to fill the membrane holes with resist so that another lithography and etch step can dice the chips and pattern the tethers. At this point in the fab process the wafer has deep trenches on the membrane side and holes all the way to the membrane on the other making standard lithography difficult. The released membranes are also very fragile and need to be protected for further processing. The problem of patterning on the uneven surface is solved by unconventional lithography methods. The wafer is again bonded to a sapphire backing wafer with wax, with the membrane side down for protection. The membrane holes are then filled individually with photoresist and a paintbrush. This can be a very challenging and tedious task as a wafer can have as many as 70 chips on it and the membrane hole is 0.5 mm on a side. This process needs to be done iteratively by applying resist, then baking, then more resist until each membrane hole is full. If it is not done meticulously enough, bubbles build up in the resist that burst when baking and expose the membrane to the etch. Finally, the surface is

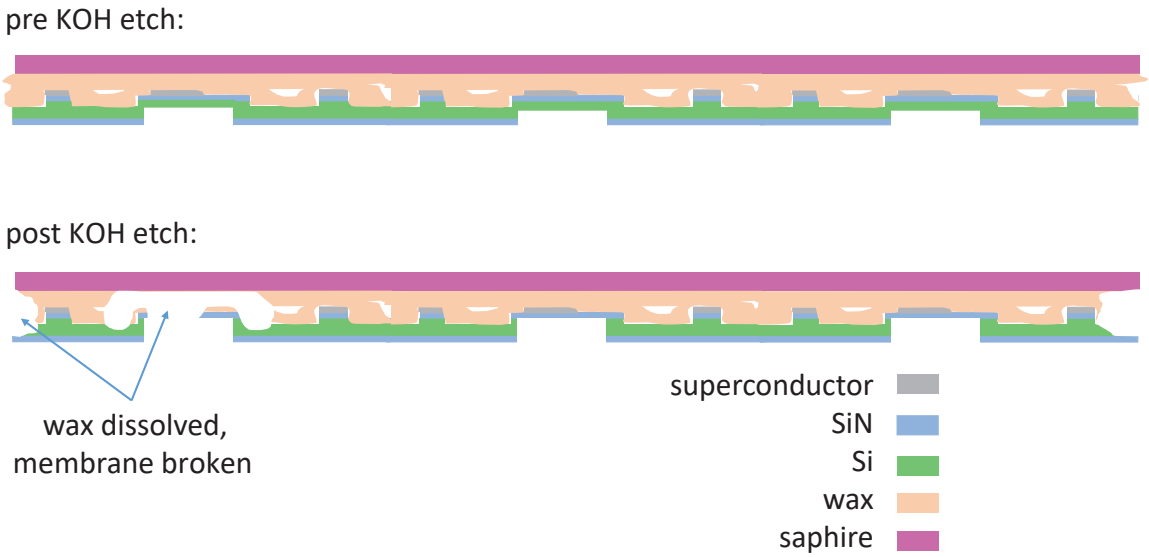

Figure 7.4: **Profile schematic of wafer scale KOH etch.** Not to scale. A sapphire wafer is affixed with wax onto the silicon wafer of top chips. Wafer is placed in wet KOH etch. The wafer in the diagram has three chips across for simplicity. The actual wafer has 70 chips on it. Prior to this step the wafer has a ~ 10 μm layer of silicon over membranes that is etched by KOH to release them. The KOH dissolves the wax from the edges and etches the exposed silicon. Wax dissolves slow enough that only edge of wafer is affected and chips are not compromised. If a membrane breaks, the etch only gets through in a small region around the broken membrane and does not touch any other chips.

smooth enough and even layer of resist can be applied using standard techniques.

7.2 Parameter noise

High-Q and low-noise superconducting microwave resonators are desirable for many applications, ranging from quantum computing [117] to particle acceleration [118] to photon detection [119]. Although the details of noise mitigation depend sensitively on geometry, reducing noise and loss invariably involves making very clean superconductors and concentrating fields away from lossy dielectrics. Therefore, fabrication of low-loss circuits with little excess noise requires addressing each potential source by optimizing the surface cleanliness [120, 121, 122], the etch chemistry [122, 123, 124], the surface interfaces [125], and the choice of superconductor [123, 126]. For a good review of parameter noise in superconducting circuits see Gao's thesis [127]. One com-

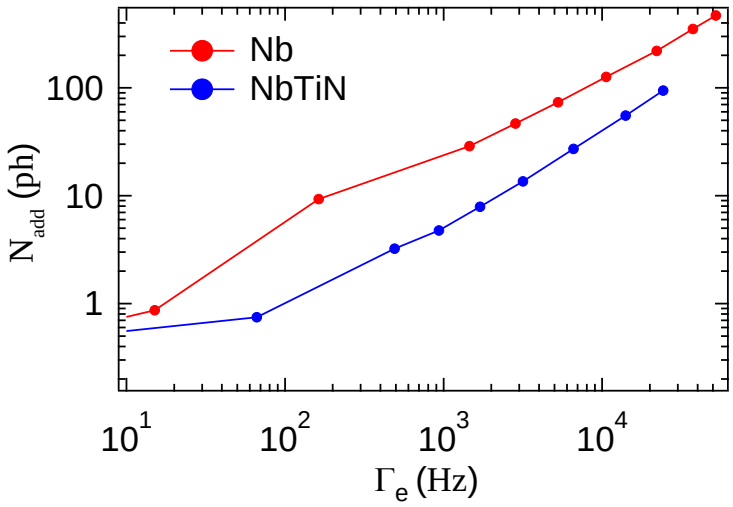

Figure 7.5: **NbTiN vs Nb added noise.** Parameter noise contribution to added noise budget for NbTiN devices compared to Nb. There is a factor of 4 reduction for a given electromechanical damping rate. The NbTiN is not measured in a converter device but is inferred from from noise performance of test devices assuming constant electromechanical coupling g_0, and that the microwave circuit performance is unaffected by integration into an optical cavity.

mon source of noise is two level system (TLS) dissipation, and therefore much of the literature is dedicated to understanding and reducing this noise source. Our circuits show some of the characteristics of TLS noise at low power, but deviated from the expectation at higher powers. The high-power regime is where parameter noise is our limiting factor, and therefore we focus on finding a solution for that range. Even though the origin of the parameter noise observed at high pump powers is not understood, borrowing practices from the literature to make high-Q, low-noise resonators still helped alleviate our problem. We measured frequency noise and loss as a function of power for a variety of devices with different circuit dimensions, etch processes, and materials, using the number of noise photons that would be added to a conversion process as our final figure of merit. The change that had the largest positive effect was changing the superconductor from niobium to NbTiN.

Switching our superconductor to NbTiN reduced the parameter noise for a given drive power by 6 dB. The superconducting properties of NbTiN are very process-dependent. We follow a

process that was developed at NIST [128] and was modified from a titanium nitride (TiN) film deposition also developed at NIST [126]. The investigation for using nitrided super conductors was first pursued at NIST based on work out of JPL using TiN for microresonator detectors [129]. The deposition is done by co-sputtering pure Nb and Ti targets at 500 °C in an Ar : N_2 atmosphere with 4 W RF, 100 V DC self bias on the substrate. The substrate is first cleaned in HF to remove native oxides. The deposition starts by growing a thin layer of SiN which selects the correct grain structure of NbTiN. The Nb:Ti ratio is controlled by the RF power on each gun. This recipe has been optimized to give a T_C of 13.8 K. Because any dry etch has the potential to roughen the SiN membrane and increase optical loss, a wet etch is used to define the NbTiN circuit. We use a SiO2 hard mask and a NH_4OH wet etch. Full fabrication details are in appendix A.

Figure 7.5 shows the projected added noise for a NbTiN device compared to Nb. For speed of testing we measured parameter noise in devices without released membranes or optical cavity integration. Therefore the added noise for the NbTiN device is the projected added noise for converter if the only change was switching to NbTiN.

The improvement from NbTiN can be further understood by looking at internal loss and frequency noise in our NbTiN resonators. The first indicator that it is an improvement is seen in the internal loss shown in Figure 7.6a. The NbTiN device has lower loss overall which is generally good and will result in lower loss in the microwave part of the converter, but more importantly it doesn't exhibit the sharp increase at high powers. The sharp increase in loss is correlated to the excess noise we observe. The low-power behaviour of the NbTiN device is characteristic of TLS noise. As the power is increased the loss decreases at first as loss from TLSs is saturated. The loss increases again at high power, but not as drastically as in the Nb device. The parameter noise may also be characterized in terms of the LC circuit's fractional frequency noise spectrum evaluated at the mechanical resonance frequency, shown in Figure 7.6b. The fractional frequency noise is independent of specific device parameters such as circuit linewidths and couplings and thus is a more accurate measure of the underlying material noise processes. We see that the NbTiN device levels off to a lower value at high power. The fractional frequency noise at low powers matches what

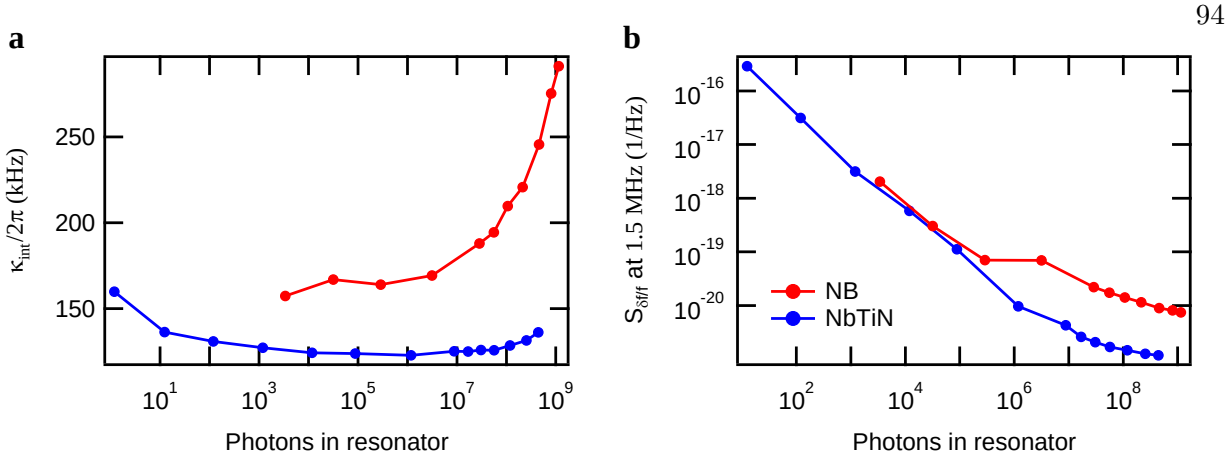

Figure 7.6: **Nb NbTiN loss and noise comparison. a,** Internal loss as number of photons in resonator is varied. Blue trace is NbTiN. Red is Nb. **b,** Fractional frequency noise at 1.5 MHz as function of photons in resonator.

is expected for TLS noise and the deviation from this at high powers corresponds to the excess parameter noise we observe.

Prior to settling on NbTiN, we tried several different modifications to our fabrication procedure to diagnose and try to mitigate parameter noise. Here we motivate a few of the tests and highlight results that may have not solved the parameter noise but were still helpful. Parameter noise has been studied extensively in CPW resonators whose geometry is quite different from ours. In the CPW resonators, the field lines mainly go through the metal-insulator interface due to the high dielectric constant of the substrate compared to air. In our geometry most of the electric field lines live in the gap between the two capacitor plates and therefore pass through the metal-air interface. Therefore, we worried about surface cleanliness such as dirty oxides, residues from etches, and electric field density. Most of our test devices exhibited no change in noise performance. Some devices of interest are discussed briefly here. One was a flip chip assembled from an NbTiN bottom chip and a Nb top chip. This had low loss at low powers but had the sharp uptick at high powers, suggesting that the loss and parameter noise are therefore not associated only with the bottom chip. Another device of interest used 100 nm of Nb on the top chip compared to the usual 25 nm. This chip also had lower loss than most Nb chips, but did not have improved noise

performance, suggesting that increasing the metal thickness on the top chip could be beneficial for reasons unrelated to parameter noise. Realizing this benefit will required careful optimization as increasing the thickness of the top chip metal also reduces the membrane's zero point motion and g_0.

The contribution to the total added noise budget due to LC parameter noise has been reduced by a factor of four by switching from Nb to NbTiN. While the factor of four improvement is obviously helpful, it will not be sufficient for quantum operation without an improvement in either the coupling rate or the mechanical dissipation, either of which would mean it would reduce the electromechanical pump power required to achieve the same level of thermal added noise.

7.3 Bonding technique for flip-chips and optical cavity assembly

We implemented SiO_2-Si bonding process to create etalons and flip-chips without epoxy. This procedure allows us to produce flip-chip devices that are immune to the effects of epoxy shrinking on the capacitor gap separation. It also produces etalons in a highly scalable way with very good alignment between the mirror and membrane (< 1 mrad). The alignment is ensured because the bond depends on the two flat surfaces being in intimate contact, so if the bond forms the surface will be aligned to the membrane to the degree that the wafers are flat. Removing the epoxy between the surfaces also ensures that the etalon remains well-aligned upon cooling down.

The recipe we follow for the bonding process was developed at NIST for wafer scale bonding to make frequency combs in suspended silicon waveguides [130]. A summary of the technique follows and full details are in appendix A. The substrates are cleaned with an ultrasound solvent bath and an aggressive O_2 plasma to remove any organics. Surface bonds are activated in a atmospheric plasma system in a $N_2 : H_2$ plasma making it hydrophilic. Substrates are rinsed in water to activate and saturate $-$OH groups. An initial bond is formed by Van der Waals forces between the hydroxyl groups which is then made permanent by annealing at 150 °C for an hour. The annealing process replaces the OH-OH bonds with stronger Si-O-Si bonds. The strength of the final bond can by increased by annealing at higher temperature for more time, but 150 °C is both strong enough for

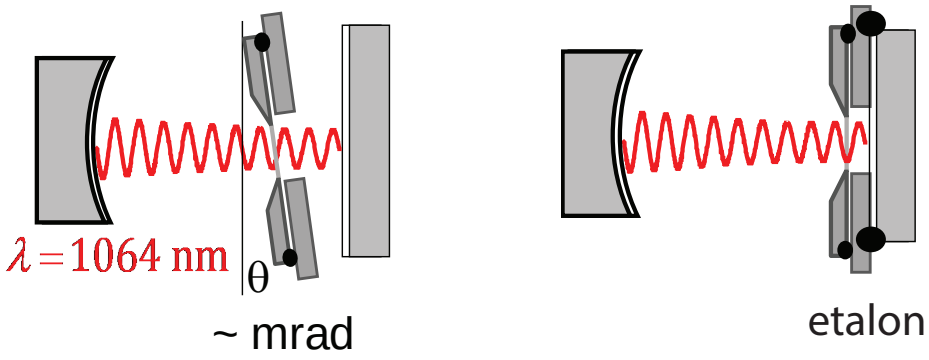

Figure 7.7: **Etalon is naturally aligned.** Three-element cavity on left shows potential for misalignment. Two-element cavity on right consists of a mirror and a etalon. The etalon is formed between the membrane and the flat mirror. These two pieces are structurally robust to misalignment and thus the whole thing behaves as a stable cavity.

our purposes and compatible with the metal thin films of our circuit. For example, annealing at 900 °C can increase the bond strength up to the fracture strength of the wafers.

7.3.1 Etalons

Moving from a three-element cavity to a two-element cavity makes the optical resonator more robust to misalignment and importantly facilitates making the cavity shorter. We refer to the new design as a two-element cavity with the two elements being a mirror and an etalon as shown in Figure 7.7. The etalon is really two elements in itself, the other mirror and the membrane, but by making them structurally the same piece, they behave like a single mirror with periodic wavelength-dependent transmission The short cavity is important for optomechanical coupling, while the robustness to misalignment is important for reducing cavity scattering losses. The etalon allowed us to move back to wired microwave coupling with a shorter optical cavity than in the first-generation design by reducing the number of components in the physical support structure.

The etalons have shown to be much more robust to misalignment on cooling down but this comes at the cost of cavity tunability. Using an etalon leaves us with only one cavity tuning knob while cold. In the three-element cavity there is a piezoelectric actuator on each mirror. One is used

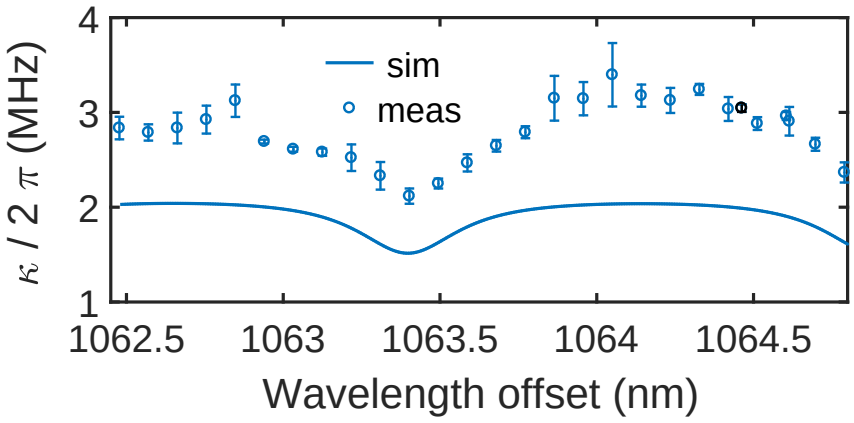

Figure 7.8: **Self-aligned etalon cavity.** Measured and simulated cavity linewidth as a function of wavelength. This is equivalent to moving membrane in the standing wave of the cavity. Cavity still has excess loss, but this loss is independent of membrane position in the optical fringe. Compare to Figure 6.8

for locking the cavity to the laser while the other is used for moving the membrane in the standing wave. The piezo for locking has so far been critical, and therefore adopting etalons we forfeit the ability to move the membrane. An equivalent method to move the standing wave relative to the membrane is to tune the wavelength of the laser. This is the technique used to produce Figure 7.8. The cavity linewidth as a function of laser wavelength in two-element cavities is well behaved. There is still the excess loss above the expected value from mirror transmissions alone, but there are no longer narrow regions with large loss indicative of hybridization when compared to Figure 6.8. We associate this with a more well aligned cavity.

We tried two other etalon assembly methods (shown in Figure 7.9) before settling on the bonding method discussed above. Our first attempt involved simply setting a mirror on a chip and applying epoxy to the edge. This produced etalons with angular misalignment between the membrane the flat mirror ranging from 0.1 mrad to 0.8 mrad, mainly limited by epoxy wicking between the two surfaces. The low end of this range works for our application, but we still pushed for a more reliable and less time-consuming fabrication method. Our second approach was optically contacting chips to mirrors on fused silica substrates. Optical contacting relies on two surfaces

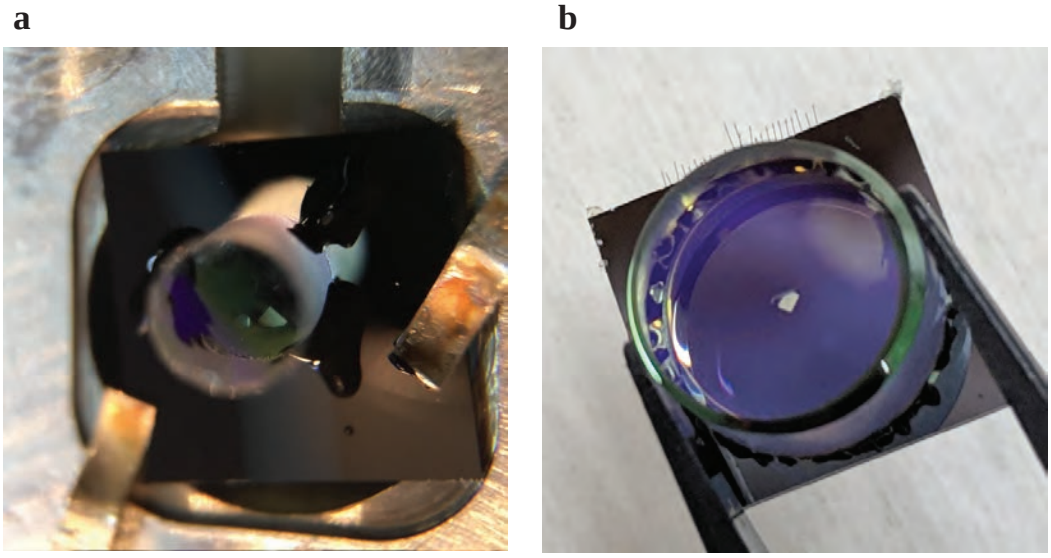

Figure 7.9: **Etalon assembly methods. a,** Epoxied etalon. No intimate contact between mirror and chip. Epoxy wicking under leads to misalignment. **b,** Optically contacted etalon backed up with epoxy. Has reliable, robust mirror-membrane alignment.

being extremely flat and clean, so that by touching them together the two surfaces stick together by Van der Waals forces. We subsequently painted epoxy around the bonded surface to protect the relatively weak bond during thermal cycling, and verified this epoxy did not affect the etalon alignment. This produced good alignment at reliably < 0.3 mRad, but the yield was limited due to the strict cleanliness requirements that were difficult to achieve even in a cleanroom. Our third approach was SiO2 bonding, which preserved the alignment reliability and works at the wafer scale, dramatically increasing production numbers. We switched our mirror substrates from fused silica pieces that were the size of a single chip, to 3" silicon wafers. The wafer scale bonding technique described above produced an entire set of bottom chips with mirrors attached. Flip-chips are then produced with the well-aligned etalon built in.

7.3.2 Chip bonding

Perhaps one of the largest contributions of this thesis has been simply reducing the number of epoxy joints in the electro-optic converter. Epoxy has been a constant source of variability from

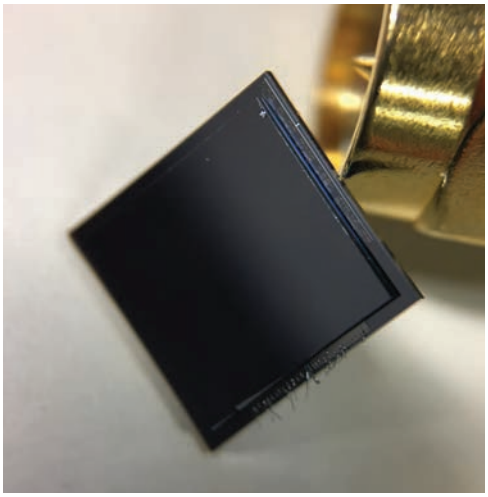

Figure 7.10: **Flip-chip bonded without epoxy.** Test flip-chip bonded with SiO_2 posts. Notice lack or epoxy anywhere on edges or corners. No membrane in test chips. These chips were used to test microwave properties, infer gap separations, and ensure bonds survived thermal cycling.

device to device and misalignment of both the LC circuit and optical cavity, and using bonded etalons reduced the number of epoxy joints in the optical cavity by half. The bonding method has also allowed us to make flip-chips without epoxy. This eliminates flexing of the top and bottom chips relative to each other on thermal cycling, improves the number of thermal cycles the chips can handle, and reduces variability from thermal cycle to thermal cycle. The bonding technique was developed for wafer-scale bonding of pristine surfaces, but we were able to adapt it for chip-scale fairly easily. A flip-chip device using the bond process is shown in Figure 7.10.

Bonded flip-chips have not been integrated into the full converter yet, but they have been tested for robustness and for the effect on Q_{m}. The bond is formed over four 100 μm diameter posts. Smaller post areas were not robust enough for handling, and larger post areas made it difficult to achieve small capacitor gap separations, probably due to dust on the posts. In order to integrate the bonding process into our chip design, we replaced the Al posts previously used to set the flip-chip separation with SiO2 posts deposited using electron cyclotron resonance plasma enhanced chemical vapour deposition (ECR-PECVD) deposited SiO_2. The ECR-PECVD process was chosen for its clean, reliable-thickness depositions, but also importantly for its low-energy growth. Thermally

grown or high-energy depositions would ruin the NbTiN thin film which is constrained to be the first step due to its high-temperature deposition. The chips that were temperature cycled repeatedly and showed gap separations as reliable as our best devices with the stress compensation for epoxy.

Bonded chips produced mechanical quality factors that were orders of magnitude worse than our improved tether designs. Only one of the tested devices achieved $Q_{\mathrm{m}} > 5 \times 10^5$ and that device had the middle posts etched away to eliminate contact area inside the tethers. This suggests that when the chips really are in intimate contact, placement of points of contact relative to the tethers matters a lot. This was obviously not what we hoped to find, but is valuable for a few reasons. It suggests that while bonding does limit the achievable Q_{m} with standard chip designs, there are routes to improve it. For example a phononic shield in the top chip inside of the joints should reduce the radiative loss. Another more extreme example would be make the top chip much smaller and put a phononic shield outside it in the bottom chip.

7.4 Frequency-independent coupling

A method of coupling to the LC circuit that is less frequency dependent is developed. Even with the capacitor gap improvements, the capacitance is still a relatively uncontrolled variable leading to a range of frequencies and therefore to a range of external couplings, and this variation is exacerbated by smaller gap spacings. The coupling method determines the frequency scaling for external coupling dependence. The wireless coupling allowed us to make smaller optical cavity length, produced our lowest loss and most stable optical cavity. However, because the microwave circuit is resonantly coupled to the 3D cavity, the external coupling rate to the transmission line the external coupling rate is highly sensitive to the frequency of the LC circuit. The etalon cavity geometry allows us to preserve the short optical cavity length while returning to wired connections to the chip.

In contrast to the 3D cavity coupling, inductive coupling on chip can be designed to have nearly no dependence on the LC frequency. The 3D wireless cavity is resonantly coupled and

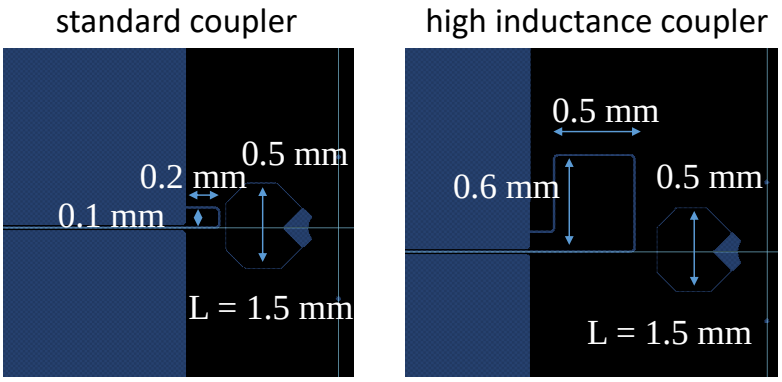

Figure 7.11: **High inductance coupler reduces frequency dependence.** Designs are shown for the bottom chip including the CPW, coupler and resonator. The left shows our standard coupler used in wired designs. The right shows a higher inductance coupler that reduces the frequency dependence of a variable capacitor gap separation.

therefore scales as $1/\Delta^2$ (equation 3.1). For an on-chip inductive coupler, the external coupling is

$$\kappa_{\text{ext}} = \frac{1}{L}\frac{\omega^2 M^2 Z_0}{Z_0^2 + \omega^2 L_c^2}. \tag{7.2}$$

Where M is the mutual inductance, L_c is the coupling inductance, Z_0 is the impedance of the transmission line, and the expression should be evaluated at $\omega = \omega_{\text{LC}}$. Our original wired coupling design with a small inductive loop coupler operated in the $\omega L_c \ll Z_0$ limit, where

$$\kappa_{\text{ext}} \sim \frac{1}{L}\frac{\omega^2 M^2}{Z_0}. \tag{7.3}$$

If the frequency changes due to a change in the capacitance then the coupling will scale as $\mathcal{O}(\omega^2)$. In the limit that $\omega L_c \gg Z_0$

$$\kappa_{\text{ext}} \sim \frac{Z_0 M^2}{L_c^2}. \tag{7.4}$$

In this case, if the capacitance changes then the external coupling will remain constant. In our experiment the capacitance is an unknown quantity until we cool down, so in order to set the coupling constant across the frequency band we should work in the regime where $\omega L_c \gg Z_0$. This corresponds to making a very large coupling inductor. In practice one can't make L_c arbitrarily large before its self capacitance will cause it to look like a resonator and we would be back to the same resonant coupling scheme of the 3D cavity.

noise source	noise photons	
	high efficiency device	projected improvements
parameter noise	23	1.4
generator phase noise	2	0.5
thermal motion	7	0.7
laser heating	2	2.0
total	34	4.6

Table 7.1: **Added noise budget including all improvements.** Measured added noise budget for our high-efficiency device and projected noise budget for a device that implements all improvements. The high efficiency device reached $\eta = 47\%$ and was the focus of Chapter 4. The converter efficiency is taken to be the same for the device with improvements.

The coupling design is shown if Figure 7.11. This larger loop is not quite in the regime where $\omega L_c \gg Z_0$, but it still reduces the frequency dependence. The coupling is simulated and measured to have a roughly linear dependence on ω dependence across the $4 - 8$ GHz frequency band. This allows us to make devices that all have a external coupling rate that will leave us highly overcoupled but still sideband resolved.

7.5 Improvements summary

Although a converter experiment has not been run with these improvements, they have all been independently tested and are ready to be implemented. A finished flip-chip with all these improvements (except the etalon) is shown in Figure 7.12. The noise budget of the high-efficiency device is shown in table 7.1, along with a projected noise budge for a converter incorporating all these improvements, using a conservative estimate of the efficiency. The efficiency used to calculate the projected noise budget is $\eta = 47\%$ as in our best device because even using two-element optical cavities, we still have yet to achieve the best expected optical efficiency due to excess loss. The expected optical efficiency corresponds to an overall efficiency of 75%, which would further reduce the total added noise by a factor of 1.5. The parameter noise has been reduced by a factor of four from reducing the gap size by a factor of two and another factor of four from switching from Nb to NbTiN. Smaller gap size also reduces the contribution from generator phase noise. Improvements

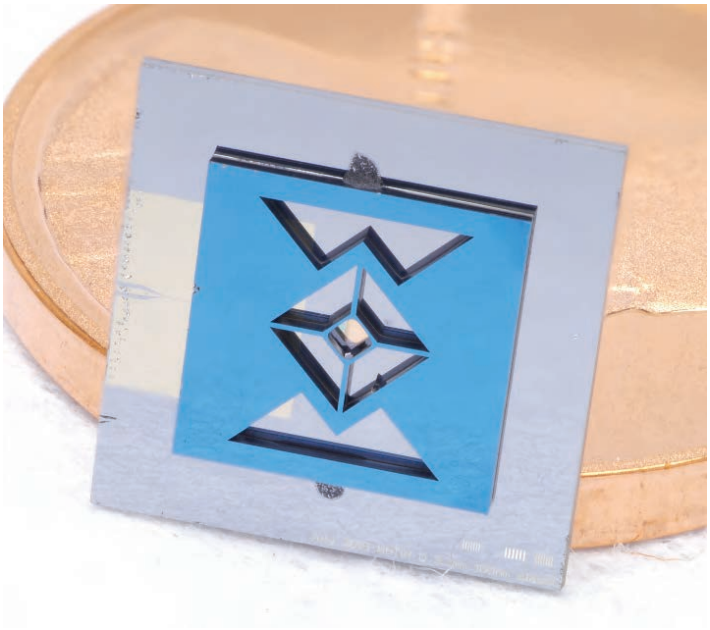

Figure 7.12: **Photo of improved transducer chip.** Photo of fabricated device with NbTiN, wired coupling, strain relief, and mechanical isolation cutouts.

in Q_{m} reduce the contribution from thermal phonons by a factor of 10. The laser heating of the LC circuit could improve with the switch to NbTiN or by the improvements to the optical cavity, but since it has not been tested the value is left the same. The total of the noise budget is still greater than one, which would preclude any quantum operation. However, the order of magnitude improvement is a large milestone towards quantum operation, and serves to elucidate where we need to focus our efforts moving forward.

Chapter 8

Conclusion and Outlook

This thesis shows improvements to our microwave optical converter that allowed for the highest conversion efficiency $\eta = 47\%$ and a record lowest added noise $N_{\mathrm{add}} = 13$ photons. The discovery of correlations in the noise at each port led to a feedforward protocol that presents an alternative path to quantum operation, even if thermal noise couples into the mechanical oscillator faster than the conversion rate. The device was studied in depth to understand the added noise limitations and to make improvements that address each source. The solutions found represent significant technical progress that would reduce the added noise to nearly the quantum threshold. With a little luck or ingenuity, this device could even operate below one photon with little to no further improvements than developed here.

The improvements made individually address each source of added noise and present a path towards reducing added noise to close to a single photon. Making a microwave optical converter that realizes all the improvements simultaneously has not yet been achieved. The largest impediment has been the effect of the etalons on the microwave chips. Bonding mirrors to the bottom chip reduces Q_{m} and alters the capacitor gap separation. Different coefficients of thermal expansion of the mirror substrate and coating flex the flip-chip causing the capacitor to collapse. The mirror also reduces the mechanical quality factor by an order of magnitude ($Q_{\mathrm{m}} \sim 10^4$) compared to the plain membranes.

There are hopeful solutions to both these problems. The collapse issue has been solved in test devices that use Si mirror substrates with coating layers removed to match thermal contractions.

The mechanical dissipation can be improved again by implementing a PNC design as discussed in Chapter 7.

The next steps involve further reducing the added noise and integrating this converter into more complex experimental setups. Even if the added noise is still above one photon there are interesting experiments that could be done. For instance, an ongoing effort in our group is to use the converter to optically readout a superconducting qubit. The experimental effort would test qubit operation in the same dilution refridgerator as an optical component, which is an important question given the long term goal of linking superconducting quantum computers via optical fiber. The converter could also be used with optical single photon counting infrastructure, which gives access to discrete variable entanglement schemes that are more robust to photon loss and can achieve high fidelity entanglement at the cost of lower success rate without needing high efficiency transduction [96, 97, 98, 99].

Bibliography

[1] A. G. J. MacFarlane, J. P. Dowling, and G. J. Milburn, "Quantum technology: the second quantum revolution," Philosophical Transactions of the Royal Society of London. Series A: Mathematical, Physical and Engineering Sciences, vol. 361, no. 1809, pp. 1655–1674, 2003. [Online]. Available: https://royalsocietypublishing.org/doi/abs/10.1098/rsta.2003.1227

[2] A. Einstein, B. Podolsky, and N. Rosen, "Can quantum-mechanical description of physical reality be considered complete?" Phys. Rev., vol. 47, pp. 777–780, May 1935. [Online]. Available: https://link.aps.org/doi/10.1103/PhysRev.47.777

[3] E. SCHRDINGER, "ARE THERE QUANTUM JUMPS ?: PART II*," The British Journal for the Philosophy of Science, vol. III, no. 11, pp. 233–242, 11 1952. [Online]. Available: https://doi.org/10.1093/bjps/III.11.233

[4] R. P. Feynman, "Quantum mechanical computers," Foundations of Physics, vol. 16, no. 6, pp. 507–531, Jun 1986. [Online]. Available: https://doi.org/10.1007/BF01886518

[5] ——, "Simulating physics with computers," International Journal of Theoretical Physics, vol. 21, no. 6, pp. 467–488, Jun 1982. [Online]. Available: https://doi.org/10.1007/BF02650179

[6] D. E. Deutsch and R. Penrose, "Quantum computational networks," Proceedings of the Royal Society of London. A. Mathematical and Physical Sciences, vol. 425, no. 1868, pp. 73–90, 1989. [Online]. Available: https://royalsocietypublishing.org/doi/abs/10.1098/rspa.1989.0099

[7] D. Deutsch and R. Penrose, "Quantum theory, the church–turing principle and the universal quantum computer," Proceedings of the Royal Society of London. A. Mathematical and Physical Sciences, vol. 400, no. 1818, pp. 97–117, 1985. [Online]. Available: https://royalsocietypublishing.org/doi/abs/10.1098/rspa.1985.0070

[8] P. W. Shor, "Algorithms for quantum computation: discrete logarithms and factoring," in Proceedings 35th Annual Symposium on Foundations of Computer Science, Nov 1994, pp. 124–134.

[9] R. L. Rivest, A. Shamir, and L. Adleman, "A method for obtaining digital signatures and public-key cryptosystems," Commun. ACM, vol. 21, no. 2, pp. 120–126, Feb. 1978. [Online]. Available: http://doi.acm.org/10.1145/359340.359342

[10] C. Bennett and G. Brassard, "Quantum cryptography: Public key distribution and coin tossing," Theoretical Computer Science - TCS, vol. 560, pp. 175–179, 01 1984.

[11] J. L. Park, "The concept of transition in quantum mechanics," Foundations of Physics, vol. 1, no. 1, pp. 23–33, Mar 1970. [Online]. Available: https://doi.org/10.1007/BF00708652

[12] P. A. Hiskett, D. Rosenberg, C. G. Peterson, R. J. Hughes, S. Nam, A. E. Lita, A. J. Miller, and J. E. Nordholt, "Long-distance quantum key distribution in optical fibre," New Journal of Physics, vol. 8, no. 9, pp. 193–193, sep 2006. [Online]. Available: https://doi.org/10.1088%2F1367-2630%2F8%2F9%2F193

[13] B. Korzh, C. C. W. Lim, R. Houlmann, N. Gisin, M. J. Li, D. Nolan, B. Sanguinetti, R. Thew, and H. Zbinden, "Provably secure and practical quantum key distribution over 307 km of optical fibre," Nature Photonics, Feb 2015.

[14] J. Yin, Y. Cao, Y.-H. Li, S.-K. Liao, L. Zhang, J.-G. Ren, W.-Q. Cai, W.-Y. Liu, B. Li, H. Dai, G.-B. Li, Q.-M. Lu, Y.-H. Gong, Y. Xu, S.-L. Li, F.-Z. Li, Y.-Y. Yin, Z.-Q. Jiang, M. Li, J.-J. Jia, G. Ren, D. He, Y.-L. Zhou, X.-X. Zhang, N. Wang, X. Chang, Z.-C. Zhu, N.-L. Liu, Y.-A. Chen, C.-Y. Lu, R. Shu, C.-Z. Peng, J.-Y. Wang, and J.-W. Pan, "Satellite-based entanglement distribution over 1200 kilometers," Science, vol. 356, no. 6343, pp. 1140–1144, 2017. [Online]. Available: https://science.sciencemag.org/content/356/6343/1140

[15] S. L. Braunstein and C. M. Caves, "Statistical distance and the geometry of quantum states," Phys. Rev. Lett., vol. 72, pp. 3439–3443, May 1994. [Online]. Available: https://link.aps.org/doi/10.1103/PhysRevLett.72.3439

[16] H. Miao, H. Yang, R. X. Adhikari, and Y. Chen, "Quantum limits of interferometer topologies for gravitational radiation detection," Classical and Quantum Gravity, vol. 31, no. 16, p. 165010, 2014. [Online]. Available: http://stacks.iop.org/0264-9381/31/i=16/a=165010

[17] L. K. Grover, "Quantum mechanics helps in searching for a needle in a haystack," Phys. Rev. Lett., vol. 79, pp. 325–328, Jul 1997. [Online]. Available: https://link.aps.org/doi/10.1103/PhysRevLett.79.325

[18] M.-H. Yung, J. D. Whitfield, S. Boixo, D. G. Tempel, and A. Aspuru-Guzik, Introduction to Quantum Algorithms for Physics and Chemistry. John Wiley Sons, Ltd, 2014, pp. 67–106. [Online]. Available: https://onlinelibrary.wiley.com/doi/abs/10.1002/9781118742631.ch03

[19] M. Hastings, D. Wecker, B. Bauer, and M. Troyer, "Improving quantum algorithms for quantum chemistry," Quantum Information and Computation, vol. 15, 03 2014.

[20] D. Poulin, M. B. Hastings, D. Wecker, N. Wiebe, A. C. Doberty, and M. Troyer, "The trotter step size required for accurate quantum simulation of quantum chemistry," Quantum Info. Comput., vol. 15, no. 5-6, pp. 361–384, Apr. 2015. [Online]. Available: http://dl.acm.org/citation.cfm?id=2871401.2871402

[21] J. I. Cirac, P. Zoller, H. J. Kimble, and H. Mabuchi, "Quantum state transfer and entanglement distribution among distant nodes in a quantum network," Phys. Rev. Lett., vol. 78, pp. 3221–3224, 1997.

[22] A. K. Ekert, "Quantum cryptography based on Bell's theorem," Phys. Rev. Lett., vol. 67, pp. 661–663, 1991.

[23] J. I. Cirac, A. K. Ekert, S. F. Huelga, and C. Macchiavello, "Distributed quantum computation over noisy channels," Phys. Rev. A, vol. 59, pp. 4249–4254, 1999.

[24] W. Dür and H.-J. Briegel, "Entanglement purification for quantum computation," Phys. Rev. Lett., vol. 90, p. 67901, Feb. 2003.

[25] H. J. Kimble, "The quantum internet," Nature, vol. 453, no. 7198, pp. 1023–1030, 2008. [Online]. Available: http://dx.doi.org/10.1038/nature07127

[26] M. H. Devoret and R. J. Schoelkopf, "Superconducting Circuits for Quantum Information: An Outlook," Science, vol. 339, no. 6124, pp. 1169–1174, 2013. [Online]. Available: http://www.sciencemag.org/content/339/6124/1169.abstract

[27] J. Kelly, R. Barends, A. G. Fowler, A. Megrant, and E. Jeffrey, "State preservation by repetitive error detection in a superconducting quantum circuit," Nature, vol. 519, pp. 66–69, 2015.

[28] N. Ofek, A. Petrenko, R. Heeres, P. Reinhold, Z. Leghtas, B. Vlastakis, Y. Liu, L. Frunzio, S. M. Girvin, L. Jiang, M. Mirrahimi, M. H. Devoret, and R. J. Schoelkopf, "Extending the lifetime of a quantum bit with error correction in superconducting circuits," Nature, vol. 536, pp. 441–445, 2016.

[29] D. Loss and D. P. DiVincenzo, "Quantum computation with quantum dots," Phys. Rev. A, vol. 57, pp. 120–126, Jan 1998. [Online]. Available: https://link.aps.org/doi/10.1103/PhysRevA.57.120

[30] L. M. K. Vandersypen, H. Bluhm, J. S. Clarke, A. S. Dzurak, R. Ishihara, A. Morello, D. J. Reilly, L. R. Schreiber, and M. Veldhorst, "Interfacing spin qubits in quantum dots and donors–hot, dense, and coherent," npj Quantum Information, vol. 3, no. 1, p. 34, 2017. [Online]. Available: https://doi.org/10.1038/s41534-017-0038-y

[31] T. Hayashi, T. Fujisawa, H. D. Cheong, Y. H. Jeong, and Y. Hirayama, "Coherent manipulation of electronic states in a double quantum dot," Phys. Rev. Lett., vol. 91, p. 226804, Nov 2003. [Online]. Available: https://link.aps.org/doi/10.1103/PhysRevLett.91.226804

[32] Y. A. Pashkin, O. Astafiev, T. Yamamoto, Y. Nakamura, and J. S. Tsai, "Josephson charge qubits: a brief review," Quantum Information Processing, vol. 8, no. 2, pp. 55–80, Jun 2009. [Online]. Available: https://doi.org/10.1007/s11128-009-0101-5

[33] E. T. Campbell, B. M. Terhal, and C. Vuillot, "Roads towards fault-tolerant universal quantum computation," Nature, vol. 549, pp. 172 EP –, Sep 2017. [Online]. Available: https://doi.org/10.1038/nature23460

[34] A. G. Fowler, A. M. Stephens, and P. Groszkowski, "High-threshold universal quantum computation on the surface code," Phys. Rev. A, vol. 80, p. 052312, Nov 2009. [Online]. Available: https://link.aps.org/doi/10.1103/PhysRevA.80.052312

[35] M. M. Wolf, D. Pérez-García, and G. Giedke, "Quantum capacities of bosonic channels," Phys. Rev. Lett., vol. 98, p. 130501, Mar 2007. [Online]. Available: https://link.aps.org/doi/10.1103/PhysRevLett.98.130501

[36] C. Rigetti, J. M. Gambetta, S. Poletto, B. L. T. Plourde, J. M. Chow, A. D. Córcoles, J. A. Smolin, S. T. Merkel, J. R. Rozen, G. A. Keefe, M. B. Rothwell, M. B. Ketchen, and M. Steffen, "Superconducting qubit in a waveguide cavity with a coherence time approaching 0.1 ms," Phys. Rev. B, vol. 86, p. 100506, Sep 2012. [Online]. Available: http://link.aps.org/doi/10.1103/PhysRevB.86.100506

[37] D. V. Strekalov, H. G. L. Schwefel, A. A. Savchenkov, A. B. Matsko, L. J. Wang, and N. Yu, "Microwave whispering-gallery resonator for efficient optical up-conversion," Phys. Rev. A, vol. 80, p. 033810, Sep 2009. [Online]. Available: https://link.aps.org/doi/10.1103/PhysRevA.80.033810

[38] A. Rueda, F. Sedlmeir, M. C. Collodo, U. Vogl, B. Stiller, G. Schunk, D. V. Strekalov, C. Marquardt, J. M. Fink, O. Painter, G. Leuchs, and H. G. L. Schwefel, "Efficient microwave to optical photon conversion: an electro-optical realization," Optica, vol. 3, no. 6, pp. 597–604, Jun. 2016.

[39] L. Fan, C.-L. Zou, R. Cheng, X. Guo, X. Han, Z. Gong, S. Wang, and H. X. Tang, "Superconducting cavity electro-optics: A platform for coherent photon conversion between superconducting and photonic circuits," Science Advances, vol. 4, no. 8, 2018. [Online]. Available: https://advances.sciencemag.org/content/4/8/eaar4994

[40] J. Verdú, H. Zoubi, C. Koller, J. Majer, H. Ritsch, and J. Schmiedmayer, "Strong magnetic coupling of an ultracold gas to a superconducting waveguide cavity," Phys. Rev. Lett., vol. 103, no. 4, p. 43603, Jul. 2009.

[41] M. Hafezi, Z. Kim, S. L. Rolston, L. A. Orozco, B. L. Lev, and J. M. Taylor, "Atomic interface between microwave and optical photons," Phys. Rev. A, vol. 85, no. 2, p. 20302, Feb. 2012.

[42] A. Imamoglu, "Cavity QED based on collective magnetic dipole coupling: Spin ensembles as hybrid two-level systems," Phys. Rev. Lett., vol. 102, p. 83602, 2009.

[43] D. Marcos, M. Wubs, J. M. Taylor, R. Aguado, M. D. Lukin, and A. S. Sørensen, "Coupling nitrogen-vacancy centers in diamond to superconducting flux qubits," Phys. Rev. Lett., vol. 105, no. 21, p. 210501, Nov. 2010.

[44] Y. Kubo, F. R. Ong, P. Bertet, D. Vion, V. Jacques, D. Zheng, A. Dréau, J. F. Roch, A. Auffèves, F. Jelezko, J. Wrachtrup, M. F. Barthe, P. Bergonzo, and D. Esteve, "Strong coupling of a spin ensemble to a superconducting resonator," Phys. Rev. Lett., vol. 105, p. 140502, 2010.

[45] L. A. Williamson, Y.-H. Chen, and J. J. Longdell, "Magneto-optic modulator with unit quantum efficiency," Phys. Rev. Lett., vol. 113, p. 203601, 2014.

[46] J. R. Everts, M. C. Berrington, R. L. Ahlefeldt, and J. J. Longdell, "Microwave to optical photon conversion via fully concentrated rare-earth-ion crystals," Phys. Rev. A, vol. 99, p. 063830, Jun 2019. [Online]. Available: https://link.aps.org/doi/10.1103/PhysRevA.99.063830

[47] T. Vogt, C. Gross, J. Han, S. B. Pal, M. Lam, M. Kiffner, and W. Li, "Efficient microwave-to-optical conversion using rydberg atoms," Phys. Rev. A, vol. 99, p. 023832, Feb 2019. [Online]. Available: https://link.aps.org/doi/10.1103/PhysRevA.99.023832

[48] J. Bochmann, A. Vainsencher, D. D. Awschalom, and A. N. Cleland, "Nanomechanical coupling between microwave and optical photons," Nat. Phys., vol. 9, no. 11, pp. 712–716, 2013.

[49] A. Vainsencher, K. J. Satzinger, G. A. Peairs, and A. N. Cleland, "Bi-directional conversion between microwave and optical frequencies in a piezoelectric optomechanical device," Appl. Phys. Lett., vol. 109, p. 33107, 2016.

[50] A. P. Higginbotham, P. S. Burns, M. D. Urmey, R. W. Peterson, N. S. Kampel, B. M. Brubaker, G. Smith, K. W. Lehnert, and C. A. Regal, "Harnessing electro-optic correlations in an efficient mechanical converter," Nature Physics, vol. 14, no. 10, 2018.

[51] A. H. Safavi-Naeini and O. Painter, "Design of optomechanical cavities and waveguides on a simultaneous bandgap phononic-photonic crystal slab," Opt. Express, vol. 18, pp. 14 926–14 943, 2010.

[52] J. T. Hill, A. H. Safavi-Naeini, J. Chan, and O. Painter, "Coherent optical wavelength conversion via cavity optomechanics," Nat. Commun., vol. 3, p. 1196, 2012.

[53] P. F. Cohadon, A. Heidmann, and M. Pinard, "Cooling of a mirror by radiation pressure," Phys. Rev. Lett., vol. 83, no. 16, pp. 3174–3177, Oct. 1999.

[54] O. Arcizet, P.-F. Cohadon, T. Briant, M. Pinard, A. Heidmann, J.-M. Mackowski, C. Michel, L. Pinard, O. Franais, and L. Rousseau, "High-sensitivity optical monitoring of a micromechanical resonator with a quantum-limited optomechanical sensor," Phys. Rev. Lett., vol. 97, p. 133601, 2006.

[55] M. Poggio, C. L. Degen, H. J. Mamin, and D. Rugar, "Feedback cooling of a cantilever's fundamental mode below 5 mk," Phys. Rev. Lett., vol. 99, p. 17201, 2007.

[56] C. Genes, D. Vitali, P. Tombesi, S. Gigan, and M. Aspelmeyer, "Ground-state cooling of a micromechanical oscillator: Comparing cold damping and cavity-assisted cooling schemes," Phys. Rev. A, vol. 77, no. 3, p. 33804, Mar. 2008.

[57] D. J. Wilson, V. Sudhir, N. Piro, R. Schilling, A. Ghadimi, and T. J. Kippenberg, "Measurement-based control of a mechanical oscillator at its thermal decoherence rate," Nature, vol. 524, pp. 325–329, 2015.

[58] M. Rossi, N. Kralj, S. Zippilli, R. Natali, A. Borrielli, G. Pandraud, E. Serra, G. Di Giuseppe, and D. Vitali, "Enhancing sideband cooling by feedback-controlled light," Phys. Rev. Lett., vol. 119, p. 123603, 2017.

[59] M. Rossi, D. Mason, J. Chen, Y. Tsaturyan, and A. Schliesser, "Measurement-based quantum control of mechanical motion," Nature, vol. 563, no. 7729, pp. 53–58, 2018. [Online]. Available: https://doi.org/10.1038/s41586-018-0643-8

[60] M. Poot and H. S. van der Zant, "Mechanical systems in the quantum regime," Physics Reports, vol. 511, no. 5, pp. 273 – 335, 2012, mechanical systems in the quantum regime. [Online]. Available: //www.sciencedirect.com/science/article/pii/S0370157311003644

[61] Y. Greenberg, Y. A. Pashkin, and E. Il'ichev, "Nanomechanical resonators," Physics-Uspekhi, vol. 55, no. 4, p. 382, 2012. [Online]. Available: http://stacks.iop.org/1063-7869/55/i=4/a=A03

[62] M. Aspelmeyer, T. J. Kippenberg, and F. Marquardt, "Cavity optomechanics," Rev. Mod. Phys., vol. 86, no. 4, pp. 1391–1452, Dec. 2014.

[63] J. C. Maxwell, A Treatise on Electricity and Magnetism. Clarendon Press, 1873, vol. 1.

[64] J. Kepler, Tychonis Brahei Dani Hyperaspistes. Frankfurt: Apud G. Tampachium, 1625. [Online]. Available: https://archive.org/details/tychonisbraheida00kepl

[65] A. Ashkin, "Acceleration and trapping of particles by radiation pressure," Phys. Rev. Lett., vol. 24, pp. 156–159, Jan 1970. [Online]. Available: http://link.aps.org/doi/10.1103/PhysRevLett.24.156

[66] T. Hänsch and A. Schawlow, "Cooling of gases by laser radiation," Optics Communications, vol. 13, no. 1, pp. 68 – 69, 1975. [Online]. Available: //www.sciencedirect.com/science/article/pii/0030401875901595

[67] D. J. Wineland and H. Dehmelt, "Proposed 10^{14} $\delta\nu < \nu$ laser fluorescence spectroscopy on Tl+ mono-ion oscillator," Bull. Am. Phys. Soc., vol. 20, p. 637, 1975.

[68] A. Ashkin, "Trapping of atoms by resonance radiation pressure," Phys. Rev. Lett., vol. 40, pp. 729–732, Mar 1978. [Online]. Available: http://link.aps.org/doi/10.1103/PhysRevLett.40.729

[69] D. Leibfried, R. Blatt, C. Monroe, and D. Wineland, "Quantum Dynamics of Single Trapped Ions," Rev. Mod. Phys., vol. 75, no. 1, p. 281, Mar. 2003. [Online]. Available: http://link.aps.org/doi/10.1103/RevModPhys.75.281

[70] C. M. Caves, "Quantum limits on noise in linear amplifiers," Phys. Rev. D, vol. 26, no. 8, pp. 1817–1839, Oct. 1982. [Online]. Available: http://link.aps.org/doi/10.1103/PhysRevD.26.1817

[71] M. E. Gertsenshtein and V. I. Pustovoit, "On the detection of low frequency gravitational waves," JETP, vol. 43, August 1962.

[72] R. Weiss, "Electromagnetically coupled broadband gravitational antenna," Quarterly Progress Report, Research Laboratory of Electronics, no. 105, pp. 54 – 76, 1972. [Online]. Available: https://dspace.mit.edu/bitstream/handle/1721.1/56271/RLE_QPR_105_V.pdf?sequence=1#page=38

[73] B. P. Abbott et al., "Observation of gravitational waves from a binary black hole merger," Phys. Rev. Lett., vol. 116, p. 061102, Feb 2016. [Online]. Available: http://link.aps.org/doi/10.1103/PhysRevLett.116.061102

[74] ——, "Observation of a kilogram-scale oscillator near its quantum ground state," New J. Phys., vol. 11, no. 7, p. 73032, 2009. [Online]. Available: http://stacks.iop.org/1367-2630/11/i=7/a=073032

[75] J. Aasi and others, "Enhanced sensitivity of the LIGO gravitational wave detector by using squeezed states of light," Nature Photonics, vol. 7, pp. 613–619, 2013.

[76] S. Mancini, D. Vitali, and P. Tombesi, "Optomechanical Cooling of a Macroscopic Oscillator by Homodyne Feedback," Phys. Rev. Lett., vol. 80, no. 4, pp. 688–691, Jan. 1998. [Online]. Available: http://link.aps.org/doi/10.1103/PhysRevLett.80.688

[77] S. Bose, K. Jacobs, and P. L. Knight, "Preparation of nonclassical states in cavities with a moving mirror," Phys. Rev. A, vol. 56, pp. 4175–4186, Nov 1997. [Online]. Available: https://link.aps.org/doi/10.1103/PhysRevA.56.4175

[78] J. Teufel, T. Donner, D. Li, J. Harlow, M. Allman, K. Cicak, A. Sirois, J. D. Whittaker, K. Lehnert, and R. W. Simmonds, "Sideband cooling of micromechanical motion to the quantum ground state," Nature, vol. 475, no. 7356, pp. 359–363, 2011. [Online]. Available: http://dx.doi.org/10.1038/nature10261

[79] J. Chan, T. M. Alegre, A. H. Safavi-Naeini, J. T. Hill, A. Krause, S. Gröblacher, M. Aspelmeyer, and O. Painter, "Laser cooling of a nanomechanical oscillator into its quantum ground state," Nature, vol. 478, no. 7367, pp. 89–92, 2011. [Online]. Available: http://dx.doi.org/10.1038/nature10461

[80] T. A. Palomaki, J. D. Teufel, R. W. Simmonds, and K. W. Lehnert, "Entangling mechanical motion with microwave fields," Science, vol. 342, pp. 710–713, October 2013. [Online]. Available: http://science.sciencemag.org/content/342/6159/710

[81] T. A. Palomaki, J. W. Harlow, J. D. Teufel, R. W. Simmonds, and K. W. Lehnert, "Coherent state transfer between itinerant microwave fields and a mechanical oscillator," Nature, vol. 495, no. 7440, pp. 210–214, 2013. [Online]. Available: http://dx.doi.org/10.1038/nature11915

[82] R. W. Andrews, A. P. Reed, K. Cicak, J. D. Teufel, and K. W. Lehnert, "Quantum-enabled temporal and spectral mode conversion of microwave signals." Nature Communications, vol. 6, p. 10021, May 2015. [Online]. Available: http://dx.doi.org/10.1038/ncomms10021

[83] F. Lecocq, J. B. Clark, R. W. Simmonds, J. Aumentado, and J. D. Teufel, "Mechanically mediated microwave frequency conversion in the quantum regime," Physical Review Letters, vol. 116, no. 4, p. 043601, 2016. [Online]. Available: http://link.aps.org/doi/10.1103/PhysRevLett.116.043601

[84] C. A. Regal and K. W. Lehnert, "From cavity electromechanics to cavity optomechanics," Journal of Physics: Conference Series, vol. 264, no. 1, p. 12025, 2011. [Online]. Available: http://stacks.iop.org/1742-6596/264/i=1/a=012025

[85] R. W. Andrews, R. W. Peterson, T. P. Purdy, K. Cicak, R. W. Simmonds, C. A. Regal, and K. W. Lehnert, "Bidirectional and efficient conversion between microwave and optical light," Nat. Phys., vol. 10, pp. 321–326, Mar. 2014.

[86] A. A. Clerk, M. H. Devoret, S. M. Girvin, F. Marquardt, and R. J. Schoelkopf, "Introduction to quantum noise, measurement, and amplification," Rev. Mod. Phys., vol. 82, no. 2, pp. 1155–1208, Apr. 2010.

[87] D. Morin, Quantum Optics. Berlin, Germany: Springer, 2008.

[88] J. Kerckhoff, R. W. Andrews, H. S. Ku, W. F. Kindel, K. Cicak, R. W. Simmonds, and K. W. Lehnert, "Tunable Coupling to a Mechanical Oscillator Circuit Using a Coherent Feedback Network," Phys. Rev. X, vol. 3, no. 2, p. 21013, Jun. 2013. [Online]. Available: http://link.aps.org/doi/10.1103/PhysRevX.3.021013

[89] R. Andrews, "Quantum signal processing with mechanical oscillators," Ph.D. dissertation, University of Colorado, Boulder, 2015.

[90] R. W. Peterson, T. P. Purdy, N. S. Kampel, R. W. Andrews, P.-L. Yu, K. W. Lehnert, and C. A. Regal, "Laser cooling of a micromechanical membrane to the quantum backaction limit," Phys. Rev. Lett., vol. 116, no. 6, p. 63601, 2016.

[91] T. Menke, P. S. Burns, A. P. Higginbotham, N. S. Kampel, R. W. Peterson, K. Cicak, R. W. Simmonds, C. A. Regal, and K. W. Lehnert, "Reconfigurable re-entrant cavity for wireless coupling to an electro-optomechanical device," Rev. Sci. Instrum., vol. 88, p. 94701, 2017.

[92] T. P. Purdy, R. W. Peterson, P.-L. Yu, and C. A. Regal, "Cavity optomechanics with Si_3N_4 membranes at cryogenic temperatures," New J. Phys., vol. 14, no. 11, p. 115021, 2012.

[93] R. W. Peterson, "Quantum measurement backaction and upconverting microwave signals with mechanical resonators," Ph.D. dissertation, University of Colorado, 2017.

[94] J. Thompson, B. Zwickl, A. Jayich, F. Marquardt, S. Girvin, and J. Harris, "Strong dispersive coupling of a high-finesse cavity to a micromechanical membrane," Nature, vol. 452, no. 7183, pp. 72–75, 2008.

[95] R. W. P. Drever, J. L. Hall, F. V. Kowalski, J. Hough, G. M. Ford, A. J. Munley, and H. Ward, "Laser phase and frequency stabilization using an optical resonator," Applied Physics B, vol. 31, no. 2, pp. 97–105, 1983. [Online]. Available: http://dx.doi.org/10.1007/BF00702605

[96] R. Riedinger, A. Wallucks, I. Marinkovic, C. Löschnauer, M. Aspelmeyer, S. Hong, and S. Gröblacher, "Remote quantum entanglement between two micromechanical oscillators," Nature, vol. 556, no. 7702, pp. 473–477, 2018. [Online]. Available: https://doi.org/10.1038/s41586-018-0036-z

[97] L. M. Duan, M. D. Lukin, J. I. Cirac, and P. Zoller, "Long-distance quantum communication with atomic ensembles and linear optics," Nature, vol. 414, pp. 413–418, 2001.

[98] C. H. Bennett, D. P. DiVincenzo, J. A. Smolin, and W. K. Wootters, "Mixed-state entanglement and quantum error correction," Phys. Rev. A, vol. 54, p. 3824, 1996.

[99] H.-J. Briegel, W. Dür, J. I. Cirac, and P. Zoller, "Quantum repeaters: The role of imperfect local operations in quantum communication," Phys. Rev. Lett., vol. 81, pp. 5932–5935, Dec 1998. [Online]. Available: https://link.aps.org/doi/10.1103/PhysRevLett.81.5932

[100] M. A. Castellanos-Beltran, K. D. Irwin, G. C. Hilton, L. R. Vale, and K. W. Lehnert, "Amplification and squeezing of quantum noise with a tunable josephson metamaterial," Nature Physics, vol. 4, pp. 929 – 931, 12/2008 2008. [Online]. Available: http://www.nature.com/nphys/journal/v4/n12/full/nphys1090.html

[101] C. J. Hood, H. J. Kimble, and J. Ye, "Characterization of high-finesse mirrors: Loss, phase shifts, and mode structure in an optical cavity," Phys. Rev. A, vol. 64, no. 3, p. 33804, Aug. 2001.

[102] S. L. Braunstein and H. J. Kimble, "Teleportation of Continuous Quantum Variables," Phys. Rev. Lett., vol. 80, no. 4, pp. 869–872, 1998.

[103] M. Zhang, C.-L. Zou, and L. Jiang, "Quantum transduction with adaptive control," Phys. Rev. Lett., vol. 120, no. 2, p. 20502, 2018.

[104] D. Gottesman, A. Kitaev, and J. Preskill, "Encoding a qubit in an oscillator," Phys. Rev. A, vol. 64, p. 12310, 2001.

[105] V. V. Albert, K. Noh, K. Duivenvoorden, D. J. Young, R. T. Brierley, P. Reinhold, C. Vuillot, L. Li, C. Shen, S. M. Girvin, B. M. Terhal, and L. Jiang, "Performance and structure of single-mode bosonic codes," Phys. Rev. A, vol. 97, p. 032346, Mar 2018. [Online]. Available: https://link.aps.org/doi/10.1103/PhysRevA.97.032346

[106] J. Davila-Rodriguez, F. N. Baynes, A. Ludlow, T. Fortier, H. Leopardi, S. Diddams, and F. Quinlan, "A thermal noise limited, rigidly-held optical reference cavity for ultra-low noise microwave generation," in Conference on Lasers and Electro-Optics. Optical Society of America, 2017, p. JF1D.4. [Online]. Available: http://www.osapublishing.org/abstract.cfm?URI=CLEO_AT-2017-JF1D.4

[107] A. J. Weinstein, C. U. Lei, E. E. Wollman, J. Suh, A. Metelmann, A. A. Clerk, and K. C. Schwab, "Observation and Interpretation of Motional Sideband Asymmetry in a Quantum Electromechanical Device," Phys. Rev. X, vol. 4, no. 4, p. 41003, Oct. 2014. [Online]. Available: http://link.aps.org/doi/10.1103/PhysRevX.4.041003

[108] A. H. Safavi-Naeini, J. Chan, J. T. Hill, S. Gröblacher, H. Miao, Y. Chen, M. Aspelmeyer, and O. Painter, "Laser noise in cavity-optomechanical cooling and thermometry," New Journal of Physics, vol. 15, no. 3, p. 35007, 2013. [Online]. Available: http://stacks.iop.org/1367-2630/15/i=3/a=035007

[109] T. Rocheleau, T. Ndukum, C. Macklin, J. B. Hertzberg, A. A. Clerk, and K. C. Schwab, "Preparation and detection of a mechanical resonator near the ground state of motion," Nature, vol. 463, pp. 72–75, Jan. 2010.

[110] A. D. Córcoles, J. M. Chow, J. M. Gambetta, C. Rigetti, J. R. Rozen, G. A. Keefe, M. B. Rothwell, M. B. Ketchen, and M. Steffen, "Protecting superconducting qubits from radiation," Applied Physics Letters, vol. 99, no. 18, p. 181906, 2011. [Online]. Available: http://dx.doi.org/10.1063/1.3658630

[111] S. Krinner, S. Storz, P. Kurpiers, P. Magnard, J. Heinsoo, R. Keller, J. Lütolf, C. Eichler, and A. Wallraff, "Engineering cryogenic setups for 100-qubit scale superconducting circuit systems," EPJ Quantum Technology, vol. 6, no. 1, p. 2, May 2019. [Online]. Available: https://doi.org/10.1140/epjqt/s40507-019-0072-0

[112] P. Krantz, M. Kjaergaard, F. Yan, T. P. Orlando, S. Gustavsson, and W. D. Oliver, "A quantum engineer's guide to superconducting qubits," Applied Physics Reviews, vol. 6, no. 2, p. 021318, 2019. [Online]. Available: https://doi.org/10.1063/1.5089550

[113] J. C. Sankey, C. Yang, B. M. Zwickl, A. M. Jayich, and J. G. E. Harris, "Strong and tunable nonlinear optomechanical coupling in a low-loss system," Nature Physics, vol. 6, no. 9, pp. 707–712, 2010. [Online]. Available: https://doi.org/10.1038/nphys1707

[114] Y. Tsaturyan, A. Barg, E. S. Polzik, and A. Schliesser, "Ultracoherent nanomechanical resonators via soft clamping and dissipation dilution," Nature Nanotechnology, vol. 12, no. 8, pp. 776–783, 2017. [Online]. Available: https://doi.org/10.1038/nnano.2017.101

[115] A. H. Safavi-Naeini, J. T. Hill, S. Meenehan, J. Chan, S. Gröblacher, and O. Painter, "Two-dimensional phononic-photonic bandgap optomechanical crystal cavity," Phys. Rev. Lett., vol. 112, p. 153603, 2014.

[116] P.-L. Yu, K. Cicak, N. Kampel, Y. Tsaturyan, T. Purdy, R. Simmonds, and C. Regal, "A phononic bandgap shield for high-q membrane microresonators," Appl. Phys. Lett., vol. 104, no. 2, p. 23510, 2014. [Online]. Available: http://scitation.aip.org/content/aip/journal/apl/104/2/10.1063/1.4862031

[117] J. M. Martinis, K. B. Cooper, R. McDermott, M. Steffen, M. Ansmann, K. D. Osborn, K. Cicak, S. Oh, D. P. Pappas, R. W. Simmonds, and C. C. Yu, "Decoherence in josephson qubits from dielectric loss," Phys. Rev. Lett., vol. 95, p. 210503, Nov 2005. [Online]. Available: https://link.aps.org/doi/10.1103/PhysRevLett.95.210503

[118] A. Romanenko and D. I. Schuster, "Understanding quality factor degradation in superconducting niobium cavities at low microwave field amplitudes," Phys. Rev. Lett., vol. 119, p. 264801, Dec 2017. [Online]. Available: https://link.aps.org/doi/10.1103/PhysRevLett.119.264801

[119] M. Reagor, H. Paik, G. Catelani, L. Sun, C. Axline, E. Holland, I. M. Pop, N. A. Masluk, T. Brecht, L. Frunzio, M. H. Devoret, L. Glazman, and R. J. Schoelkopf, "Reaching 10 ms single photon lifetimes for superconducting aluminum cavities," Appl. Phys. Lett., vol. 102, no. 19, 2013.

[120] A. Bruno, G. d. Lange, S. Asaad, K. L. v. d. Enden, N. K. Langford, and L. DiCarlo, "Reducing intrinsic loss in superconducting resonators by surface treatment and deep etching of silicon substrates," App. Phys. Lett., vol. 106, no. 8, p. 182601, May 2015.

[121] J. Wenner, R. Barends, R. C. Bialczak, Y. Chen, J. Kelly, E. Lucero, M. Mariantoni, A. Megrant, P. J. J. OMalley, D. Sank, A. Vainsencher, H. Wang, T. C. White, Y. Yin, J. Zhao, A. N. Cleland, and J. M. Martinis, "Surface loss simulations of superconducting coplanar waveguide resonators," Applied Physics Letters, vol. 99, no. 11, p. 113513, 2011. [Online]. Available: https://doi.org/10.1063/1.3637047

[122] W. Chen, D. A. Bennett, V. Patel, and J. E. Lukens, "Substrate and process dependent losses in superconducting thin film resonators," Superconductor Science and Technology, vol. 21, no. 7, p. 075013, may 2008. [Online]. Available: https://doi.org/10.1088%2F0953-2048%2F21%2F7%2F075013

[123] R. Barends, N. Vercruyssen, A. Endo, P. J. de Visser, T. Zijlstra, T. M. Klapwijk, P. Diener, S. J. C. Yates, and J. J. A. Baselmans, "Minimal resonator loss for circuit quantum electrodynamics," Applied Physics Letters, vol. 97, no. 2, p. 023508, 2010. [Online]. Available: https://doi.org/10.1063/1.3458705

[124] M. Sandberg, M. R. Vissers, J. S. Kline, M. Weides, J. Gao, D. S. Wisbey, and D. P. Pappas, "Etch induced microwave losses in titanium nitride superconducting resonators," Applied Physics Letters, vol. 100, no. 26, p. 262605, 2012. [Online]. Available: https://doi.org/10.1063/1.4729623

[125] A. Megrant, C. Neill, R. Barends, B. Chiaro, Y. Chen, L. Feigl, J. Kelly, E. Lucero, M. Mariantoni, P. J. J. O'Malley, D. Sank, A. Vainsencher, J. Wenner, T. C. White, Y. Yin,

J. Zhao, C. J. Palmstrøm, J. M. Martinis, and A. N. Cleland, "Planar superconducting resonators with internal quality factors above one million," Appl. Phys. Lett., vol. 100, no. 11, 2012.

[126] M. R. Vissers, J. Gao, D. S. Wisbey, D. A. Hite, C. C. Tsuei, A. D. Corcoles, M. Steffen, and D. P. Pappas, "Low loss superconducting titanium nitride coplanar waveguide resonators," Applied Physics Letters, vol. 97, no. 23, p. 232509, 2010. [Online]. Available: https://doi.org/10.1063/1.3517252

[127] J. Gao, "The physics of superconducting microwave resonators," Ph.D. dissertation, California Institute of Technology, 2008.

[128] M. R. Vissers, J. Hubmayr, M. Sandberg, S. Chaudhuri, C. Bockstiegel, and J. Gao, "Frequency-tunable superconducting resonators via nonlinear kinetic inductance," Applied Physics Letters, vol. 107, no. 6, p. 062601, 2015. [Online]. Available: https://doi.org/10.1063/1.4927444

[129] H. G. Leduc, B. Bumble, P. K. Day, B. H. Eom, J. Gao, S. Golwala, B. A. Mazin, S. McHugh, A. Merrill, D. C. Moore, O. Noroozian, A. D. Turner, and J. Zmuidzinas, "Titanium nitride films for ultrasensitive microresonator detectors," Applied Physics Letters, vol. 97, no. 10, p. 102509, 2010. [Online]. Available: https://doi.org/10.1063/1.3480420

[130] N. Nader, A. Kowligy, J. Chiles, E. J. Stanton, H. Timmers, A. J. Lind, F. C. Cruz, D. M. B. Lesko, K. A. Briggman, S. W. Nam, S. A. Diddams, and R. P. Mirin, "Infrared frequency comb generation and spectroscopy with suspended silicon nanophotonic waveguides," Optica, vol. 6, no. 10, pp. 1269–1276, Oct 2019. [Online]. Available: http://www.osapublishing.org/optica/abstract.cfm?URI=optica-6-10-1269

Appendix A

Fabrication Details

Standard lithographic fabrication techniques are used to make top and bottom chips. Microfabrication techniques involve depositing or etching layers or material in selective ways. Patterning is all done via photo lithography using a maskless contact aligner (Heidelberg MLA150). Figure A.1 shows profile schematic of fabrication process of both top and bottom chips. All fabrication was performed at the NIST Boulder Microfabrication Facility (BMF). Full etch chemistry and deposition parameters can be found in the process sheets included in Section A.1.

The bonding technique produces etalons or chips without epoxy holding them together. Figure A.2 shows a completed flip chip with mirror bonded to form an etalon, and a flip-chip assembled without epoxy. The bond is formed between a layer of SiO_2 grown on both chips. In the etalon, the mirror coating is capped with a thin layer of SiO_2 that bonds to the silicon of the bottom chip.

The surface treatment for preparing the bond is as follows:

(1) Ace/ipa sonication of both wafers, followed by SRD.

(2) Inspect/make sure no big particles.

(3) Ontos O2 clean on both wafers. Opto pr strip recipe

(4) Put both wafers in Ontos H2/N2 treatment

(5) SRD both wafers.

(6) Place one wafer right side up on the bonding jig.

(7) Move the flags over the wafer with the 1 toggle switch.

(8) Place the other wafer on top of the flags, upside down over the first wafer, and align the

flats

(9) Press together with a metal tweezers and hold for a few seconds.

(10) Retract the flags fully with the 1 toggle switch.

(11) Tap around the wafer a few times to make sure its pressed together uniformly

(12) Inspect on IR cam setup.

(13) Anneal 150C for 1 hr on hotplate.

(14) Inspect again.

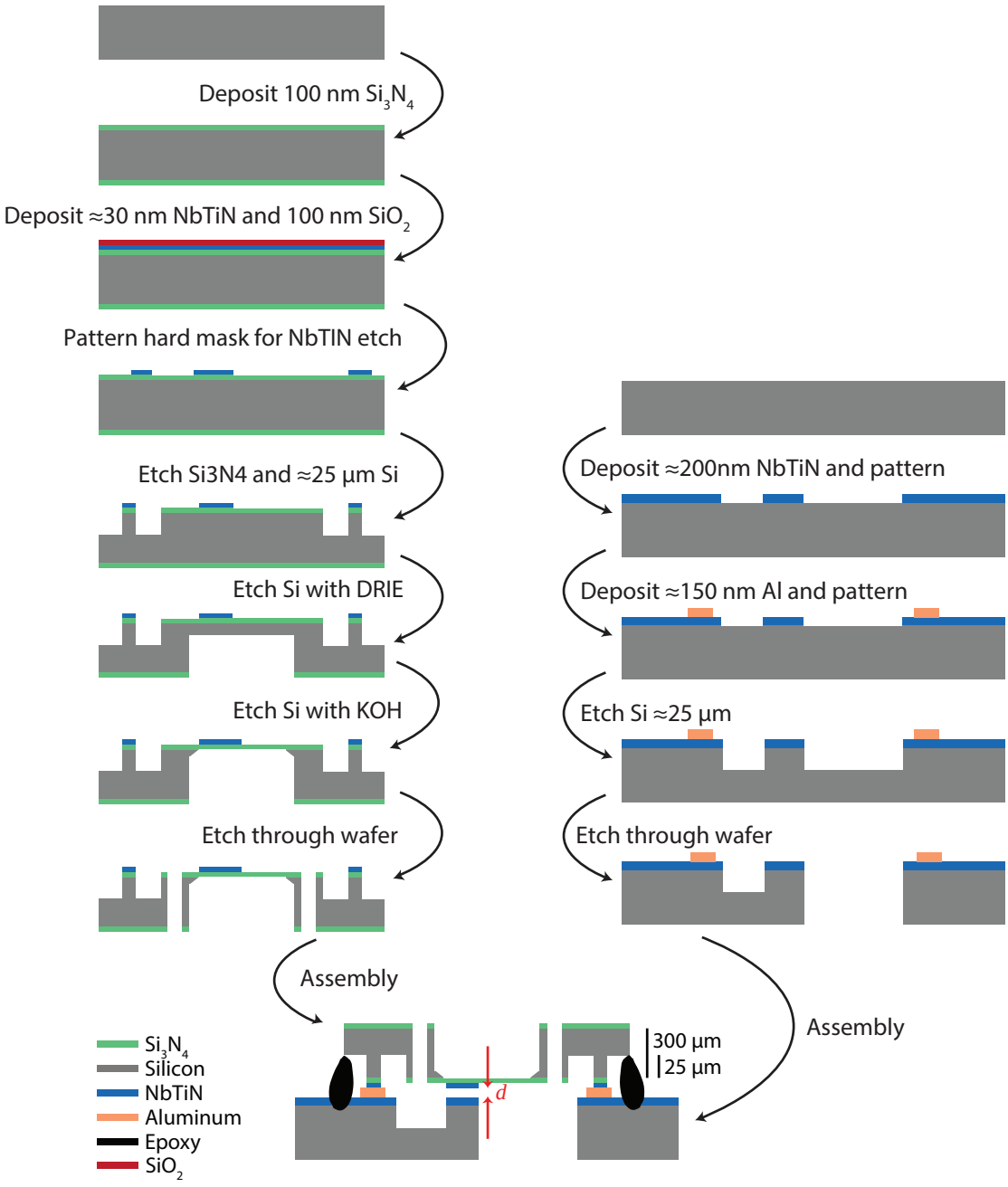

Figure A.1: **Construction details for converter chips.** Profile view of fabrication process. Layers are not to scale. Both chips start with high-resistivity silicon wafers. Layers are deposited and etched way to produce top and bottom chips with cutouts, released membrane, and LC circuit. Final flip-chip assembled as shown with $d = 150$nm

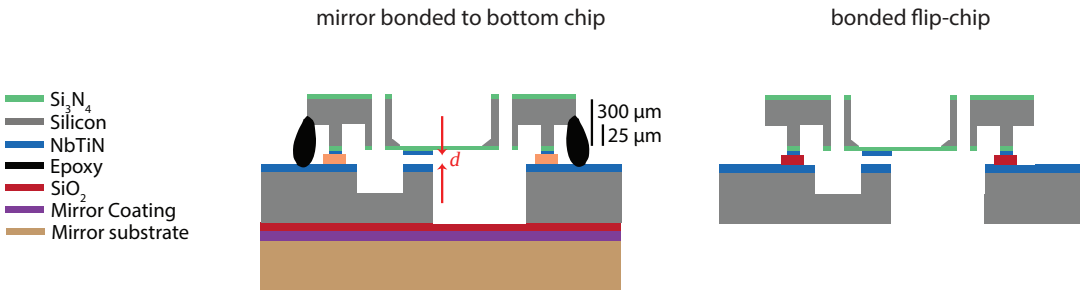

Figure A.2: **Bonding Assembly for flip-chips and etalon.** Profile views of assembled etalon and bonded flip-chip. Layers not to scale. Mirror is bonded to back of bottom chip to make naturally aligned etalon. Flip-chip is bonded by SiO_2 layers on posts to reduce effect of epoxy on d.

A.1 Process sheets

NbTiN Q Membrane Chip wfr_____
Date/Initials:_____ Project name: PSB020819.Membrane.wafer.NbtiN.Q.x.gds

Circle Wafer Type: Oxidized Si, Unoxidized Si, Sapphire, Other_____

Stepper job file: jb110815.MemLC.rwa

Layer / Image	PM/MLA150	ONE			
B1					
B2					
TR					

xic Image (1 of 6)

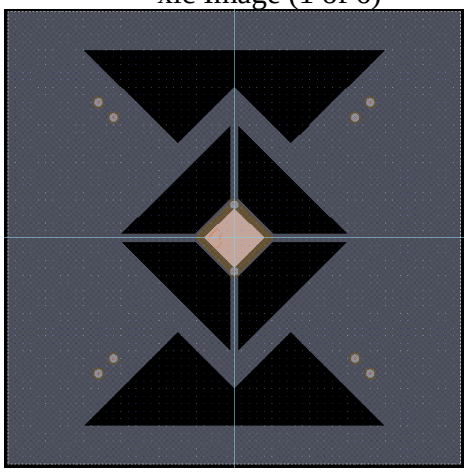

Process Outline

- Sputter NbTiN in PVD system
- Deposit SiO2 in PEVCD Oxford
- Pattern 1um resist
- Etch SiO2 in Trion Fl
- Etch NbTiN in NH4OH
- Etch SiO2 in HF
- Pattern 1 um resist
- Cut through nitride (with axic)
- Pattern 7um resist
- RIE 15um Si
- Glue to sapphire backing wafer (membranes down)
- (back side) Pattern 1 um resist
- Cut through nitride (with axic)
- Pattern 7um resist
- Etch into silicon substrate (STS ASE) until 10 microns left
- Koh, Protect with wax and backing wafer
- pattern 7 micron resist
- Dice/trampoline with DRIE

Thickness of: Wafer center: Wafer edge:
LPCVD stoich. Nitride:_____
Capacitor pads (Nb):_____
Si trench depth (Si):_____

Sputter NbTiN in big PVD System

Date/Initials_____

- Stress data:_____
- **Inspect** wafer surface under microscope:_____
- **Clean wafer in automated washer/drier**
- Load wafer into
  Load Lock p = _____(< $5x10^{-6}$) torr
  Main chamber base p = _____(< $5x10^{-8}$ torr)
- Recipe:

Ti Power:	**Nb Power:**
Time:	
Pressure:	
N2 Flow:	

- Record parameters:
  RF Clean:_____(10)mTorr, _____(45)W, _____(-298)V, _____(120)sec
  pre-dep: _____( )mTorr, Nb: _____( )W, _____( )V, _____( )A, _____( )sec
  Ti: _____( )W, _____( )V, _____( )A,
  dep: _____( )mTorr, Nb: _____( )W, _____( )V, _____( )A, _____( )sec
  Ti: _____( )W, _____( )V, _____( )A,

-
- **Inspect under microscope: _____**

PECVD SiO2 in Oxford ICP

Date/Initials_____

- Stress data:_____
- **Inspect** wafer surface under microscope:_____
- **Clean wafer in automated washer/drier**
- Load wafer into:
  Load Lock p = _____(< $5x10^{-6}$) torr
  Main chamber base p = _____(< $5x10^{-8}$ torr)
- Recipe:

DC Power:	**RF Power:**
Time:	
Pressure:	
Gas flows:	

- Record parameters:
  RF Clean:_____(10)mTorr, _____(45)W, _____(-298)V, _____(120)sec

  dep: _____(5.7)mTorr, _____(250)W, _____(305)V, _____(0.86)A, _____(130)sec
-
- **Inspect under microscope: _____**

Pattern SPR 660L Resist

Date/Initials_____

- **Clean masks in automated washer/drier 100s wash, 200s dry**
- **Clean wafer in automated washer/drier**
- **Pattern ____1____-layer resist on a wafer:**
  - **a)** Rinse spinner nozzle with acetone, dry with a wipe, and run program **PRG-660** a few times on dummy wafer to purge resist line.
  - **b)** Load wafer and spin P-20 primer and then SPR660L resist at 2600 rpm for 40s (run program **3A26P**)
  - **c)** Place wafer in hotplate at 95 C for 60 sec (load into hotplate and run).
  - **d)** Expose on stepper:
    - **i)** Masks: **_FCM07B4-00___**
    - **ii)** Job File: **_jb120913.MemLC.rwa_____**
    - iii) Layer ID: **_B3_____**
    - **iv)** Exposure Dose:_____ **(250) mJ/cm^2**, Focus: _____(0.0) μm
  - **e)** Place wafer in hotplate at 110 C for 60 sec (load into hotplate and run program **660-PEB**).
- Spin-develop with MF-26A for _____(**30/30 DSP**) s. Alternatively hand-develop in MF-26A, 60 sec, DI rinse 2 min, spin dry
- Inspect under microscope_____

Dry Etch SiO2 with Trion Fl (created 08/25/2011 by KC)

Date/Initials_____

- Recipe
- Preconditon machine by running plasma for 5-10 min without wafer
- Etch wafer:
  O2 _____(18) sccm Power f:_____(30)W,
  CF4 _____(42) sccm r:_____(0)W
  press:_____(100) mTorr Voltage:_____(-70)V Total etch time_____(4:00)min

- **Inspect under microscope: _____**
- **Strip resist:**
  - SVC-150 at ~70C for 15 to 20 minutes
  - DI Water Rinse
  - Ultrasound "dirty" acetone (2 min), Ultrasound "clean" acetone (2 min), dip IPA, dip DI water, then immediately place in rinser dryer and run.
- **Inspect under microscope: _____**

Wet Etch NbTiN (created 3/01/2012 by KC)

- **Wet-etch NbTiN in:** H2O: 100 ml H2O2 (30%): 40 ml NH4OH (30%): 20 ml

- **At 62 C**
- **Time:**_____s clear +_____s

- **Inspect under microscope: _____**
- **Clean in acetone in ultrasonic bath (power setting 70):** In "dirty" acetone 3 min, in clean acetone 3 min, rinse with IPA and spin dry.
- **Inspect under microscope**: **_____**
- **Measure etched thickness** using profilometer: _____(~100) nm

HF Etch SiO2

Date/Initials_____

Use BOE
Details:

Pattern SPR 660L Resist

(created 6/10/2011 by KC)
Date/Initials_____

- **Clean masks in automated washer/drier 100s wash, 200s dry**
- **Clean wafer in automated washer/drier**
- **Pattern ____1____-layer resist on a wafer:**
  - **a)** Rinse spinner nozzle with acetone, dry with a wipe, and run program **PRG-660** a few times on dummy wafer to purge resist line.
  - **b)** Load wafer and spin P-20 primer and then SPR660L resist at 2600 rpm for 40s (run program **3A26P**)
  - **c)** Place wafer in hotplate at 95 C for 60 sec (load into hotplate and run program **660-115**).
  - **d)** Expose on stepper:
    - **i)** Masks: **_ ___**
    - **ii)** Job File: **_ _____**
    - iii) Layer ID: **_B2_____**
    - **iv)** Exposure Dose:_____ **(250) mJ/cm^2**, Focus: _____(0.0) μm
  - **e)** Place wafer in hotplate at 110 C for 60 sec (load into hotplate and run program **660-PEB**).
- Spin-develop with MF-26A for _____(**30/30 DSP**) s. Alternatively hand-develop in MF-26A, 60 sec, DI rinse 2 min, spin dry
- Inspect under microscope_____

Dry Etch Si3N4 with Axic

(created 8/25/2011 by KC)

Date/Initials_____

- Recipe **JM_Nitride**
- Precondition machine for 5-10 minutes
- Etch wafer:

  Endpoint Filename (if saved):_____

  CF4 _____(42) sccm RIE forward_____(150),

  O2_____(2) sccm RIE refl_____(0) W

  p = _____(40) mTorr DC bias _____(380) V Total time _____(240)s

Inspect under microscope: _____

- **Inspect** all under microscope:_____
- **Strip resist:**
  - Clean Asher without wafer: 50 sccm O_2 50 W (subtract any offset) 3:00 min
  - Use Asher with wafer: 50 sccm O_2 50 W (subtract any offset) 3:00 min
  - Ultrasound "dirty" acetone (2 min), Ultrasound "clean" acetone (2 min), dip IPA, dip DI water, then immediately place in rinser dryer and run.
- **Inspect** under microscope:_____
- **Deck-tech** to measure Nitride thickness etched: Center of wfr: _____(____) nm, Edge:_____(____) nm

Pattern 7 micron SPR 220-3.0 Resist

(created 8/25/2011 by KC)

Date/Initials_____

- Rinse spinner nozzle with acetone, dry with a wipe, and run program **PRG-220-3** a few times on dummy wafer to purge resist line.
- Load wafer and spin P-20 primer and then SPR220-3.0 resist at 2500 rpm (run program **3B25P**)
- Place wafer in hotplate at 115 C for 90 sec (load into hotplate and run program **220-3**).
- Expose on stepper:
  - Masks: __
  - Job File: _ _____
  - Layer ID: ____**TR**_____
  - Exposure Dose:_____ **(275) mJ/cm^2**, Focus: _____(0.0) μm
- NO Post-bake!
- Spin-develop on Solitec with MF-26A for _____(60) s. Alternatively hand-develop in MF-26A, 60 sec, DI rinse 2 min, spin dry
- Inspect under microscope_____

Dry Etch Si Wafer with RIE

(created 1/13/2011 by KC)

Date/Initials_____

- **Deep RIE**:
  Recipe_____ (SPECBNOD)
  Etch Cycles_____(~25 cycles)
  He leak rate_____(<5 mT/min)
- **Inspect under microscope: _____**
- **Strip resist:**
  - Clean Technics PE-IIA asher without wafer: 50 sccm O_2 100 W (subtract any offset) 3:00 min
  - Etch wafer in the asher: 50 sccm O_2 100 W (subtract any offset) 5:00 min
  - Ultrasound "dirty" acetone (2 min), Ultrasound "clean" acetone (2 min), dip IPA, dip DI water, then immediately place in rinser dryer and run.
- **Inspect under microscope: _____**
- **Etch depth (either dek-tek or use focus on microscope)_____**

Glue Wafer to Sapphire Backing Wafer with Wax for DRIE

(created 3/2/2014 KC; modified 12/16/2014 KC)

Date/Initials_____

- Clean **DSP sapphire backing wafer** and **Si sample wafer** in automated washer/drier
- Ash ("wax side") **DSP sapphire backing wafer** and **Si sample wafer** in O2 plasma, 50 W, 3 min.
- Consult Dan Schmidt's recipe cartoon for "Double spun-on wax" (available on wiki) for the following:
- **Spin thick wax 2:1 = wax:EBR** by weight (_____rpm, _____(30) sec) using the wax spinner in bay 5 (Notes: Wax should not be more than ~1 month old; Squirt wax with plastic disposable droppers (with tapered tips cut off!) to cover 2/3-3/4 wafer, then spin) on:
  a) **sapphire backing wafer** (ashed side)
  b) **your wafer** (side to be buried in wax) and
- Put each wafer in its own waxer disc and **bake both in vacuum oven** (~25 in Hg) at _____ C (134C, oven set to 148C) for ____(20) min
- **Let wafers cool** (2 min) propped out of the waxer disc, than **sandwich together** in one of the waxer discs
- Top with the weight disc and **bake in vacuum** (~25 in Hg) oven at _____C (134C, oven set to 148C) for _____(20min - 60 min)
- If applicable inspect the front side of your wafer for cleanliness and that the previously patterned resist still looks good.
- If applicable deck-tech the thickness of the previously patterned resist to make sure wax baking did not change it: center_____, edge_____
- Spin clean Si wafer top with acetone and IPA. Ready for lithography or etching.

Dry Etch Si Wafer with DRIE

(created 1/13/2011 by KC, modified 12/29/14 by KC)

Date/Initials_____

- If etching **through** the Si wafer, you need a sapphire backing wafer as etch stop (see "Glue Wafer to Sapphire Backing Wafer with Wax for Deep RIE")

- Load wafer (face up) into STS Deep RIE
- Set/check that T = 20 C.
- Recipe **specbnod:**
  - Etch: 12 sec, 130 sccm SF6, 13 sccm O2, 36 mT, Platen: 295V, 12 W, Coil: 600W
  - Passivate 8 sec, 85 sccm C4F4, - 18 mT, Platen: 0 V, 0 W, Coil: 600W

Etch rate of Si wafer ~1 um/cycle, ~3 cycles/min
(275 um wafer takes ~90 min, 425 um wafer takes ~2hr 20 min)

Half-way through the etch **rotate wafer by 180 deg.** for more even etch.

Run	Cycles (Total)	He leak rate	Thickness left side	Thickness center	Thickness right
_____	_____(____)	_____	_____	_____	_____
_____	_____(____)	_____	_____	_____	_____
_____	_____(____)	_____	_____	_____	_____
_____	_____(____)	_____	_____	_____	_____
_____	_____(____)	_____	_____	_____	_____
_____	_____(____)	_____	_____	_____	_____
_____	_____(____)	_____	_____	_____	_____
_____	_____(____)	_____	_____	_____	_____
_____	_____(____)	_____	_____	_____	_____

- Inspect and measure etched thickness with microscope:

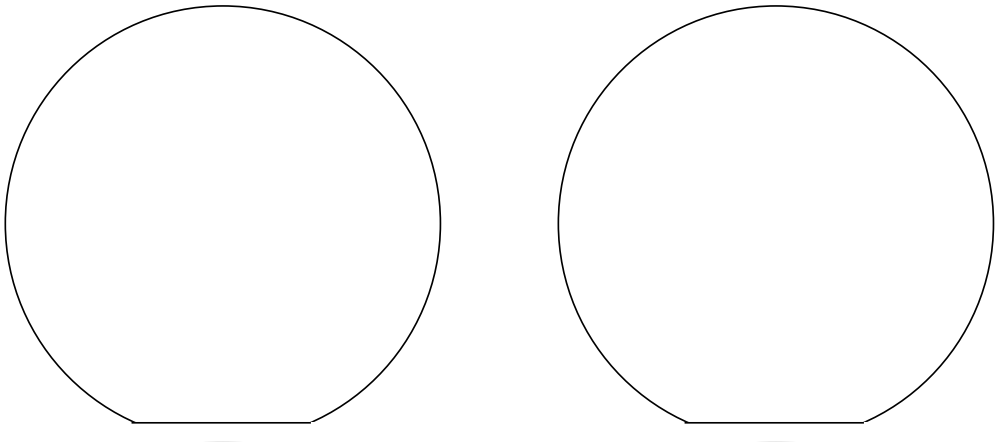

- See “Remove Resist, Backing Wafer and Wax after DRIE”.
- Also see “Remove Resist Residue after DRIE”

Remove Resist, Backing Wafer, and Wax after DRIE

(created 1/13/2011 by KC, modified 6/2/14 by KC)

Date/Initials_____

- **Strip Deep RIE resist:**
  - Clean Technics PE-IIA asher without wafer: 50 sccm O_2 50 W (subtract any offset) 5:00 min
  - Etch wafer sandwich in the asher: 50 sccm O_2 50 W (subtract any offset) 5:00 min
  - Spin clean resist side with Acetone and IPA
- **Inspect under microscope: _____**

Wet Etch Silicon in KOH-Based Etchant

(created 4/23/2013 by KC, modified 1/2/15 KC)

- Dip chips/wafer in **IPA** to wet them (helps brake surface tension in KOH later)
- Etch chips/wafer (etching side down in beaker) in **heated KOH-based etchant** (KOH mix or PSE-200)* at _____(80)C for _____hr:min
  (etch rate of <100> wafer is about ~1 um/min at 80 C).
- Dip into **heated ___(55)C DI water**, then **dilute with cold DI water** slowly and rinse/soak for ___(~5)min. Do not dry (keep in DI water until next step.)
- Soak in **DI water** for _____(5)min.
- Then rinse/dry on spinner with **DI water** and **IPA** (can reverse order)
- **Inspect under microscope: _____**
- Ultrasound in dirty acetone to remove koh etch residue

Remove Resist, Backing Wafer, and Wax after DRIE

(created 1/13/2011 by KC, modified 6/2/14 by KC)

Date/Initials_____

- **Remove backing wafer and clean wax:**
  - Heat on hotplate 125-130 C and slide off wafer/pieces from backing wafer
  - Soak in first acetone bath _____(20) min, then ultrasonicate in second acetone bath _____(2) min.
    (Alternative: soak in acethone bath overnight, then soak in 2nd acetone bath for ____(20) min.)
  - Spray with ACETONE then IPA while spinning dry.
    (Alternative: dip in IPA and let air dry.)
- **Inspect under microscope: _____**

Paint Wet Wax in Membrane hole

(created 1/2/15 by KC)

- Flip the wafer **top-side down** into the waxer holder (so membrane windows are up).
- Dab the wax mixture into the membrane windows **(back of wafer)** under microscope. Try to put in just enough wax to fill the window trench. Do not overfill to avoid spilling wax over the wafer surface.
- Bake with waxer holder in **vacuum oven** at _____(~**135 C** when set to 148 C) for _____(**20 min**). Wax should be dry after cooling.
- **Inspect both sides under microscope: _____**
- Clean off wax from the alignment marks.

Glue Wafer to Sapphire Backing Wafer with Wax for DRIE

(created 3/2/2014 KC; modified 12/16/2014 KC)

Date/Initials_____

- Clean **DSP sapphire backing wafer** and **Si sample wafer** in automated washer/drier
- Ash ("wax side") **DSP sapphire backing wafer** and **Si sample wafer** in O2 plasma, 50 W, 3 min.
- Consult Dan Schmidt's recipe cartoon for "Double spun-on wax" (available on wiki) for the following:
- **Spin thick wax 2:1 = wax:EBR** by weight (_____rpm, _____(30) sec) using the wax spinner in bay 5 (Notes: Wax should not be more than ~1 month old; Squirt wax with plastic disposable droppers (with tapered tips cut off!) to cover 2/3-3/4 wafer, then spin) on:
    a) **sapphire backing wafer** (ashed side)
    b) **your wafer** (side to be buried in wax) and
- Put each wafer in its own waxer disc and **bake both in vacuum oven** (~25 in Hg) at _____ C (134C, oven set to 148C) for ____(20) min
- **Let wafers cool** (2 min) propped out of the waxer disc, than **sandwich together** in one of the waxer discs
- Top with the weight disc and **bake in vacuum** (~25 in Hg) oven at _____C (134C, oven set to 148C) for _____(20min - 60 min)
- If applicable inspect the front side of your wafer for cleanliness and that the previously patterned resist still looks good.
- If applicable deck-tech the thickness of the previously patterned resist to make sure wax baking did not change it: center_____, edge_____
- Spin clean Si wafer top with acetone and IPA. Ready for lithography or etching.

Pattern 7 micron SPR 220-7.0 Resist (BMF)

(created 5/29/2014 by KC; modified 12/24/14 KC)

Date/Initials_____

- **Clean masks in automated washer/drier 100s wash, 200s dry**
- **Clean wafer in automated washer/drier**
- On bench **Wafer Coat 2:**
    - On a **dummy wafer** two times spin-purge SPR220-7.0 resist and P-20:
    - On **your wafer** spin SPR220-7.0 resist with recipe _____
      (**3IN COAT\ 3IN-SPR220_7-P20-2500-SLOWSPINUP_KAT3**)
    - Bake **your wafer** on a hotplate with **recipe** _____
      (**SPR220-7 3IN NO TOUCH KAT**)
    - If needed remove edge bead with acetone-soaked wipe, or Q-tip while spinning on a spinner

Dry Etch Si Wafer with DRIE

(created 1/13/2011 by KC, modified 12/29/14 by KC)

Date/Initials_____

- If etching **through** the Si wafer, you need a sapphire backing wafer as etch stop (see "Glue Wafer to Sapphire Backing Wafer with Wax for Deep RIE")

- Load wafer (face up) into STS Deep RIE
- Set/check that T = 20 C.
- Recipe **specbnod:**
  - Etch: 12 sec, 130 sccm SF6, 13 sccm O2, 36 mT, Platen: 295V, 12 W, Coil: 600W
  - Passivate 8 sec, 85 sccm C4F4, - 18 mT, Platen: 0 V, 0 W, Coil: 600W

Etch rate of Si wafer ~1 um/cycle, ~3 cycles/min
(275 um wafer takes ~90 min, 425 um wafer takes ~2hr 20 min)

Half-way through the etch **rotate wafer by 180 deg.** for more even etch.

Run	Cycles (Total)	He leak rate	Thickness left side	Thickness center	Thickness right
_____	_____(____)	_____	_____	_____	_____
_____	_____(____)	_____	_____	_____	_____
_____	_____(____)	_____	_____	_____	_____
_____	_____(____)	_____	_____	_____	_____
_____	_____(____)	_____	_____	_____	_____
_____	_____(____)	_____	_____	_____	_____
_____	_____(____)	_____	_____	_____	_____
_____	_____(____)	_____	_____	_____	_____
_____	_____(____)	_____	_____	_____	_____

- Inspect and measure etched thickness with microscope:

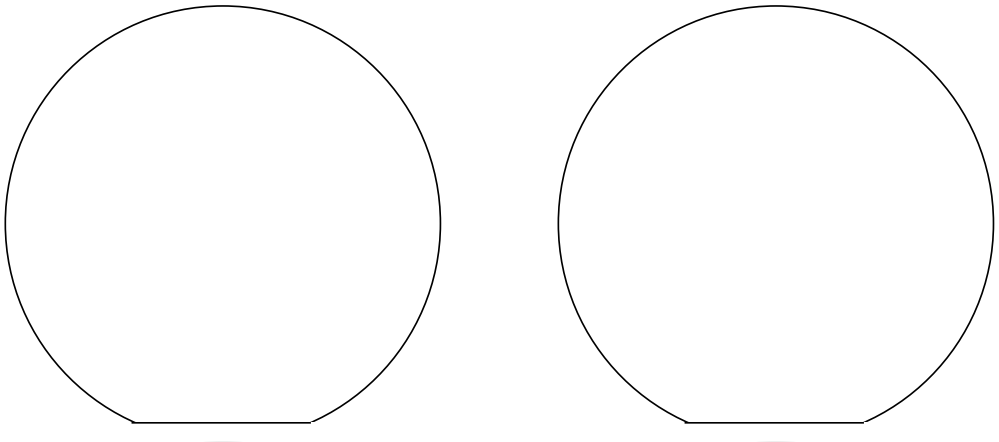

- See "Remove Resist, Backing Wafer and Wax after DRIE".
- Also see "Remove Resist Residue after DRIE"

Remove Resist, Backing Wafer, and Wax after DRIE

(created 1/13/2011 by KC, modified 6/2/14 by KC)

Date/Initials_____

- **Strip Deep RIE resist:**
  - Clean Technics PE-IIA asher without wafer: 50 sccm O_2 50 W (subtract any offset) 5:00 min
  - Etch wafer sandwich in the asher: 50 sccm O_2 50 W (subtract any offset) 5:00 min
  - Spin clean resist side with Acetone and IPA
- **Inspect under microscope: _____**
- **Remove backing wafer and clean wax:**
  - Heat on hotplate 125-130 C and slide off wafer/pieces from backing wafer
  - Soak in first acetone bath _____(20) min, then ultrasonicate in second acetone bath _____(2) min. (Alternative: soak in acethone bath overnight, then soak in 2nd acetone bath for ____(20) min.)
  - Spray with ACETONE then IPA while spinning dry. (Alternative: dip in IPA and let air dry.)
- **Inspect under microscope: _____**

Planar circuits and Bottom chip **wfr**_____
Date/Initials:_____ **Project name: fullwafer_param.x-cut.gds**

Circle Wafer Type: Oxidized Si, Unoxidized Si, Sapphire, Other_____

Stepper job file: **jb110815.MemLC.rwa**

Layer / Image -> | V	**PM**	**Note**
PM	SUSSPM—W1	
B1	MLA150	Nb/NbTiN
B2	MLA150	Al (separate job for each layer)

xic Image ( )

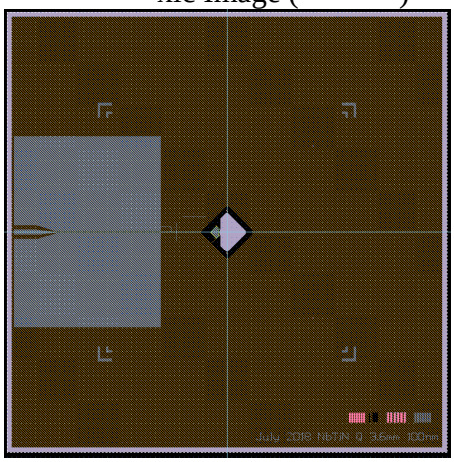

Process Outline

- Sputter 200nm NbTiN
- Etch bottom layer of metal NbTiN (etch in Oxford Fl)
- Pattern 1 um resist
- Sputter 200nm Nb lesker high temp
- Sputter Al 150nm in SIS
- Pattern 1um resist
- Pattern Al with mF-26A
- Pattern 1 um resist
- Etch Nb in IPE RIE
- Pattern 3um resist
- Etch trenches into Si around metal (DEEP RIE)
- Glue to Saph wafer
- Pattern 7um resist
- Dice with DRIE
- Final cleans

Thickness of: Wafer center: Wafer edge:
Bottom layer (Al):_____
Top layer (NbTiN):_____

Sputter NbTiN in big PVD System
Date/Initials_____

- Stress data:_____
- **Inspect** wafer surface under microscope:_____
- **Clean wafer in automated washer/drier**
- Load wafer into
  Load Lock p = _____(< $5x10^{-6}$) torr
  Main chamber base p = _____(< $5x10^{-8}$ torr)
- Recipe:

	Ti Power:	**Nb Power:**
	Time:	
	Pressure:	
	N2 Flow:	

- Record parameters:
  RF Clean:_____(10)mTorr, _____(45)W, _____(-298)V, _____(120)sec
  pre-dep: _____( )mTorr, Nb: _____( )W, _____( )V, _____( )A, _____( )sec
  Ti: _____( )W, _____( )V, _____( )A,
  dep: _____( )mTorr, Nb: _____( )W, _____( )V, _____( )A, _____( )sec
  Ti: _____( )W, _____( )V, _____( )A,

-
- **Inspect under microscope: _____**

Pattern SPR 660L Resist

(created 6/10/2011 by KC)
Date/Initials_____

- **Clean wafer in automated washer/drier**
- **Pattern ____1____-layer resist on a wafer:**
  a) Purge if first to use spinner in a few hours
  b) Load wafer and spin P-20 primer and then SPR660L resist at 2600 rpm for
  c) Place wafer in hotplate at 95C for 60 sec).
  d) Expose on MLA150:
  i) Job File: _ _____
  ii) Layer ID: _____
  iii) Exposure Dose:_____ **(250) mJ/cm^2**, Focus: _____(0.0) µm
  e) Place wafer in hotplate at 110 C for 60 sec).
- Spin-develop in Brewer with MF-26A for _____(30/30 DSP) . Alternatively hand-develop in MF-26A, 60 sec, DI rinse 2 min, spin dry
- Inspect under microscope_____

Film on Wafer	Spin speed	Thickness	Dose	Calibration
Nb	3000 rpm	1.01 µm	270 mJ/cm^2	LRV
Nb	**2600 rpm**	**1.12 µm**	**250 mJ/cm^2**	**LRV**

Dry Etch NbTiN with Oxford Fl (vertical wall) (created 8/25/2011 by KC)

Date/Initials_____

- Load cleaning wafer into **Oxford Fluorine RIE** and run recipes:
  _____ _____(10) min
  CMB Ti undr less O2.prc _____(1-2) min to condition
  then load your wafer, use **endpoint detector** and run:

Recipe _____ (CMB Ti undr less O2.prc) Endpoint Filename (if saved):_____

CHF3_____(25)sccm
Ar_____(100)sccm
O2_____(2.5)sccm
p = _____( ) mTorr
RIE = f_____( ), r_____( ) W
ICP = f_____( ), r_____( ) W
DC bias = _____( ) V
T = _____( )C
Total time = _____( )s

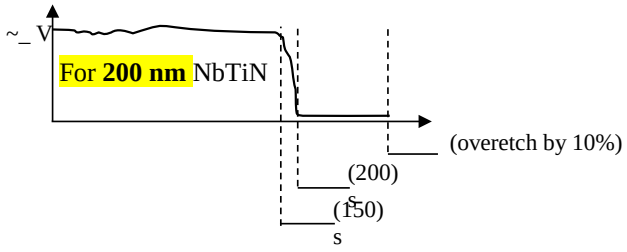

- **Inspect** all under microscope:_____
- **Strip resist:**
- Clean Asher without wafer: 50 sccm O_2 50 W (subtract any offset) 3:00 min
- Use Asher with wafer: 50 sccm O_2 50 W (subtract any offset) 3:00 min
- Ultrasound "dirty" acetone (2 min), Ultrasound "clean" acetone (2 min), dip IPA, dip DI water, then immediately place in rinser dryer and run.
- **Inspect** under microscope:_____
- **Deck-tech** to measure Nb thickness etched: Center of wfr: _____(____) nm, Edge:_____(____) nm

Pattern SPR 660L Resist (created 6/10/2011 by KC)

Date/Initials_____

- **Clean wafer in automated washer/drier**
- **Pattern ____1____-layer resist on a wafer:**
  a) Purge if first to use spinner in a few hours
  b) Load wafer and spin P-20 primer and then SPR660L resist at 2600 rpm for
  c) Place wafer in hotplate at 95C for 60 sec).
  d) Expose on stepper:
  i) Job File: _ _____
  ii) Layer ID: _____
  iii) Exposure Dose:_____ **(250) mJ/cm^2**, Focus: _____(0.0) μm
  e) Place wafer in hotplate at 110 C for 60 sec).
- Spin-develop in Brewer with MF-26A for _____(30/30 DSP) . Alternatively hand-develop in MF-26A, 60 sec, DI rinse 2 min, spin dry
- Inspect under microscope_____

Sputter Nb in Lesker High Temp

Date/Initials_____

- Stress data:_____
- **Inspect** wafer surface under microscope:_____
- **Clean wafer in automated washer/drier**
- Load wafer into
  Load Lock p = _____(< $5x10^{-6}$) torr
  Main chamber base p = _____(< $5x10^{-8}$ torr)
- Recipe:

  Nb Power:
  Time:
  Pressure:
  N2 Flow:
- Record parameters:
  RF Clean:_____(10)mTorr, _____(45)W, _____(-298)V, _____(120)sec
  pre-dep: _____( )mTorr, Nb: _____( )W, _____( )V, _____( )A, _____( )sec
  Ti: _____( )W, _____( )V, _____( )A,
  dep: _____( )mTorr, Nb: _____( )W, _____( )V, _____( )A, _____( )sec
  Ti: _____( )W, _____( )V, _____( )A,
- **Strip resist:**
  - Ultrasound in "Liftoff" for 10 minutes
  - Ultrasound "dirty" acetone (5 min), Ultrasound "clean" acetone (2 min), dip IPA, dip DI water, then immediately place in rinser dryer and run.
- **Inspect under microscope: _____**
- **Deck-tech** to measure Nb thickness dep'd: Center of wfr: _____(____) nm, Edge:_____(____) nm

Pattern SPR 660L Resist

(created 6/10/2011 by KC)

Date/Initials_____

- **Clean wafer in automated washer/drier**
- **Pattern ____1____-layer resist on a wafer:**
  a) Purge if first to use spinner in a few hours
  b) Load wafer and spin P-20 primer and then SPR660L resist at 2600 rpm for
  c) Place wafer in hotplate at 95C for 60 sec).
  d) Expose on MLA150:
  i) Job File: _ _____
  ii) Layer ID: _____
  iii) Exposure Dose:_____ **(250) mJ/cm^2**, Focus: _____(0.0) μm
  e) Place wafer in hotplate at 110 C for 60 sec).
- Spin-develop in Brewer with MF-26A for _____(30/30 DSP) . Alternatively hand-develop in MF-26A, 60 sec, DI rinse 2 min, spin dry
- Inspect under microscope_____

Dry Etch in Nb with IPE RIE (created 08/25/2011 by KC)

Date/Initials_____

- Recipe **nbsf6.prc**
- Preconditon machine by running plasma for 5-10 min without wafer
- Etch wafer: Power f:_____(____)W,
  SF_6 _____(____) sccm r:_____(0)W
  press:_____(____) mTorr Voltage:_____(____)V Total etch time_____(____)min

  Rough etch rate ~ _____ (?)

- **Inspect under microscope: _____**
- **Strip resist:**
  - Clean Asher without wafer: 50 sccm O_2 50 W (subtract any offset) 3:00 min
  - Etch in Asher with wafer: 50 sccm O_2 50 W (subtract any offset) 3:00 min
  - Ultrasound "dirty" acetone (2 min), Ultrasound "clean" acetone (2 min), dip IPA, dip DI water, then immediately place in rinser dryer and run.
- **Inspect under microscope: _____**

Sputter 100nm Al in SIS System (created 3/1/2012 by KC)

Date/Initials_____

(Check recent deposition rates)

- **Inspect** wafer surface under microscope:_____
- **Clean wafer in automated washer/drier**
- Load wafer into **SIS-system**:
  Load Lock p = _____(< $5x10^{-6}$) torr ~15 min pump
  Main chamber base p = _____(< $5x10^{-8}$ torr)
- Recipe: **QubitBaseCleanAldep:** **qb_sub_Clean60W** (60 W rf clean, 60 sec) **(for cleaning blank wfr) OR** **qb_sub_Clean110W_junction** (420 sec) **(for removing AlOx)**
  qb_sub_Aldep100nm:

line	value
82	**5 mT**
230	**gun 2 (Al)**
240	**300 W**
825	~~**380 sec → ~100 nm** (0.26 nm/sec)~~

Data at 300 W, 5 mT:
380 s → ~100 nm
1140 s → ~362 nm (7/12/11 kc)
313 s → ~100 nm (7/13/11 kc)
385 s → 110 nm (8/6/11 dl)
525 s → 150 nm (8/11/11 dl)
350 s → 102 nm (9/3/11 jdw)
315 s → 81 nm (2/1/12 fql)
317 s → 101 nm (2/10/12 fql)

- Record parameters:
  RF clean: _____(15)mTorr, _____(60)sec, _____/_____(60/0) forw/refl W, _____(289)V
  Al pre-dep: _____(5.0)mTorr, _____(300)W, _____(280)V, _____(1.0)A, _____(60)sec
  Al dep:_____(5.0)mTorr, _____(300)W, _____(280)V, _____(1.0)A, _____(350)sec

- **Inspect** wafer under microscope:_____

Etch Al MF-26A (created 3/01/2012 by KC)

Date/Initials_____

- Spin-develop in Brewer with MF-26A for _____(4x45 DSP) .
- **Strip Resist**
  - Sonicate **i**n "dirty" acetone 3 min, in clean acetone 3 min, dip IPA, dip DI water, then immediately place in rinser dryer and run.
- **Inspect under microscope**: _____
- **Measure etched thickness** using profilometer: _____

Pattern SPR 660L Resist (created 6/10/2011 by KC)

Date/Initials_____

- **Clean wafer in automated washer/drier**
- **Pattern ____1____-layer resist on a wafer:**
  - **a)** Purge if first to use spinner in a few hours
  - **b)** Load wafer and spin P-20 primer and then SPR660L resist at 2600 rpm for
  - **c)** Place wafer in hotplate at 95C for 60 sec).
  - **d)** Expose on stepper:
    - **i)** Job File: _ _____
    - ii) Layer ID: _ _____
    - **iii)** Exposure Dose:_____ **(250) mJ/cm^2**, Focus: _____(0.0) μm
  - **e)** Place wafer in hotplate at 110 C for 60 sec).
- Spin-develop in Brewer with MF-26A for _____(30/30 DSP) . Alternatively hand-develop in MF-26A, 60 sec, DI rinse 2 min, spin dry
- Inspect under microscope_____

Dry Etch Si Wafer with Deep RIE (created 1/13/2011 by KC)

Date/Initials_____

- **Deep RIE**:
  Recipe_____ (SPECZNOD)
  Etch Cycles_____(~10 cycles)
  He leak rate_____(<5 mT/min)
- **Inspect under microscope: _____**
- **Strip resist:**
  - Clean Technics PE-IIA asher without wafer: 50 sccm O_2 100 W (subtract any offset) 3:00 min
  - Etch wafer in the asher: 50 sccm O_2 100 W (subtract any offset) 5:00 min
  - Ultrasound "dirty" acetone (2 min), Ultrasound "clean" acetone (2 min), dip IPA, dip DI water, then immediately place in rinser dryer and run.
- **Inspect under microscope: _____**

- **Etch depth (either dek-tek or use focus on microscope)_____**

Glue Wafer to Sapphire Backing Wafer with Wax for Deep RIE

(created 1/6/2011 by KC)

Date/Initials_____

- Spin thick wax (2:1 wax:EBR by weight) on **a)** the back of your wafer and **b)** sapphire backing wafer (_____ (**MAX)** rpm, _____ (60-90) sec) on the wax spinner
- Bake both wafers in vacuum oven, 20 min, 125 C in waxer discs
- Let wafer cool, than sandwich together in the waxer disc
- Top with the weight disc and bake in vacuum oven for _____(20min - 60 min), 125 C

Pattern 7 micron SPR 220-7.0 Resist On Backside

(created 8/25/2011 by KC)

Date/Initials_____

- Purge line if first to use in a few hours
- Load wafer and spin P-20 primer and then SPR220-7.0 resist at 2500 rpm
- Remove edge bead with acetone-soaked wipe
- Place wafer in hotplate at 115 C for 90 sec (load into hotplate and run program **220-7**).
- Expose on MLA150:
    - Job File: _ _____
    - Layer ID: _____
    - Exposure Dose:_____**() mJ/cm^2**, Focus: _____(0.0) μm
- NO Post-bake! WAIT ~20 minutes for water to be reabsorbed into resist
- Spin-develop on Solitec with MF-26A for _____(**80**) s. Alternatively hand-develop in MF-26A, 80 sec, DI rinse 2 min, spin dry
- Inspect under microscope_____
- Measure resist thickness_____

Dry Etch Si Wafer with Deep RIE

(created 1/13/2011 by KC)

Date/Initials_____

- **Deep RIE**:
  Recipe_____ (SPECZNOD)
  Etch Cycles_____(~400 cycles)
  He leak rate_____(<5 mT/min)
- **Inspect under microscope: _____**
- **Strip resist:**
    - Clean Technics PE-IIA asher without wafer: 50 sccm O_2 100 W (subtract any offset) 3:00 min
    - Etch wafer in the asher: 50 sccm O_2 100 W (subtract any offset) 5:00 min
    - Place on spinner sapphire side down, spray with acetone then IPA then DI water
- **Inspect under microscope: _____**
- **Etch depth (either dek-tek or use focus on microscope)_____**

Remove chips from sapphire backing wafer

(created 1/6/2011 by KC)

Date/Initials_____

- Soak (typically overnight) in acetone with wafer held so that die fall onto cleanroom wipe
- Place die in clean acetone bath
- Sonicate 5 minutes high power
- Dip IPA
- Blow Dry
- **Inspect under microscope: _____**

Final Clean

(created 1/6/2011 by KC)

Date/Initials_____

- Soak die for 20 minutes in EKC 265 at 70C
- Dip IPA bath
- Dip IPA bath
- Dip DI water
- Place on spinner and spray with DI water, let dry (3k rpm for 4 minutes is usually sufficient)
    - Alternatively, spray DI water and end with a light squirt of IPA and spin dry (takes a few seconds)